AN ABSTRACT OF THE DISSERTATION OF

Kenneth James Squire for the degree of Doctor of Philosophy in Electrical and Computer Engineering presented on December 6, 2019.

Title: Optical Sensors using Biological Photonic Crystals

Abstract approved:

_____

Alan X. Wang

This dissertation focuses on the application of diatom frustules, the biosilica shell of an algae possessing physical and photonic properties capable of enhancing optical signals, for the enhancement of optical sensing. In this work, we incorporate diatom frustules into biosensors for signal enhancement and improved target molecule detection. The potential for immunoassay improvement from frustules is first demonstrated using standard sandwich immunoassay fluorescence detection and various analytical methods are explored to analyze the signal. The diatom-based sandwich fluorescence immunoassay is then employed to the detection of the clinically important biomarker, N-terminal pro-B-type natriuretic peptide (NT-proBNP), for the screening of heart failure. Machine learning analyses are employed to further improve the results and enable efficient screening in human plasma. Lastly, the versatility of the frustules is demonstrated by utilizing the frustule, paired with a core-shell nanoparticle, to perform surface-enhanced Raman spectroscopy detection of vapors from explosives. This work validates the utilization of diatom frustules as a means of enhancing optical signals and highlights their unique capabilities to enable superior analyte detection.

Optical Sensors using Biological Photonic Crystals

by
Kenneth James Squire

A DISSERTATION

submitted to

Oregon State University

in partial fulfillment of
the requirements for the
degree of

Doctor of Philosophy

Presented December 6, 2019
Commencement June 2020

Doctor of Philosophy dissertation of Kenneth James Squire presented on December 6, 2019

APPROVED:

Major Professor, representing Electrical and Computer Engineering

Head of the School of Electrical Engineering and Computer Science

Dean of the Graduate School

I understand that my dissertation will become part of the permanent collection of Oregon State University libraries. My signature below authorizes release of my dissertation to any reader upon request.

Kenneth James Squire, Author

ACKNOWLEDGEMENTS

I would like to express my gratitude to my advisor Dr. Alan Wang for his guidance and council throughout my graduate school education. He has mentored my research, guided my efforts, and provided opportunities for professional development, all with an eye on real training for future success in my career. I appreciate his support and encouragement through this process.

I would like to thank my lab mates for their comradery and friendship. They have lent an ear when progress had stalled and counseled with me on the appropriate methods of advancing my research. Their friendship and encouragement mean more than they can know.

I want to express my appreciation to my family. Their support through the course of my Ph.D. education has been invaluable and has been instrumental in my successful completion.

Lastly, I want to thank my lovely wife, Stephanie. The many all-night experiments and obstacles overcome would not have been possible without her continued love, support, and encouragement. The completion of this Ph.D. degree is as much her accomplishment as it is mine.

CONTRIBUTION OF AUTHORS

Dr. Xianming Kong aided with the fluorescence spectroscopy outlined in Chapter 2 and gave overall advice about the immunoassay process. Dr. Paul LeDuff and Joseph Kraai helped with the preparation of diatom frustules with Dr. Gregory Rorrer advising them. Dr. Yong Zhao and Dr. Ailing Tan advised about the chemometric methods implemented in Chapter 3. Dr. Sivashanmugan Kundan aided with general experimental design and organization. Dr. Alan Wang advised through the whole process.

TABLE OF CONTENTS

Page

TABLE OF CONTENTS (Continued)

Page

TABLE OF CONTENTS (Continued)

Page

TABLE OF CONTENTS (Continued)

Page

LIST OF FIGURES

Figure Page

LIST OF FIGURES (Continued)

Figure Page

LIST OF FIGURES (Continued)

Figure Page

LIST OF FIGURES (Continued)

Figure Page

CHAPTER 1. INTRODUCTION

1.1 Optical Sensing Technique Key Parameters

Cancerous biomarkers, hidden explosives, toxins in food: these are a few of the many targets that have been detected using optical techniques. When considering sensors, a few of the most important parameters are sensitivity, selectivity, and responsivity. Sensitivity denotes the correlation between the analyte's concentration and the sensor's output. The higher the sensitivity, the lower the concentration that is able to be detected. Selectivity relates to a sensor's ability to discriminate between the target analyte and competing materials within the sample matrix. A sensor with high selectivity is able to measure the signal from the desired target, despite an abundance of competing molecules. A sensor that can quickly achieve detection, has a high responsivity. It is desirable that a sensor should accel in each of these parameters, while maintaining a low cost to enable widespread application of the sensor. Optical sensing techniques have gained a lot of attention over the past couple decades for their prowess in each of these areas. Optical sensing generally relies on a change in the amount or quality of light to signal a detection event. By observing a change in optical intensity, wavelength, or polarization, these sensors are able to detect analytes. Because optical detection techniques generally have high sensitivity, specificity and responsivity, they are among the preferred methods of detection. Two of the most prominent methods of detection are fluorescence sensing and surface-enhanced Raman spectroscopy.

1.2 Fluorescence Sensing

1.2.1 Basic Mechanism

Fluorescence sensing is a well-established, powerful detection technique. It relies on incident light exciting electrons of a sample to a higher energy state. The excited electron will experience non-radiative relaxation resulting in a drop to a lower energy state. The electron then undergoes a radiative relaxation, wherein a photon is released with energy equal to the energy difference between the excited state and the ground state. This process is shown in Fig. 1.1 below. The resultant energy difference between the excitation source and the emitted light results in a bathochromic shift.

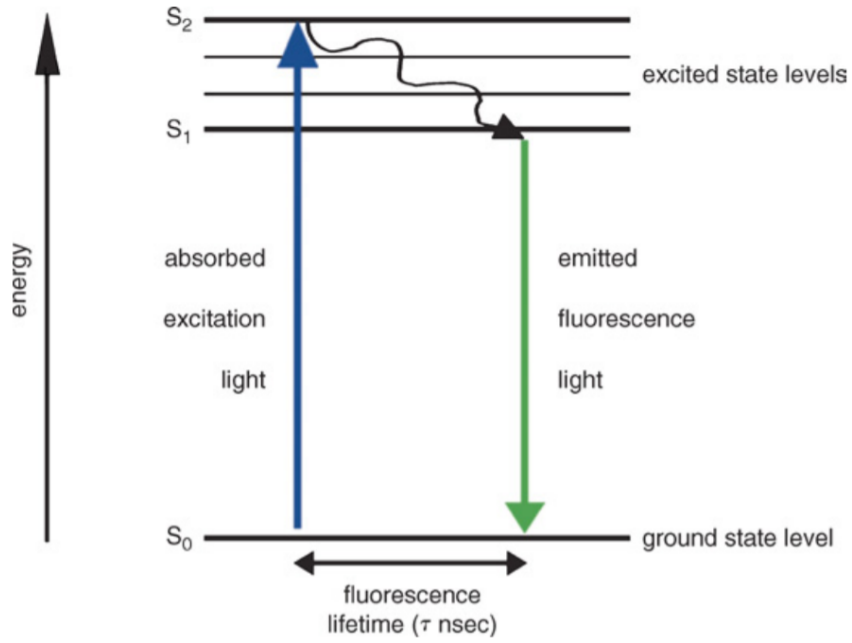

Fig. 1.1: Jablonski diagram demonstrating the mechanism of fluorescence[1].

1.2.2 Methods of Fluorescence Sensing and Applications

The fluorescence signal can be inherent within the analyte itself or can be from a fluorescent tag chemically attached to the analyte. The detection of the fluorescence emission is generally achieved in two ways: fluorescence spectroscopy and fluorescence imaging. Fluorescence spectroscopy relies on the utilization of a spectrometer to measure the emitted light. The emission spectral intensity, when compared to a calibration plot, can identify and quantify the analyte present. Furthermore, the spectral information obtained can be utilized in multiplex detection of multiple analytes with different emission spectra. Fluorescence spectroscopy is a highly sensitive detection technique that has been employed to detect a variety of analytes including explosives[2-4], toxins in food[5, 6], and cancer[7-9], to name a few. For fluorescence imaging, rather than utilizing a spectrometer, an imager is used to capture and measure the fluorescent light. This maintains the spatial information as well as the fluorescence intensity while enabling detection with low-cost-imagers. This is particularly useful for point-of-care sensing[10-13] and cell phone-based applications[14-16].

1.2.3 Improved Fluorescence and Practical Examples

To improve fluorescence detection, several things can be done. The first is to enhance the excitation of the fluorescent analyte. The increased excitation results in greater emission and thus, greater signal strength. Similarly, enhancing the emission also gives greater signal. This can be achieved by increasing the fluorescent efficiency of the interrogated molecule or by decreasing the fluorescence lifetime. This reduces

the possibility of non-radiative relaxation and increases the conversion efficiency from the excitation source to the emission. In addition to enhanced excitation and emission, concentration of the analytes results in stronger signals and higher sensitivity.

To these ends, several works have been presented to enhance the signal of fluorescence sensors. Most of those enhancements focus on utilizing plasmonic effects to enhance electromagnetic field experienced by the fluorophore, resulting in enhanced excitation. However, these are very localized enhancements and if the metallic structure is too close to the fluorophore, the fluorescence will be quenched, and no signal will be observed. Novotny's group investigated the fluorescence enhancement with respect to distance from a gold nanoparticle (Au NP) to determine the change from quenching to enhancement regime[17, 18]. To overcome the quenching and adequately remove the fluorophore from the plasmonic metal, sophisticated and inventive means must be employed to achieve the enhancement without quenching the signal. Acuna et al., used a crosslinker to label DNA and maintain the distance from the NP to the fluorophore[19]. Aslan et al. utilized a silica shell around the silver (Ag) NP to shield the fluorophores from quenching and still maintain the enhanced local field effect[20]. These few examples are represented in Fig. 1.2 below. The use of external NP manipulation, chemical crosslinkers, or physical spacers is effective; however, each method adds further cost and complexity to the system while not guaranteeing the fluorophore remains unquenched.

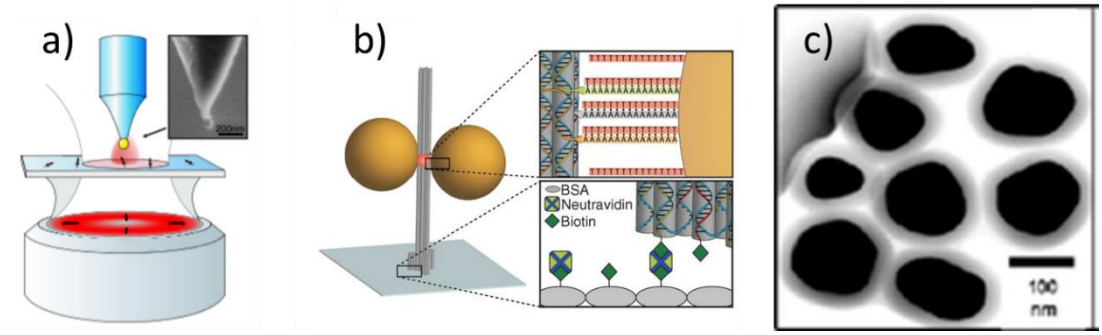

Fig 1.2: Demonstrations of several methods of metallic NP isolation from fluorophores while still achieving the local field enhancement using external manipulation (a), chemical crosslinkers (b), and physical spacers (c)[17-20].

Analyte preconcentration is another preferred method of fluorescence enhancement that has attracted interest. The utilization of metal-organic frameworks (MOF) has been demonstrated to preconcentrate analytes within its porous structure[21, 22]. For biological detection of antibodies, a lateral flow immunoassay allows the preconcentration of the analyte upon a designed area of the sensor[23, 24]. The creativity and methodology of concentrating the analytes is varied; however, most of these still add cost, complexity, or further sample preparation to the sensor. A simple, cost-effective method is needed to enhance fluorescence without inducing unnecessary complexity to the sensing process.

1.3 Surface-Enhanced Raman Spectroscopy

1.3.1 Basic Mechanism

Incident light upon a molecule can induce rovibrational modes resulting in inelastic Raman scatter[25]. The spectral shift of the Raman scatter is determined by the molecular bonds within the material and thus, can act as an optical fingerprint for

the material as illustrated in Fig. 1.3a below. Exciting a substance with a monochromatic light and then collecting and analyzing the Raman scatter, as shown in Fig. 1.3b below, allows for detection, quantification, as well as identification of analytes. However, Raman scattering occurs infrequently compared to the elastic Rayleigh scattering, making the detection of the Raman signal difficult. To improve the Raman signal, surface-enhanced Raman scattering (SERS) has been developed. This is achieved by performing the measurement near a plasmonic structure. The incident light excites surface plasmons within the metallic, plasmonic structure which results in greatly enhanced electromagnetic fields near its surface. When the analyte is near the plasmon, it experiences a much greater field, which results in greater Raman scattering, raising the signal to levels of practical utility.

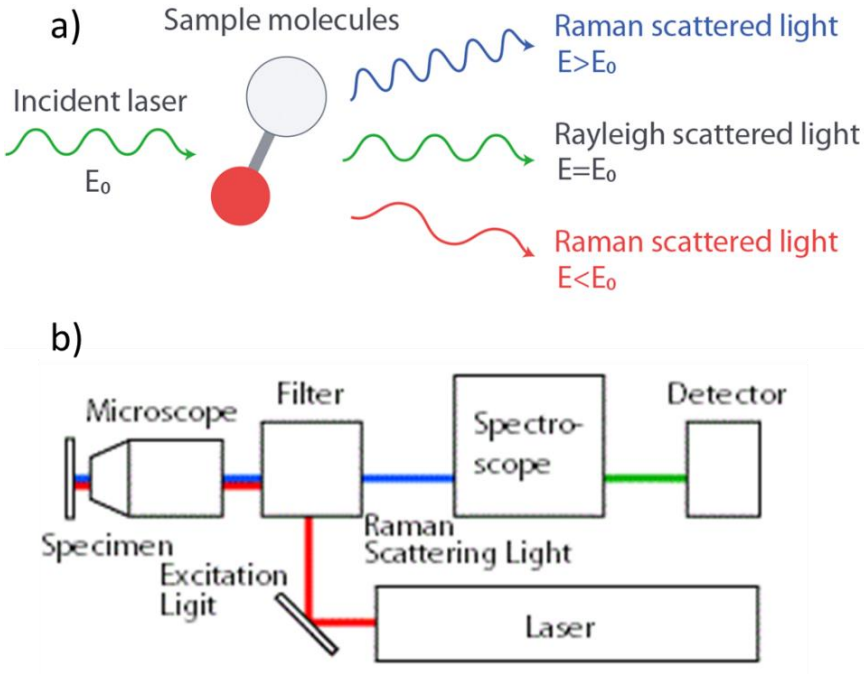

Fig. 1.3: Diagram depicting Raman scattering mechanism (a) and common measurement schematic (b) [26].

1.3.2 Applications and Methods of SERS Sensing

SERS has been employed to detect a wide array of analytes in a variety of fields. Ranging from detecting life on Mars[27-29] to drug abuse detection[30-32], SERS has been utilized in biosensing[33-35], safety and security[36-38], and art restoration[39-41]. There have been many innovative methods of introducing the plasmonic structure near the sample depending on its materialistic phase, as well as the sample matrix. The creation of a "smart-dust" has been pursued to enable the deposition of the plasmonic nanoparticles directly upon the sample[42-44]. Another method (called tip-enhanced Raman spectroscopy) is the introduction of a plasmonic probe that is placed in the proximity of the measured area[45-47]. Examples of these methods are shown in Fig. 1.4 below. Despite the many means of enhancement, the most prevalent approach is to create a substrate with metallic nano-features, whereupon plasmons may be excited and the sample can then be placed upon the substrate and the SERS measured.

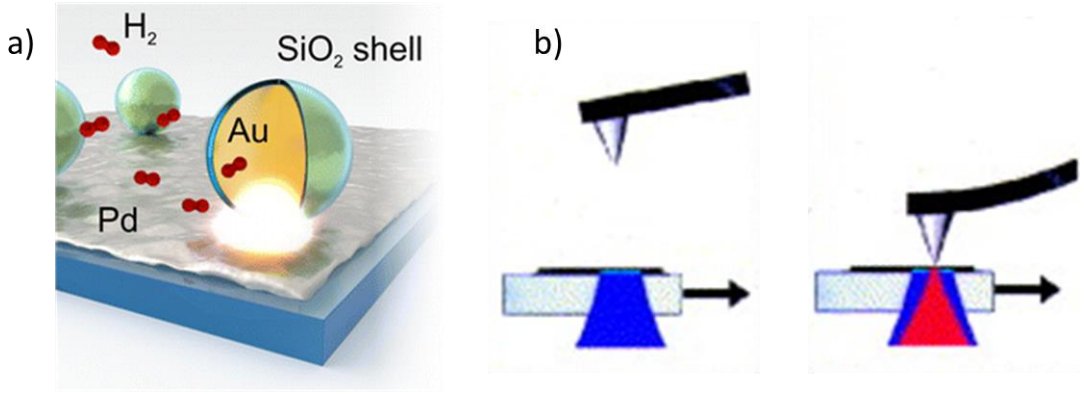

Fig. 1.4: Examples of "smart dust" (a) and tip-enhanced Raman spectroscopy (b) [42, 47].

1.3.3 SERS Substrates and Practical Examples

The SERS substrates can generally be categorized into two groups: top-down rationally-designed and bottom-up assembled substrates. The first group relies on sophisticated and expensive fabrication techniques, and cleanroom level technologies to achieve high sensitivity and good reproducibility[48-50]. Examples of this technique are shown in Fig 1.5 below. This method can yield excellent substrates; however, the cost and time of fabrication may render them impractical. Bottom-up methods generally rely on random assembly of NPs resulting in inexpensive, irreproducible sensing substrates[51]. Both methods have their advantages and disadvantages and work is being done to integrate the two to achieve the advantages of both, while avoiding the cons of each. However, an inexpensive, sensitive, and reliable SERS substrate is still needed.

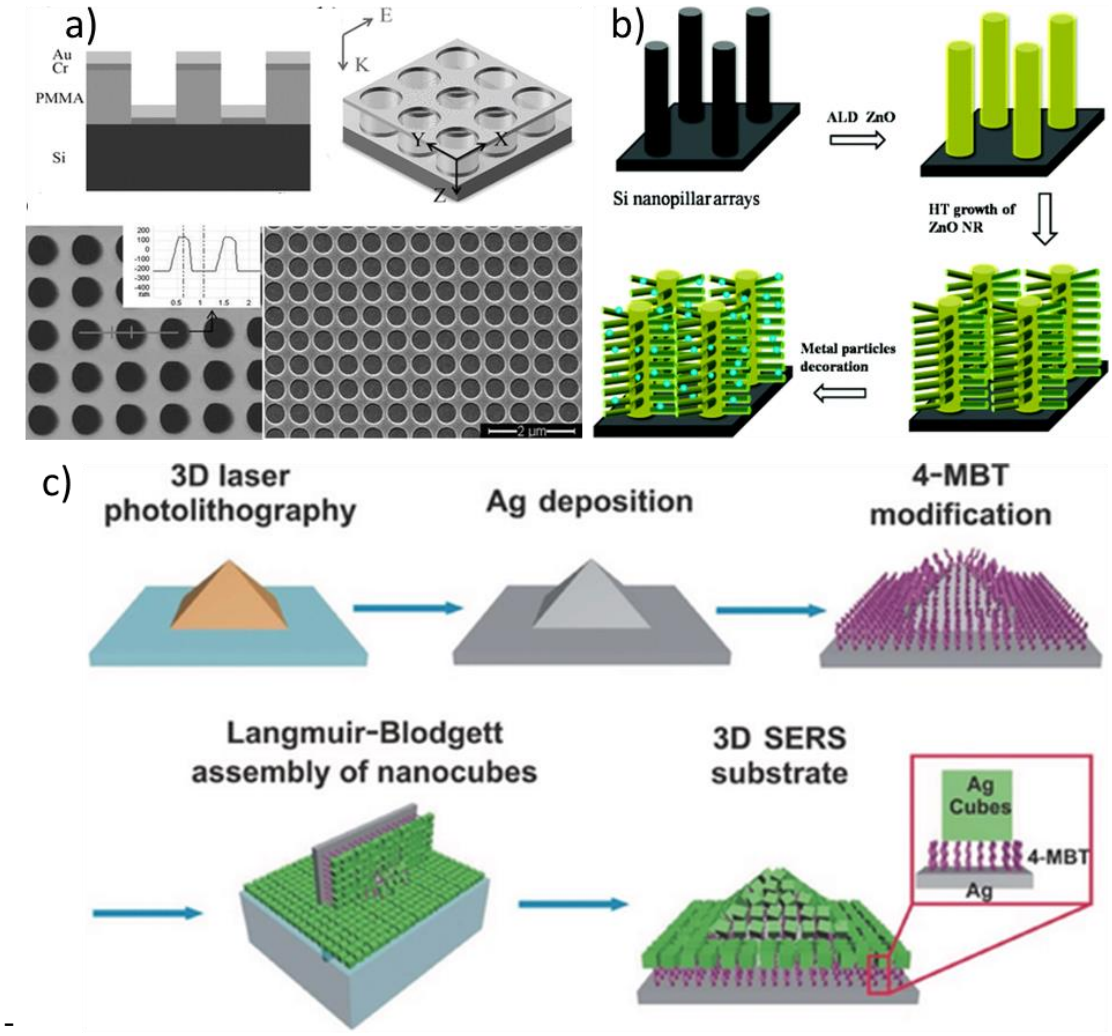

Fig. 1.5: Examples of top-down SERS substrate fabrication[48-50].

1.4 Chemometric Applications

Chemometrics is the application of data extraction techniques for the understanding of chemical processes. There are several common methods of chemometrics: feature extraction techniques to reduce the dimensionality of the data, regressionary techniques to find correlations between variables, and classification techniques to separate data into distinct groups. These techniques, and others, have been applied to aid in fluorescence[52-54] and SERS[55-57] sensing. The implementation

of these techniques can further improve sensitivity and selectivity, and aid in detection. However, due to the variability of data sets and experimental systems, no one method is best for all applications. Thus, when applying chemometrics to analyze data, it is wise to employ several methods to achieve optimal analysis. While analytical methods enable better signal extraction, physical and optical means of signal enhancement are still necessary to achieve sensitive sensing.

1.5 Photonic Crystals

1.5.1 Structure and Photonic Properties

Photonic crystals are periodic, dielectric material with interesting photonic properties. Photonic crystals can be one-dimensional, by stacking alternating dielectric materials; two-dimensional, by creating periodic porous structures or checkerboard patterns with dielectrics; or three-dimensional, by using multiple checkerboard patterns or periodic bubbles within a material. Photonic crystals are truly interesting when they possess a photonic band gap in which a range of frequencies are forbidden from existing within the structure without the existence of a defect[58]. By engineering the periodic structure of the photonic crystal and rationally designing a defect, excellent manipulation of light can be achieved resulting in novel applications. Considering the two-dimensional photonic crystal, a point defect can result in a microcavity with high optical enhancement[59-61] and a line defect can be used as a waveguide to direct light[62-64] as shown in Fig. 1.6 below. Furthermore, photonic crystals can be used to focus light[65-68]. This tunability and control enables extraordinary manipulation of

light. The utilization of photonic crystals has been applied to various optical sensing techniques, including fluorescence and SERS.

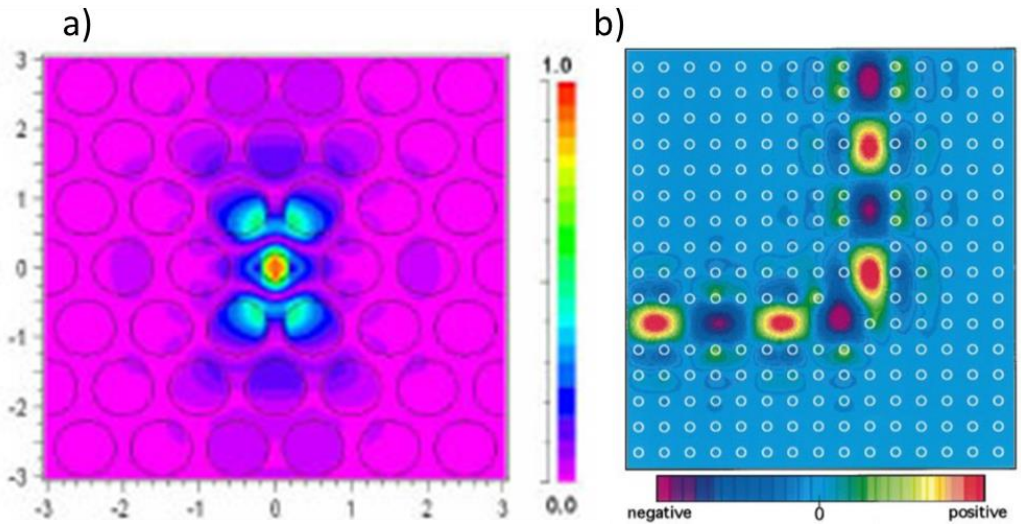

Fig. 1.6: Examples of point (a) and line (b) defects demonstrating manipulation capabilities of photonic crystals [60, 62].

1.5.2 Effect and Applications with Fluorescence Sensing

Photonic crystals can affect fluorescent molecules on or near its surface in a number of ways, including guided mode resonance, Purcell enhancement, and coherent scattering effects. Guided mode resonance (GMR) enhances fluorescence when resonant modes within the structure strengthen the optical field and result in greater light-analyte interaction and thus, greater signal. The Purcell effect is attributed to an enhanced density of optical states, which results in shorter fluorescence lifetime and increased efficiency[69]. Photonic crystals are capable of trapping emitted light from a fluorophore within its structure into resonant modes. These modes “leak” out of the structure and the photonic crystal can be designed to essentially allow preferential angular emission of the fluorescence, thus optically focusing the light and strengthening

the signal[70]. Lastly, the large surface area-to-volume ratio enables analyte aggregation. These enhancements have been employed in the detection of DNA[71], cancer biomarkers[72], explosives[73], and metal-ion recognition[74] to name a few. An example is shown in Fig. 1.7a.

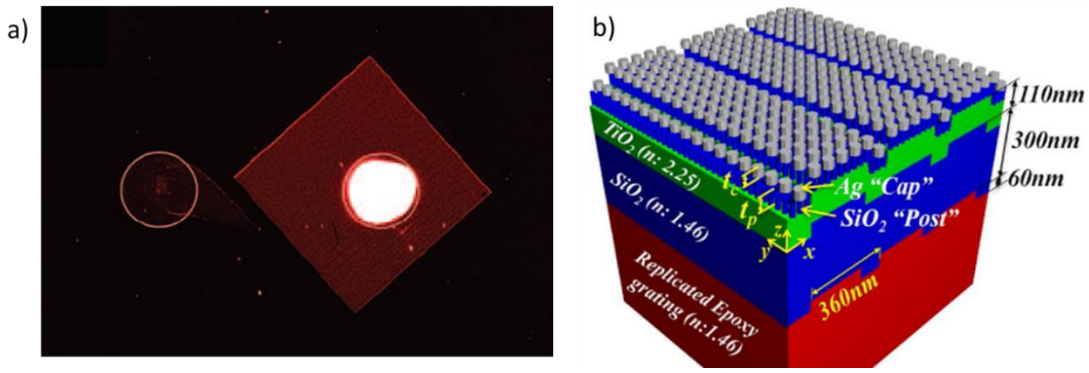

Fig. 1.7: Demonstration of fluorescence on and off photonic crystal (a)[70]. SERS substrate utilizing photonic crystal enhancements (b)[75].

1.5.3 Effect and Applications with SERS

SERS also benefits from the GMR discussed in the previous section, and the analyte concentration factor. Using these enhancements, SERS with photonic crystals have been investigated, an example of which is shown above in Fig. 1.7b[75, 76]. Photonic crystal-enhanced SERS has been applied to the detection of multiplex bioassays[77], cancer proteins[78], surface chemistry monitoring[79], and creatinine[80].

1.5.4 Shortcomings of Photonic Crystals

While photonic crystals provide the potential for enormous enhanced optical sensing, the limitations of photonic crystals can make them impractical. As has been

alluded to, photonic crystals can be highly customized to achieve the desired optical manipulation. As such, its design is an involved process, requiring time and expertise. Furthermore, most methods of photonic crystal fabrication require sophisticated and expensive equipment, as well as trained personnel for that equipment[81]. This often makes photonic crystal integration with optical sensors cost-prohibitive. What is needed is a means of integrating the enhancements from photonic crystals without being yoked with their weaknesses. An inexpensive photonic crystal easily integrated with optical sensors would enable higher sensitivity while maintaining manageable cost for wide-scale production. Nature has provided us with the perfect candidate.

1.6 Diatoms

1.6.1 Structure and Properties

Fig. 1.8: Image showing various species of diatoms[82].

Diatoms, a type of unicellular algae, are the most common algal group in most ecological systems, and are abundantly found in ocean, lakes, and rivers[83]. Diatoms possess nano-porous biosilica shells, called frustules, with various shapes and sizes ranging from 2-500 μm and are classified based on the symmetry of the porous structure[82, 84]. Some varieties of diatom frustules are shown above in Fig. 1.8. These micro-scale frustules, with hierarchal nano-scale pores, are excessively abundant and have an array of interesting properties. Diatom frustules have a large surface area-to-volume ratio and tailorable surface chemistry, are thermally stable, are chemically and mechanically resistive, and are biocompatible[85]. Beyond the physical and chemical properties of frustules, they possess many promising optical properties as well. Diatom frustules possess a photonic bandgap, couple light into distinctive waveguides, optically filter and diffract, are capable of lensless focusing, and experience GMR within their structure[86-91]. Select examples of these photonic properties are shown in Fig. 1.9 below. These ubiquitous algae possess naturally-occuring photonic crystal shells that can be harnessed to enable the sensing enhancements from photonic crystals without the difficulties of fabrication.

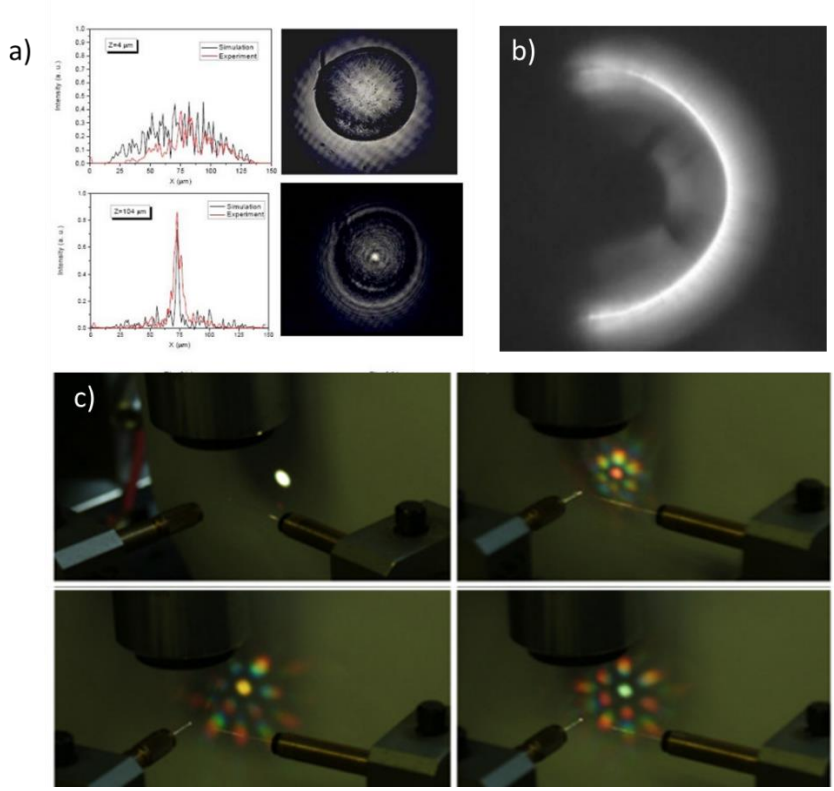

Fig. 1.9: Select examples of diatom optical properties including lensless focusing (a), guided waveguide modes (b) and optical diffraction (c)[86, 88, 89].

1.6.2 Applications of Diatoms

Because of the many advantages of diatoms and their frustules, they have been applied to optical detection regimes. Certain strains of diatoms have been shown to possess intrinsic photoluminescence (PL) capabilities[92]. This aspect of diatoms has been harnessed to create gas sensors by monitoring the change in PL[93, 94]. Additionally, by modifying the growth phase of the diatom frustule, the intrinsic PL can be manipulated further[95, 96]. The integration of diatom frustules with plasmonic nanoparticles for the fabrication of various SERS substrates has been investigated previously by our group[97-101] and others[102, 103]. They have also been used for fluorescence-based sensing[104, 105]. Fig. 1.10 shows some of these applications

below. The value of diatoms in optical sensing has been proven and now needs to be implemented for practical detections.

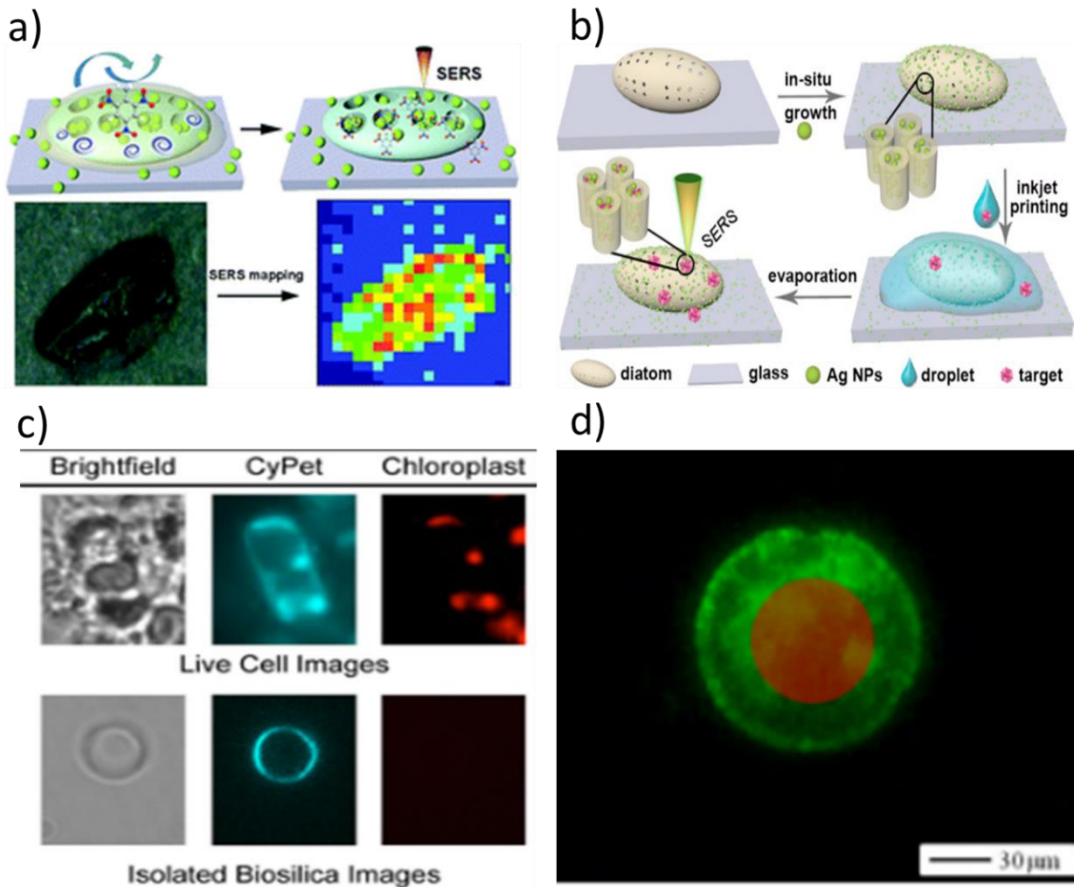

Fig. 1.10: Diatom optical sensing substrates for SERS (a,b) and fluorescence (c,d) [98, 101, 104, 105]

1.7 Dissertation Organization

The purpose of this dissertation is to outline our work in bringing diatom-based optical enhancements to practical sensing applications. Chapter 2 discusses the combination of diatom frustules with a sandwich immunoassay for enhanced fluorescence biosensing. The integration of the photonic crystal-like diatom with the bound and fluorophore-labeled analyte enables significant enhancements. Theoretical

calculations are performed to determine the expected fluorescence enhancement as well as experimental work to determine the overall enhancement. In this work, fluorescence spectroscopy and imaging are used to show the versatility of the diatom-fluorescence sensor and its potential for consumer grade cameras.

In Chapter 3, a diatom-based fluorescence imaging biosensor is fabricated for the detection of a cardiovascular disease biomarker in plasma. The fluorescence enhancement enables strengthened signals, and chemometric techniques are employed to further improve signal detection. Machine learning is used to screen samples for heart failure based on captured fluorescence images. The pairing of the fluorescence-enhancing diatom frustules, with the chemometric signal extraction, enables sensitive detection of the analyte.

In Chapter 4, a novel multi-scale substrate is presented for the rapid SERS detection of vapor-based analytes. Synergistic pairing of diatom frustules with core-shell nanoparticles afford the SERS sensor various features to achieve this detection. The diatom frustule enables enhanced optical fields on and near its surface while its porous structure allows for rapid analyte-substrate interactions. The metallic nanoparticle induces plasmons to further enhance the electromagnetic field. The porous silica shell around the metal nanoparticle captures and concentrates the vapor analyte near the plasmonic surface, while also preventing oxidation of the metallic particle. This multi-scale SERS sensor is applied to the practical detection of explosive vapor.

Lastly, chapter 5 gives a conclusion and brief summary of this work.

Photonic crystal enhanced fluorescence immunoassay on diatom biosilica

Kenneth Squire, Xianming Kong, Paul LeDuff, Gregory L. Rorrer, and Alan X. Wang

Journal of Biophotonics

Onlinelibrary.wiley.com/journal/18640648

Issue 10

CHAPTER 2: PHOTONIC CRYSTAL ENHANCED FLUORESCENCE IMMUNOASSAY ON DIATOM BIOSILICA

To demonstrate the utility of diatoms in biosensing, this chapter highlights the pairing of the frustules with an immunoassay. Immunoassays are an integral part of biosensing, in which an antibody is used to selectively bind with an antigen. This gives the sensor excellent specificity and can be used to detect either the antigen or antibody depending on the configuration of the sensor. In this work, we use a sandwich-based sensor with an antibody bound to the frustule-populated substrate to selectively capture the antigen. A secondary antibody is labeled with a fluorophore and is used to tag the captured antigen. The attached fluorophore is the reporter molecule used to detect the antigen and its close proximity to the photonic crystal-like frustule results in enhanced fluorescence and thus improved detection using fluorescence spectroscopy and microscopy.

2.1 Background

Fluorescence biosensors have found applications in a broad range of fields due to their capacity for extremely high sensitivity, multiplex detection, and to cause little or no damage to the sample [106-109]. Two common modalities of fluorescence biosensing are fluorescence spectroscopy and fluorescence microscopy (imaging). Fluorescence spectroscopy is a highly sensitive detection modality and very well established. As was mentioned previously in Chapter 1, fluorescence spectroscopy is performed by exciting a sample with a light source and measuring the emitted fluorescence signals that are inherent to the target, or a fluorescent tag, using a

spectrometer. The fluorescence intensity is proportional to the amount of target molecules and, based on the profile and intensity of the spectra, enables detection and quantification to be performed [110-113]. Fluorescence microscopy is one of the most widely used biosensing mechanism due to the high sensitivity and spatial resolution [114-119]. Fluorescence microscopy operates similarly to spectroscopy but rather than measuring the fluorescence spectra with a spectrometer, an imager is used, such as a CCD or CMOS sensor array. Compared with fluorescence spectroscopy, which requires optical spectrometers, fluorescence microscopy can be performed with simple read-out equipment --- only requiring an optical filter and a camera. This, paired with the ease with which it can be performed, makes fluorescence microscopy a powerful biosensing technique. However, to achieve the desired high sensitivity with either modality, high grade electronics and optics are required. This limits the applications of these sensing methods in point-of-care diagnostics. In order to achieve practical detection limits with consumer grade electronics, efforts have been made to implement various optical setups with additional complexity [15, 16, 120]. An alternative approach is the improvement of the sensing substrate. Many works have been published focusing on the creation of sensor substrates capable of enhancing measured fluorescence signals using a variety of structures, including photonic crystals [121-124].

Photonic crystals are periodic dielectric materials that can be one, two or three-dimensional. For fluorescence sensing, photonic crystal features are capable of enhancing the local optical field intensity [91, 101]. Additionally, if a fluorophore is placed in proximity to a photonic crystal, it will experience enhanced emission due to the Purcell effect [69]. Such dual enhancement mechanisms, combined together, will

lead to photonic crystal enhanced fluorescence detection that can achieve high levels of sensitivity without the need for high-grade electronics or optics. Fabricating rationally designed photonic crystal devices usually requires sophisticated fabrication equipment [125, 126] and relatively high cost, although the concerns have been relieved significantly by new techniques such as nano-imprinting [127]. Cell cultivation is a conventional bioprocess that can provide an alternative approach for fabricating nanoscale photonic structures with low cost and less complexity.

Diatoms are unicellular marine organisms that have porous biosilica cell walls with dimensions on the order of ten microns, as described in Chapter 1. The porous nature of the diatom frustule gives it significantly more surface area than the glass surface while the two-dimensional periodic nanosized pores endow it with hierarchical nanoscale photonic crystal features [81, 128]. Our research group have previously shown the evaporation-based ability of diatoms to concentrate analytes [98]. We have also previously shown that diatoms are capable of enhancing the electromagnetic field on its surface for SERS sensing [91, 98, 101, 129] and an ultra-sensitive SERS immunoassay has been developed, achieving a detection limit of mouse IgG down to 10pg/mL [99].

In this chapter, a novel photonic crystal enhanced fluorescence immunoassay biosensor on diatom biosilica, represented in Fig. 2.1, is presented. The demonstrated enhancement in fluorescence spectroscopy signals achieves results greater than 100× in comparison to an equivalent non-diatom-based biosensor allowing detection down to 100 aM (14 fg/mL). Utilizing fluorescence microscopy, a 10× enhancement to the limit of detection is achieved compared to non-diatom sensors and a 27~2,700×

enhancement in a hot-spot counting method, achieving detection down to 1 fM (140 fg/mL). The fluorescence immunoassay in this work improved the detection limit by 100~1,000× compared with our previous SERS immunoassay, allowing for single molecule mouse IgG detection on diatom frustules. The effectively-enhanced fluorescence imaging, coupled with a simple hot-spot counting analysis method presented in this chapter proves the ability of diatom fluorescence immunoassay for highly sensitive biosensors and the great potential for point-of-care diagnostics.

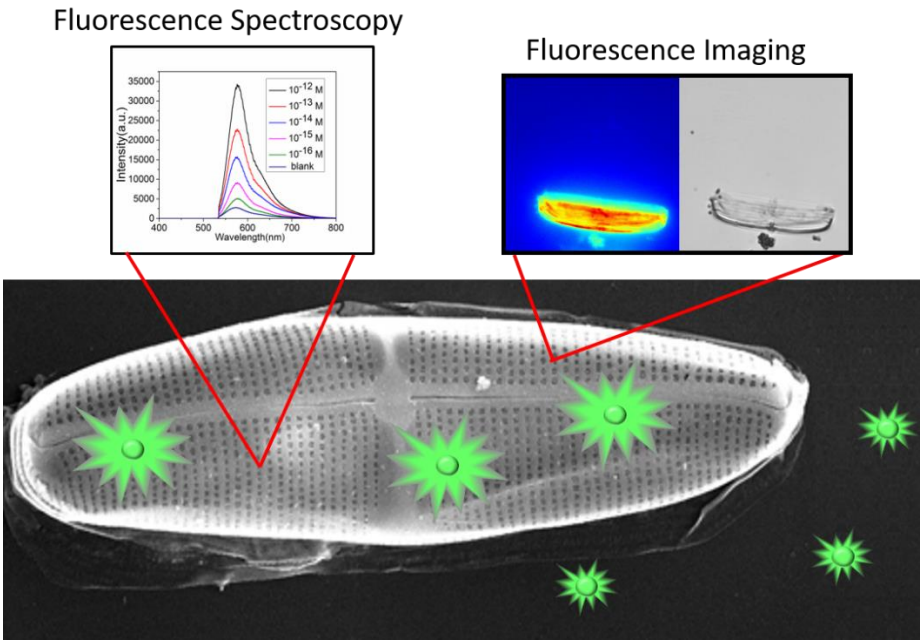

Fig. 2.1: Scanning electron microscope image of biosilica diatom frustule that enables significant enhancement of fluorescence spectroscopy and fluorescence image.

2.2 Theoretical Investigation of Fluorescence on Diatoms

2.2.1 Diatom Fluorescence Simulation

As discussed in Chapter 1, two mechanisms are capable of enhancing the fluorescence signal of a fluorophore on diatom. The first mechanism enhances the excitation while the second intensifies the emission. The enhanced excitation comes from a strengthened local optical field on the surface of the photonic crystal. Incident light induces resonant modes within the structure that, in turn, increase the optical field on the surface which in turn causes greater excitation of the fluorophore [70, 130]. This has been investigated previously by our research group and the diatom structure has been theoretically shown capable of enhancing the excitation intensity by 10× [98]. The enhanced emission comes from an increased emission rate due to the Purcell effect [69, 131]. When a fluorophore is placed on a photonic crystal slab, the density of optical states increases, resulting in a greater emission rate from the fluorophore.

To explore the enhanced emission of fluorophores on diatom surface, we performed a finite-difference time-domain (FDTD) analysis. The structure is modelled after the *Pinnularia sp.* diatom which we used in our experiments. The model is comprised of a silica slab with periodic air holes to simulate the pores. The dimensions of the simulated structure were chosen according to dimensions found from the SEM image of diatoms [98]. The pores are 160 nm in diameter with nanoscale features at the bottom. They are two-dimensionally periodic with a period of 300 nm along the major and minor axes of the structure. These dimensions are shown in Fig. 2.2a and b. The

structure is 15 µm × 5 µm which is similar to the actual size of the diatoms. This structure was used to simulate the Purcell effect of the diatom frustule.

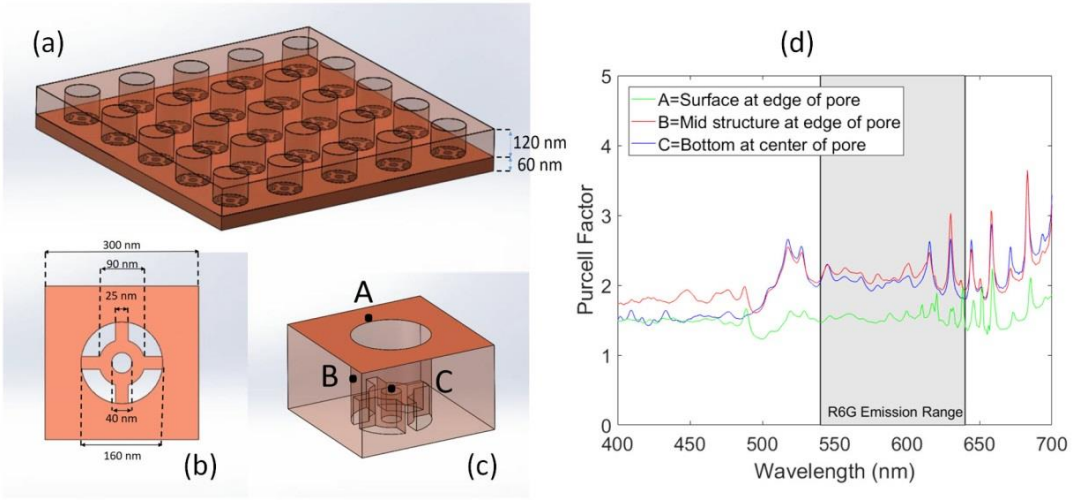

Fig. 2.2: (a) Simulated slab structure with 5×5 array of nanopores; (b) enlarged view of the nanopore with geometric parameters; (c) placement of fluorophores in diatom frustules; (d) the Purcell effect simulation results at the three points within a unit cell as a function of the wavelength

As the Purcell effect is related to the emission of a fluorophore, a single electric dipole representing the emission of a previously excited fluorophore was used to simulate the Purcell effect. This dipole was placed at various points as shown in Fig. 2.2c to excite electric fields in the nano-structure. The Purcell factor was calculated from the dipole source as the ratio of the power emitted in the photonic crystal environment compared to that emitted in a homogenous material. The emission wavelength of the dipole was swept from 400-700 nm in order to acquire the structure's Purcell effect. In Fig. 2.2d, the Purcell factor is plotted with respect to the wavelength. The shaded region represents the emission region of R6G which is the fluorescence tag used in our experiment and represents the expected enhancement in our experiment. The simulation shows that when the fluorophore is near the nanopore, the power

emitted by a fluorophore is enhanced by 1.5-3× across our region of interest due to the Purcell effect. Overall, the fluorophores inside the nanopores (B and C in Fig. 2.2c) will experience stronger Purcell effect compared with that (A in Fig.2.2c) on the surface of the frustule.

For fluorescence biosensing, it is equally critical to efficiently collect the fluorescence signals. To address this concern, the far-field radiation patterns of a dipole on diatom and on glass were simulated. Simulating the radiation pattern of a fluorophore on diatom, as shown in Fig. 2.3a, shows that there are a few strongly focused radiation directions at large angles of 70˚ - 80˚, which is quite surprising. The reason is that a significant amount of the fluorescence emission from the fluorophore is coupled into the slab waveguide and emitted from the edge, which contributed to the large angle radiation. In reality, however, the surface roughness and curvature of the frustule (see Fig. 2.5 for details) will scatter these slab modes and homogenize the radiation in the solid angle. Nevertheless, we still investigated the radiation pattern within a 50˚ cone. Our fluorescence spectroscopy measurements were done using an objective lens with a numerical aperture of 0.75, which has a corresponding 50˚ half angle of acceptance directly above and normal to the sample. To investigate the collection efficiency of fluorescence light, the far-field radiation patterns are shown on diatom and glass in Fig. 2.3b-c respectively. As can be seen, the emission from the fluorophore on diatom is more intense than that found on glass and by averaging the collected intensity in both instances, the enhancement by diatom is calculated to be 1.7×. When combined with the enhanced excitation, we expect the total measured fluorescence enhancement from diatom to be on the order of 10×. This analysis applies

to single molecule or a few molecule sensing. If a large number of randomly distributed fluorophores emit light with random polarization, corresponding to the biosensing of high concentration analyte, we may not observe any dependence of the radiation on the direction. The fluorescence emission from both diatom and glass will be relatively homogenous.

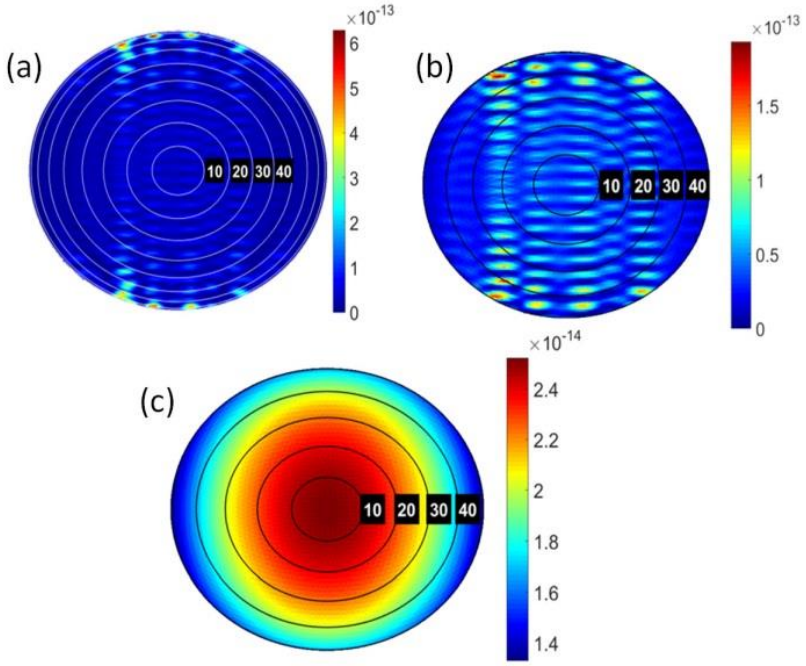

Fig. 2.3: Far-field radiation pattern of fluorophore on diatom (a), and radiation pattern inside the 50˚ solid angle on diatom (b) and glass (c).

2.2.2 Enhanced Surface Area Calculation

The average diatom diameter along the minor and major axis are 5 μm and 15 μm respectively. Using the SEM diatom image in our previous work[27], it was estimated there are approximately 1,200 pores in a diatom substrate with the pore being 120 nm deep. In our estimation we did not account for the smaller pores at the bottom

of each pore. The diatom footprint on glass is about 60 μm^2 and the surface area of the diatom is roughly 670 μm^2 giving us a surface area enhancement of roughly 11×.

2.3 Experimental Procedures

2.3.1 Instruments and Measurement Details

Scanning electron microscopy (SEM) images were acquired on FEI Quanta 600 FEG SEM with 15–30 kV accelerating voltage. Fluorescence spectra were acquired according to the method proposed by Aroca's group[132]. Briefly, we point to a diatom surface with the 50× objective lens, with the Horiba Jobin Yvon Lab Ram HR800 Raman system using the 532 nm laser line with a spot size of 2 μm. Fluorescence microscopy images were obtained using a 60x objective lens on an Olympus IX73 microscope equipped with a CY3 filter by Olympus as well. Excitation was achieved with a X-cite 120 LED fluorescence microscope light source set at 250 mW. The images were collected on a Hamamatsu Orca-Flash 4.0 LT with a 50 ms integration time for optical images and 500 ms integration time for fluorescence images.

2.3.2 Preparation of Diatom Biosilica

Diatom (*Pinnularia sp.*) biosilica were prepared according to the method previously reported with minor modification [98]. Briefly, diatoms were cultured in a container for one week. The diatom suspension was concentrated 10× through centrifuging and dispersed in sterile filtered artificial seawater and filtered with 20 μm mesh to separate cells. The diatom cell density was adjusted to 0.1×10^5 cells/mL for seeding. A coverslip was placed into a petri dish separately, and 15 mL of diatom cell suspension was cast onto the glass slides and incubated in a humidifier chamber for one

hour to deposit the cells on the coverslip surface. Then the coverslip with diatoms was put into a new petri dish, kept in a humidifier for 24 hours, and immersed in 70% ethanol (EtOH) for 4 hours, and soaked in pure EtOH for 4 more hours. The diatoms were dried in air and treated in a Novascan PSD-UVT UV ozone cleaner at 90 °C for one day. After that, the diatom substrate was ready for use.

2.3.3 Preparation of Diatom Fluorescence Immunoassay

The diatom biosensor was prepared as shown in Fig. 2.4. The diatom substrate was incubated in 15 mL of 0.05% aminopropyl-triethoxylsilane (APTES 98% purity) in 100% EtOH (v/v) for 6 hours at room conditions followed by washing with acetone and EtOH and drying with nitrogen gas. After that, the aminated diatom substrate was immersed in 15 mL of 2% (v/v) glutaraldehyde (GA) in phosphate buffer saline (PBS pH of 7.4) for 2 hours. The GA-modified diatom was washed thoroughly with double-distilled water three times to remove excess GA and again dried with nitrogen. The GA-activated surface was then reacted with 0.1 mg/mL of goat anti-mouse IgG in PBS buffer by drop casting 1 µL onto various points on the sensor and leaving at 4°C for 6 hours to get an antibody layer followed by another rinsing with PBS and water and drying with nitrogen. After this step, the sample was submerged in 1 mg/mL of bovine serum albumin (BSA) in PBS and left at room temperature for 6 hours to block the remaining GA-active surface to reduce the non-specific binding of the immunoassay. The antibody immobilized diatom substrates were rinsed with PBS and water, dried with nitrogen, and stored at 4°C for future immunoassay procedures.

The immunoassay procedure is similar to a standard sandwich protocol of the enzyme-linked immunosorbent assay (ELISA), as shown in Fig. 2.4. Briefly, 1 µL of

antigen (mouse IgG) at different concentrations was pipetted onto spots corresponding with immobilized goat anti-mouse IgG antibody on the diatom substrate. After 2 hours of immune recognition at room temperature, the substrate was rinsed with PBS buffer and water followed by a drying step with nitrogen. Next, 1 µL of goat-anti-mouse IgG labeled with rhodamine 6G (R6G) was pipetted onto the same spots of the substrate and kept at 4 ˚C for 4 hours and washed thoroughly with PBS buffer and water. The sensor was dried using nitrogen gas and was then ready for fluorescence measurements.

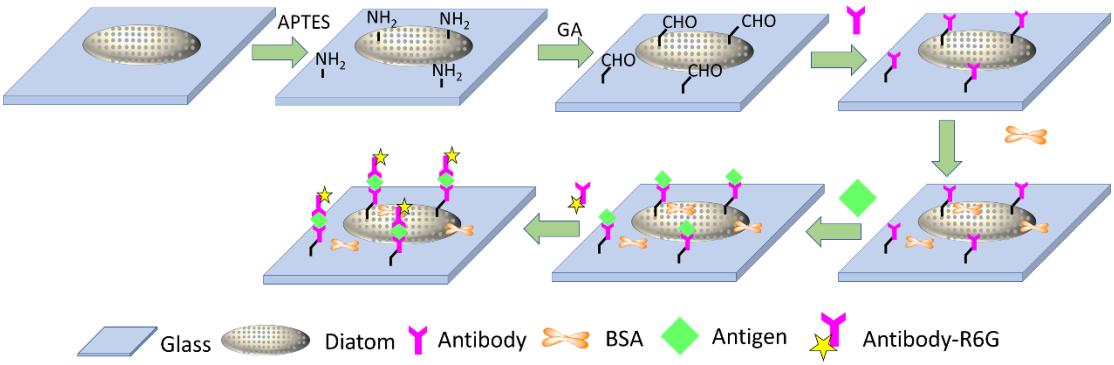

Fig. 2.4: Schematic illustration of the fluorescence microscopy immunoassay sensing on diatom photonic crystal biosilica.

2.4 Diatom-Enhanced Fluorescence Sensing

2.4.1 Fluorescence Spectroscopy

The morphology of the diatom photonic crystal biosilica was characterized by scanning electron microscopy (SEM). The SEM images of diatom are shown in Fig. 2.5a and b below. The semi-ellipsoidal cell dimension of diatom is around 25 µm along the major axis, 8 µm along the minor axis. The diatom biosilica consists of periodic two-dimensional nanopores (Fig. 2.5b) with a periodicity of 300 nm. At the floor of the pores, additional nano-features are present. The fluorescence enhancement effect of the diatom photonic biosilica was investigated using R6G as the typical probe molecule

due to its strong fluorescence feature. First, 1 μL of R6G aqueous solution was cast onto the glass-diatom substrate. After drying in air, the fluorescence image of the glass-diatom substrate was obtained under a fluorescence microscope with 532 nm laser as the excitation light. As shown in Fig. 2.5c, the orange color from the diatom photonic biosilica is brighter than that from the glass slide. The contrast between the diatom and glass was attributed to the photonic crystal enhancement effect from diatom frustules. The fluorescence enhancement effect of diatom photonic biosilica was further verified by fluorescence spectra as shown in Fig. 2.5d. The sample used to collect the fluorescence spectra was the same one that was used for fluorescence image acquisition in Fig. 2.5c. The intensity of the fluorescence spectra of R6G from diatom photonic biosilica are almost 10× that from the glass slide, which is in accordance with the fluorescence imaging result.

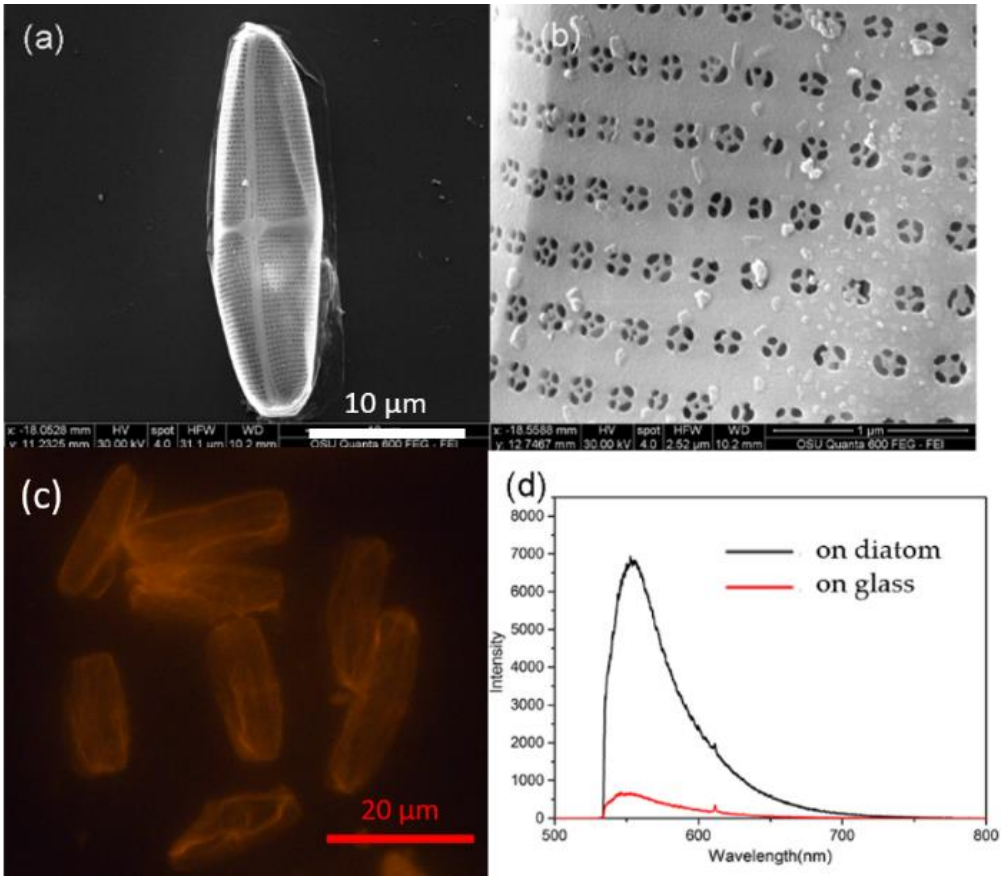

Fig. 2.5: SEM images of (a) an overview of a single diatom frustule, (b) primary pores on a frustule, (c) fluorescence image of 1 µL of R6G (10-6 M) dropped onto the glass-diatom substrate, (d) fluorescence spectra of 1 µL of R6G (10-6 M) solution dropped onto the glass-diatom substrate.

The target antigen, mouse IgG, varying from 1 pM to 0.1 fM, was applied to the sensor as outlined in the previously stated immunoassay protocol section. Fig. 6a shows the fluorescence spectra of the R6G-labeled immunocomplex on diatom frustules with different antigen concentrations. It can be observed that the intensity of the peak decreases gradually with the decrease of antigen concentrations. When the concentration of mouse IgG decreases to 0.1 fM, the fluorescence intensity at 575 nm is still easily observed compared to the control sample. In contrast, on the glass slides, when the concentration of mouse IgG decreases to 10 fM, it is difficult to distinguish

the fluorescence signal of R6G from the control as shown in Fig. 6b. This demonstrates a 100× enhancement from our sensor. The superior performance can be attributed to the photonic crystal effect of the diatom frustules, from both enhanced excitation and the Purcell effect. It is interesting to point out that there is not any trace of Purcell effect modulation as the simulation results in Fig. 2.2d in the experimental spectra. This is because the diatom structure is not perfectly periodic over a long range as the simulation model. Therefore, the local Purcell factor varies from diatom to diatom and even across the diatom frustule. This creates an averaging effect of the Purcell effect which results in the absence of this modulation.

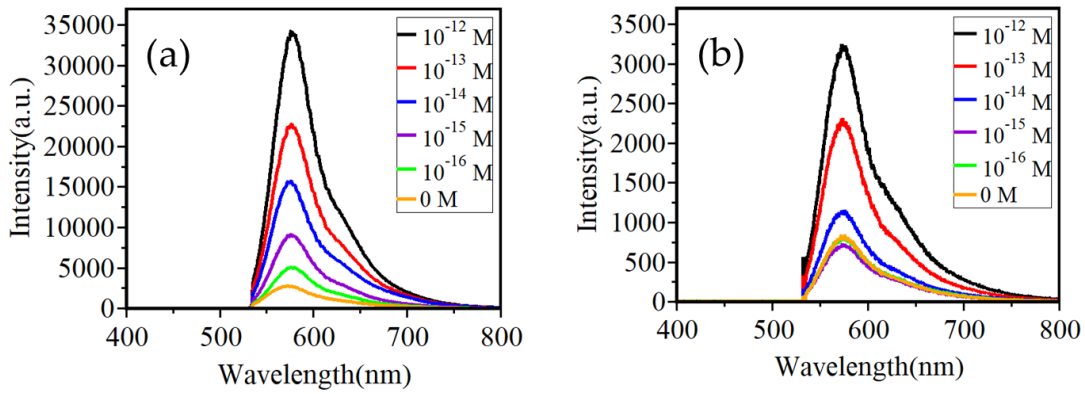

Fig. 2.6: Fluorescence spectra on diatom (a) and glass (b) for different concentrations of IgG.

2.4.2 Fluorescence Imaging Average Intensity Analysis

To further explore the capabilities of our sensor, optical and fluorescence images were taken of diatoms using a fluorescence microscope. Varying concentrations of antigen were imaged, and it is observed that the fluorescence intensity decreases as the antigen concentration decreases as shown in Fig. 2.7. The analysis of multiple images at each concentration was performed by calculating the average fluorescent

intensity of each pixel on diatom and on glass in Matlab. The average intensities were used to compute the enhancement due to the presence of diatoms. First, the noise due to the dark noise of our camera as well as nonspecific binding of the antigen to our sample was determined. This was done by calculating the average intensity on diatom of the fluorescent image for each control image. The fluorescent intensity values for multiple control samples were then averaged to find the average noise floor of diatoms. This process was repeated for the glass substrate. Similar averaging was performed for each concentration and the average intensity on diatom and on glass was found.

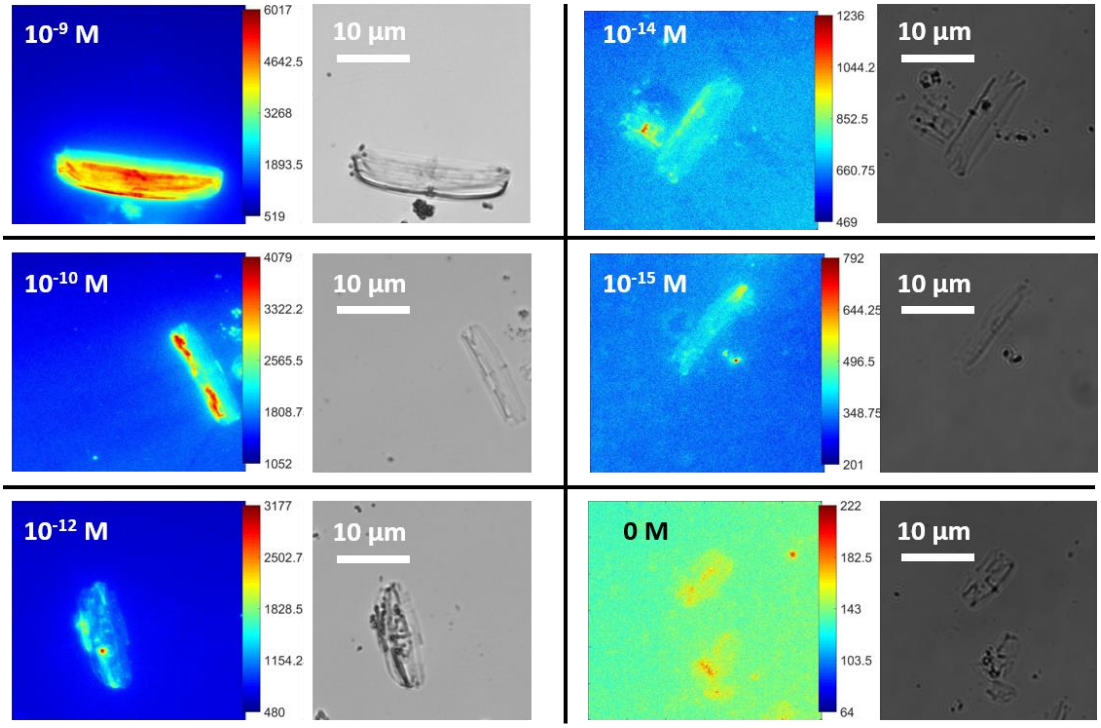

Fig. 2.7: Fluorescence and optical images of diatoms at varying concentrations of R6G-tagged mouse IgG.

To demonstrate the reproducibility of our diatom-based device, we fabricated two batches of three sensors in parallel for a total of six sensors. The immunoassay was performed according to the process described in this paper, using an antigen concentration of 10 nM mouse IgG. Ten representative images were taken and analyzed and the average fluorescence on diatom was calculated for each image. The standard deviation and average for the sample were then calculated and the results are shown in Fig. 2.8 below. As can be seen, the average fluorescence on diatom show practical levels of reproducibility.

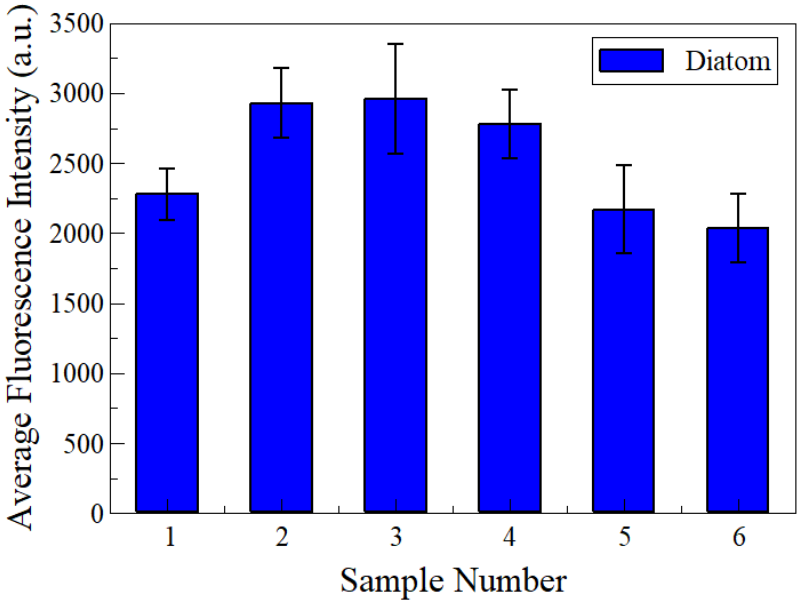

Fig. 2.8: Average and standard deviation of the fluorescence on diatom showing the reproducibility of our diatom-based sensor.

The fluorescence intensity on diatom and on glass was then analyzed and the average at each concentration, along with error bars of the standard deviation, was plotted with respect to concentration as shown in Fig. 2.9a. The noise floor was defined as 3× the signal-to-noise ratio (SNR). The SNR was defined as shown in Eq. 2.1 below, where I_{signal} is the average fluorescence intensity for a given concentration and I_{blank} is the average fluorescence when there is no antigen present.

$$SNR = \frac{I_{signal}}{I_{blank}} \tag{2.1}$$

The SNR with respect to concentration on diatom and on glass are plotted in Fig. 2.9b. The enhancement factor due to diatom was calculated according to Eq. 2.2 where $I_{avg,d}$ is the average fluorescent intensity on diatom and $I_{avg,g}$ is the average intensity on glass. The enhancement factor was plotted with respect to concentration in Fig. 2.9c.

$$EF = \frac{I_{avg,d}}{I_{avg,g}} \tag{2.2}$$

Using this methodology, a limit of detection of 10 fM was achieved, as shown in Fig. 2.9a. A maximum SNR of 50 was achieved on diatom and an enhancement as high as 6× from diatom was achieved at antigen concentration of 10^{-9} M.

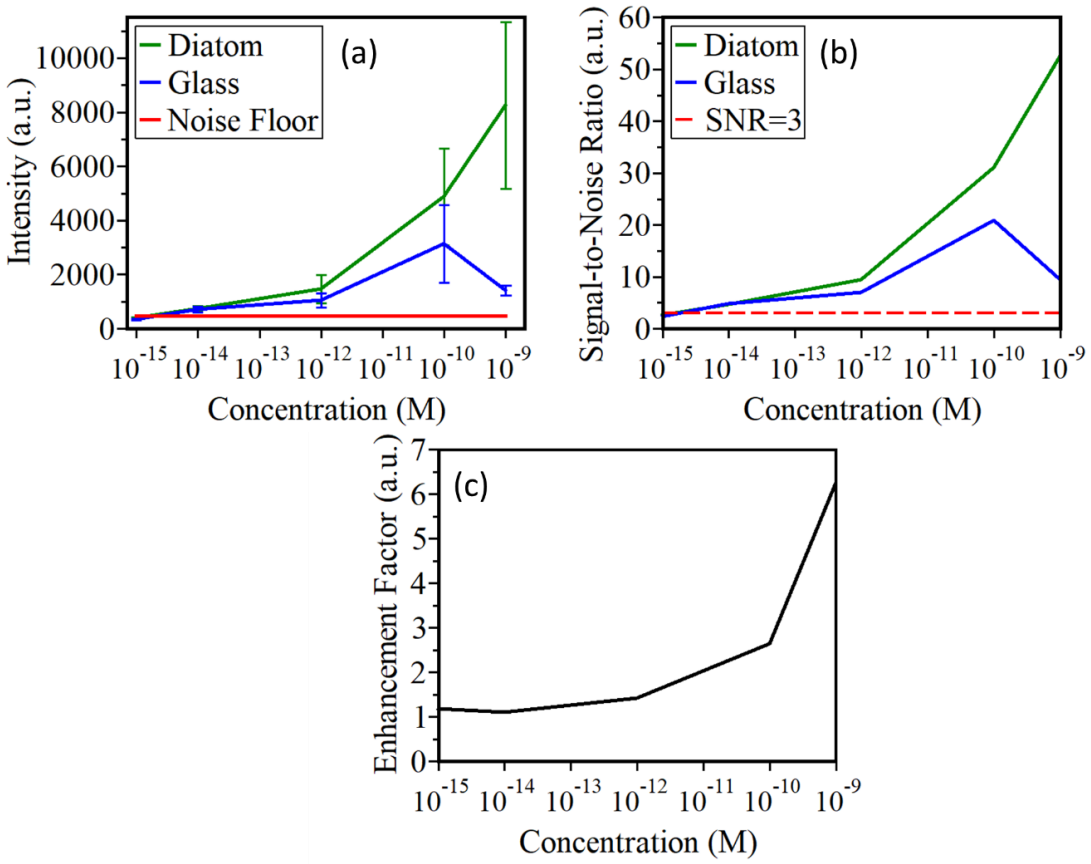

Fig. 2.9: Average fluorescence on diatom and glass with error bars, along with the noise floor (a). The SNR is shown for diatom and glass with respect to concentration with a line representing SNR = 3 (b). The enhancement factor is also calculated at each concentration (c).

As the concentration decreases, so do the SNRs, as well as the enhancement factor from diatom. This can be easily understood. At higher concentrations, the analyte is abundant and is considered to be uniformly dispersed across the sample. However, at lower

concentrations, such as 1 fM, the density of fluorophores is closer to single molecule levels. At this concentration, the molecules are no longer uniformly dispersed and by averaging the whole diatom, the enhancement factor of the fluorescence signals is diluted.

2.4.3 Fluorescence Imaging Hot-Spot Analysis

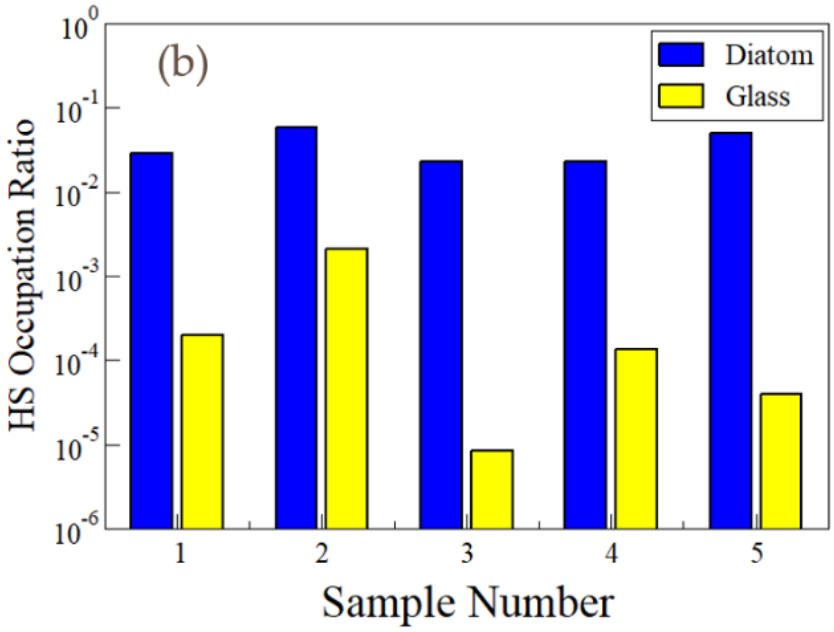

Fig. 2.10: The hot-spot occupation ratio on diatom and glass plotted on a log scale for several samples with analyte concentration at 10^{-15} M.

As a more accurate analysis method, a hot-spot counting analysis was performed rather than analyzing the average intensity. A hot-spot was defined as a pixel whose intensity is three times the noise floor. Counting the number of hot-spots, the hot-spot occupation ratio is calculated on the glass and the diatom by using Eq. 2.3 where R is the hotspot occupation ratio, N_{hs} is the number of pixels that are hot-spots and N_p is the total number of pixels.

$$R = \frac{N_{hs}}{N_p} \tag{2.3}$$

Performing this hot-spot counting analysis at several concentrations, we pushed our limit of detection down to 1 fM, achieving detection an order of magnitude lower than the large area averaging technique. As is shown in Fig. 2.10, a massive enhancement due to the diatom was achieved, ranging from 27× up to 2,700×. Due to the ultra-low concentrations, the non-uniformity of the analyte leads to large variations in hot-spot occupation ratio. An image may contain a couple of fluorophores or there may be none. For our measurements, diatoms with fluorescent signals were imaged and then compared to their surrounding glass. Because diatoms exhibiting fluorescence were selectively imaged, the variation in hot-spot occupation ratio on diatom is relatively small. However, the hot-spot occupation ratio on glass surrounding the diatom varies largely between samples as can be seen in Fig. 2.10. This large variation on glass is caused by the non-uniformity of the analyte and is responsible for the wide range of enhancement factors. Nevertheless, the enhancement factor of more than 20× is guaranteed for single-molecule detection.

Image analysis of the fluorescence images shows that the pixel intensity from fluorescence on diatom and on glass both follows normal distribution, as shown in Fig. 2.11. However, the distribution on diatom is shifted to higher intensities exhibiting nearly 20% greater fluorescence due to the enhancement from the Purcell effect, the enhanced local optical field and greater surface area. Since the hot-spots are defined as any pixel above 3× the fluorescence noise, the hot-spot occupation ratio is much larger on diatom than on glass as shown in Fig. 2.11a and b. Requiring at least a hot-spot occupation ratio of at least 1% for detection, we achieve detection limits of 1 fM on diatom and 10 fM on

glass. This 10× improvement to the limit of detection is attributed to the enhancements from diatom.

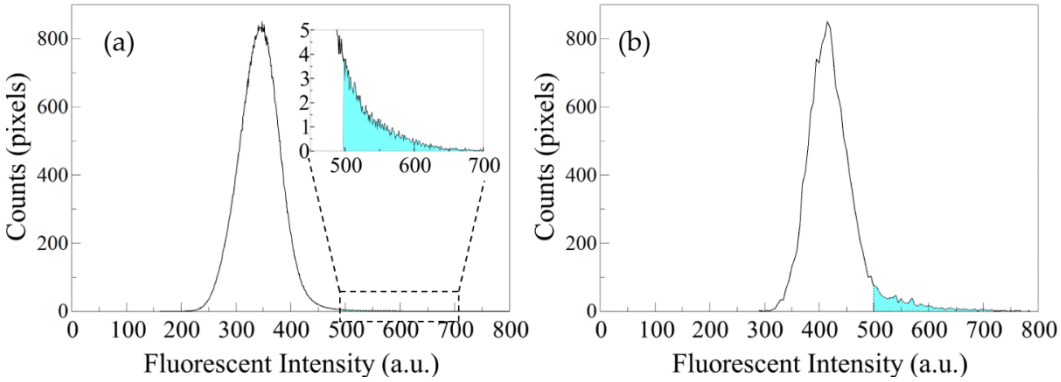

Fig. 2.11: The distribution of pixel fluorescent intensities on glass (a) and on diatom (b) with a shaded region represents the portion that are hot-spots.

2.5 Summary

Photonic crystal-enhanced fluorescence spectroscopy and fluorescence imaging on diatom biosilica were demonstrated. The porous nanostructures and the photonic crystal features of diatoms are combined in a synergistic way to achieve ultra-sensitive immunoassay detection. Enhancements of 100× and 10× better detection limit with fluorescence spectroscopy and fluorescence imaging respectively were achieved. The limit of detection of the mouse IgG goes down to 10^{-16} M (14 fg/mL) and 10^{-15} M (140 fg/mL) for the two respective detection modalities, virtually sensing a single mouse IgG molecule on each diatom frustule. The effectively enhanced fluorescence imaging, in conjunction with the simple hot-spot counting analysis method used in this paper, proves the great ability of diatom fluorescence immunoassay to enhance fluorescence and achieve high sensitivity. This sensor is ideal for point-of-care fluorescence microscopy diagnostics,

particularly cell phone-based diagnostics. Cell phone-based biosensors have gained a lot of attention in recent years [15, 16, 120, 133, 134] and the advantages of such a system are obvious, particularly in rural and low-income areas as well as developing nations. The diatom photonic crystal enhanced fluorescence immunoassay can be used as a versatile device for various biologically important diagnostics, particularly in rural and underdeveloped areas and we will investigate this in the next chapter.

Photonic Crystal-Enhanced Fluorescence Imaging Biosensor for Cardiovascular Disease Biomarker Screening with Machine Learning Analysis

Kenneth J. Squire, Yong Zhao, Ailing Tan, Kundan Sivashanmugan, Joseph A. Kraai, Gregory L. Rorrer, and Alan X. Wang

Sensors and Actuators B: Chemical

Sciencedirect.com//journal/sensors-and-actuators-b-chemical

Volume 290

CHAPTER 3: PHOTONIC CRYSTAL-ENHANCED FLUORESCENCE IMAGING BIOSENSOR FOR CARDIOVASCULAR DISEASE BIOMARKER SCREENING WITH MACHINE LEARNING ANALYSIS

Having demonstrated the diatom's ability to enhance immunoassay fluorescence, the frustules are applied to the practical detection of the cardiovascular disease biomarker. Again utilizing a sandwich immunoassay, the enhanced detection capabilities of our sensor are paired with machine learning techniques. Together, sensitive and selective sensing of the cardiovascular disease biomarker are achieved and an effective screening algorithm is developed for aiding in the diagnosis of heart failure through the detection of the biomarker in plasma.

3.1 Background

According to the American Heart Association, in 2009, one in nine deaths cited heart failure (HF) as a contributing cause and in 2016, about 5.7 million Americans suffered from HF[135]. Total direct medical costs of HF in the US are projected to be $42.9 billion by 2020[136]. The need for accurate, inexpensive and early detection of HF is critical. When an individual has HF, the myocardial wall experiences stress and the hormone N-terminal proBNP (NT-proBNP) is released into the bloodstream and is recommended by the European Society of Cardiology (ESC) as an analyte to aid in the diagnosis of HF. The ESC directs that the upper limit of normal levels of the biomarker is 125 pg/mL and values lower than this can be used to rule out the possibility of HF[137]. Levels of NT-proBNP >450 pg/mL can be used to "rule in" HF[138].

The most common method of detecting NT-proBNP is by performing electrochemiluminescence (ECL) paired with an immunoassay. This method is recommended and used by respected institutions such as the Mayo Clinic[139]. ECL is effective, but it also requires expensive, sophisticated instrumentation and highly trained personnel. Fluorescence imaging, often paired with an immunoassay, is a biosensing technique that could be used in place of ECL. The immunoassay allows for high degrees of specificity due to the specific antibody-antigen interaction, allowing capture or separation of the analyte from the surrounding sample matrix. Fluorescence imaging sensors are rationally designed such that the presence of the analyte induces a change in fluorescence intensity, which is caused by specific analyte labeling with a fluorophore[140-142] or quenching inherent sample fluorescence[143-145].

As previously explained in Chapter 2, fluorescence imaging employs imagers, either consumer or laboratory grade, to monitor the change in fluorescence intensity. The intensity depends on the concentration of analyte present and, in some applications, detection and quantification can be achieved down to single molecule levels[146, 147]. Furthermore, fluorescence imaging can perform large area measurements while maintaining spatial information, thus allowing parallel sensing of multiple sensors for high-throughput applications. This powerful sensing technique has been applied to the detection of NT-proBNP[148, 149]. However, Lee et al. achieved detection of the biomarker only to 5 ng/mL, which is significantly above clinically relevant levels[148]. Wilkins et al. successfully detected NT-proBNP down to 50 pg/mL but required high efficiency quantum dots containing toxic cadmium sulfide to achieve this level of detection[149]. Therefore,

safe detection of NT-proBNP at clinically relevant levels of detection still requires further fluorescence signal enhancement.

In recent years, plasmonic structures such as nanoparticles, nanorods and other nanostructures have been employed to enhance the local electromagnetic field resulting in enhanced fluorophore excitation[150-152]. These techniques provide fluorescence enhancement but often suffer highly localized effects. Uniform photonic crystals have also been used as suitable fluorescence enhancing substrates due to their optical field enhancement and large sensing area-to-volume ratio[127, 153, 154]. However, rationally designed photonic crystals generally require cleanroom technologies to fabricate and often experience issues with surface functionalization[125, 126]. Engineered fluorophores, such as quantum dots, have been fabricated and used to achieve higher quantum efficiencies and stronger fluorescence, but these often require toxic materials such as cadmium[155, 156] and suffer from instability[157, 158].

Other than the concern of sensitivity, random fluctuation of the fluorescence signals brings a great challenge for analyte quantization. Feature extraction, statistical regressions and classifications are the main tasks of statistical chemometric methods, such as machine learning, with each algorithm being used to improve the clarity of a dataset for quantitative and qualitative analyses. Feature extraction techniques, such as principle component analysis (PCA), reduce the dimensionality of data, enabling more effective visualization and analysis. Regression analyses, like partial least squares regression (PLSR) or support vector regression, are common analytical techniques that have been applied to fluorescence biosensing and allow for the creation of accurate calibration curves to quantitatively predict

the concentration of an analyte[159-161]. Classification techniques such as k-nearest neighbors (kNN) or support vector machines (SVM) can be used to train a model capable of accurately grouping data points by similar characteristics and are effective for qualitative and semi-quantitative classification. Implementation of classification techniques have enabled successful analyte detection with fluorescence biosensing[162-164].

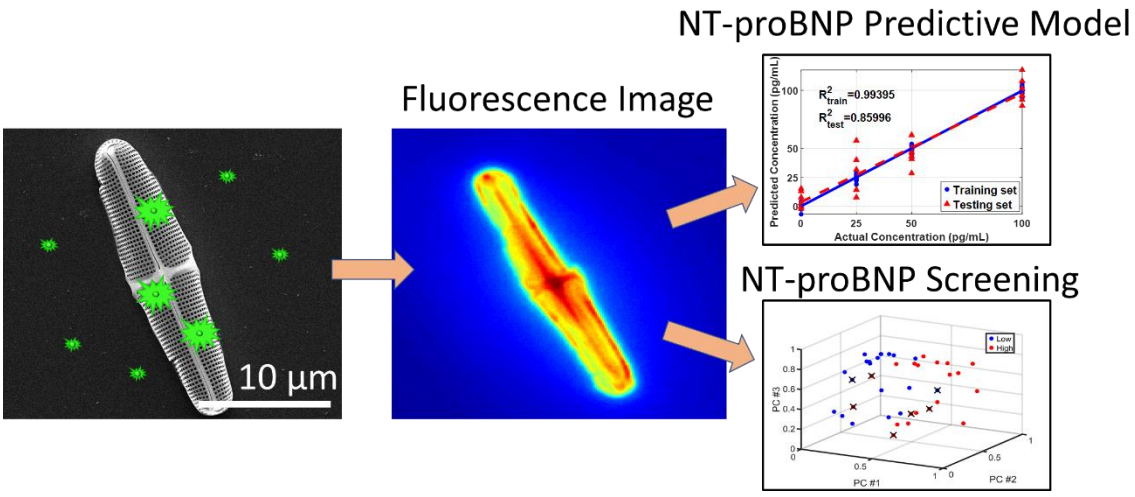

Fig. 3.1: Representative figure demonstrating the approach used for NT-proBNP sensing

In this chapter, a photonic crystal-enhanced fluorescence imaging immunoassay biosensor capable of detecting clinically relevant levels of NT-proBNP is demonstrated and machine learning-assisted analyte quantization is implemented, as illustrated in Fig. 3.1 above. Different than artificial photonic crystals made by top-down nanofabrication techniques, our cardiovascular biomarker sensor employs diatom biosilica to enhance the fluorescence signal. Diatoms are single-celled microalgae that biologically fabricate porous silica shells called frustules. The periodic, nanostructured pore arrays of diatom frustules can enable natural photonic crystal behavior. The biosensor fabrication begins with cost-effective algae cultivation to grow diatoms. Cellular organic matter is removed,

and the isolated biosilica shells are deposited onto a glass slide as a dispersed monolayer thin film. A typical sandwich immunoassay process is performed to functionalize the substrate with antibodies, selectively capturing the analyte NT-proBNP and tagging it with fluorophore-labeled antibodies. The diatom biosilica integrated with our sensor offers significant fluorescence signal enhancement for clear imaging. Following the data acquisition, a simple arithmetic average fluorescence intensity analysis is performed, resulting in the detection of NT-proBNP to clinically relevant levels but with difficulty in differentiation at lower concentrations. To improve this, feature extraction and regression analyses obtain an excellent calibration curve for the NT-proBNP concentration with good linearity and differentiation. When challenged by 24 test images, a validation R^2 value of 0.85 and a predictive root mean square error of 14.85 was achieved, allowing for good analyte quantification. Lastly, we detect NT-proBNP in human plasma and use feature extraction and classification to qualitatively distinguish between high and low concentrations of NT-proBNP, creating a screening mechanism for diagnostically ruling in or out heart failure. The classification model was trained using 160 fluorescence images and when applied to 40 test images, achieves excellent specificity of 91%, and decent accuracy and sensitivity of 78% and 64% respectively. Therefore, the synergistic integration of the photonic crystal-enhanced fluorescence imaging immunoassay with machine-learning analysis techniques has led to effective detection of cardiovascular biomarker NT-proBNP, which can play a key role for screening individuals with heart failure risk.

3.2 Experimental Setup and Analytical Methods

3.2.1 Diatom Culturing and Isolation

Pinnularia sp. were cultured according to the method previously described with minor changes[165]. The diatoms were obtained from UTEX Culture Collection of Algae (UTEX #B679). They were cultivated in 100 mL of Harrison's Artificial Seawater Medium with Guillard's f/2 nutrient enrichment[166]. Incubation was performed at 22° C with light intensity of 100 $\mu E/m^2 \bullet sec$ with a photo cycle of 14 hours light and 10 hours dark. Diatoms were subcultured every 21 days with a 10:1 dilution in fresh medium. Cell densities when harvested were ~10^6 cells/mL. This was measured using a Beckman Coulter Z2 Particle Counter using a 6 µm threshold with 100 µL of cell suspension diluted in 10mL diluent (10 g/L sterile-filtered NaCL, 171 mM).

Isolation was achieved using an adapted method described in our previous work[165]. *Pinnularia sp.* that had been growing for three weeks was allowed to settle to the bottom. The solution was decanted and centrifuged for 20 min at 2500 g. The packed cells were washed in 40 mL nanopore water three times to remove salts from the culture medium. It was re-suspended in 1 mL of 8.1 M HCl and gently mixed. The diatoms settled again, and the supernatant was removed. The oxidation treatment was performed by adding 5 mL of the concentrated diatoms to 32 mL of 0.76 HCl in 28% (v/v) H_2O_2 and mixing. This was allowed to sit for 72 hours with daily mixing. The oxidation treatment was performed twice, after which the supernatant was removed, and the diatoms were re-suspended in 40 mL H_2O. The mixture was allowed to settle, and supernatant was removed.

This aqueous washing process was repeated two more times before re-suspending in anhydrous methanol. Again, the mixture was allowed to settle, and the supernatant was removed. The crude frustule isolate was washed with methanol twice more. The isolated diatom frustules were stored in methanol at room temperature.

Coverslips were populated with diatoms by first sonicating the coverslips in 1% (v/v) solution of Liquinox detergent for 60 min at 40° C. The coverslips were rinsed using Nanopure H_2O and 100% ethanol followed by drying with nitrogen gas. They were then placed in a UV-Ozone Cleaner at 90° C for 30 min. The coverslips were placed in a petri dish on a hot plate set to 32° C and 100 µL of 0.24 mg/mL diatom frustule suspension in ethanol was dispersed onto the surface. Following evaporation, the diatom populated coverslips were placed in the UV-Ozone Cleaner again at 90° C for 24 hours to fix the diatoms to the substrate and oxidize any residual organic contaminants.

3.2.2 Diatom-Based NT-proBNP Sensor Fabrication

The sensor fabrication follows our earlier work with minor modifications[167]. Scanning electron microscopy (SEM) images of the coverslips are shown in Fig. 3.2a and b. The process of the sandwich type immunoassay is outlined in the schematic in Fig. 3.2c. Briefly, a 2.2 × 2.2 cm glass coverslip with diatom frustule mass coverage of 5 µg/cm^2 was first submerged in a mixture of 10 mL methanol, 500 µL of 99% acetic acid and 150 µL of 99% (3-Aminopropyl)-triethoxysilane (APTES) for 30 minutes at room temperature to populate the surface with free amine groups. The sample was rinsed with acetone and ethanol and dried with nitrogen. The sample was then submerged in 2% glutaraldehyde (GA), a homobifunctional crosslinker, in phosphate buffered saline (PBS) for 2 hours at

room temperature to react with the free amine group and to cover the surface with aldehyde groups. The substrate was rinsed with 20 mM 4-(2-hydroxyethyl)-1-piperazineethanesulfonic acid (HEPES) and deionized water to ensure complete removal of unbound aldehyde groups. Following the rinsing, the glass coverslip was dried with nitrogen gas flow and diced into multiple 5 × 5 mm sensors. Each sensor then had 1 µL of 0.1 mg/mL of the antibody, anti-proBNP, dropcast onto its surface. It was left at 4˚ C for 6 hours to allow the surface to be functionalized with the antibody. The sample was again rinsed with HEPES and water and dried with nitrogen gas. Next, the sample was submerged in 1 mg/mL bovine serum albumin (BSA) in PBS for 6 hours at 4˚ C to block all the remaining aldehyde groups. This decreases nonspecific binding and enhances the detection specificity of the immunoassay sensor. Again, the sample was rinsed with HEPES and water, and dried by nitrogen gas. At this point, the functionalized immunoassay sensor was ready for detection. The detection was performed by submerging the sample in a solution of NT-proBNP analyte in either PBS or human plasma. This step was performed in solution volumes of 900 mL and 400 µL for the buffer and plasma respectively. The sensor was kept in the solution for 2 hours at room temperature to allow for immune-recognition of the antibody-antigen pair. After another rinsing with HEPES and water, the sample had 1 µL of 0.25 mg/mL anti-NT-proBNP conjugated with fluorescein dropcast onto the surface, where it was left for 4 hours at 4˚ C, thus labeling the bound antigens with fluorophore labeled antibodies and completing the immune-sensing process.

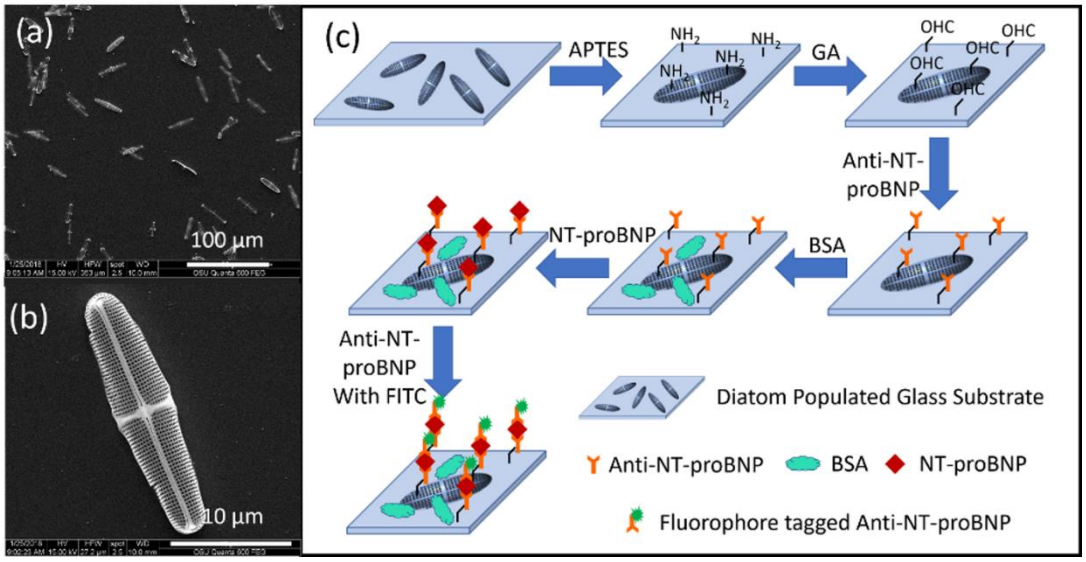

Fig. 3.2: SEM image of diatom frustule-populated glass slide (a) and zoomed in on a single frustule (b). Schematic view of diatom-based immunoassay for NT-proBNP detection (c).

3.2.3 Fluorescence Image Acquisition

Following the fabrication of the NT-proBNP sensor, the fluorescence images were measured using an Olympus IX 73 microscope paired with a bandpass filter and a 40× objective lens. Fluorescence excitation was achieved using a X-cite 120 LED fluorescence microscope light set at 250 mW. The images were collected using a Hamamatsu Digital Camera Orca Flash 4.0 LT using a 30 ms integration time for optical images and a 5 second integration time for fluorescence images.

3.2.4 Fluorescence Image Preprocessing

Using a process outlined in our previous work[167] with minor modifications, and shown Fig. 3.3 below, optical and fluorescence images were first superimposed on top of one another and aligned. Frustules in the image were then circled and a mask was created in the shape of the diatom shell. This mask was applied to the original fluorescence image,

leaving just the frustule with the remainder of the background zeroed out. Once the fluorescence image was masked, it was cropped to a uniform size with the frustule in the center. Another set of images were constructed from the original image with the frustules zeroed, leaving only the fluorescence information on glass. For diatom-glass fluorescence intensity comparisons, the resultant spatial domain fluorescence images, with diatoms cropped out, were used to highlight the fluorescence enhancement capabilities of diatoms.

After the diatom frustules from the fluorescence image were masked and cropped, the power spectral density (PSD) of each image was obtained by performing the two-dimensional fast Fourier transform (FFT) and taking the square of the absolute value in the spatial frequency domain. The image was shifted to move the zero-frequency component to the middle of the image and the natural log-scale was taken.

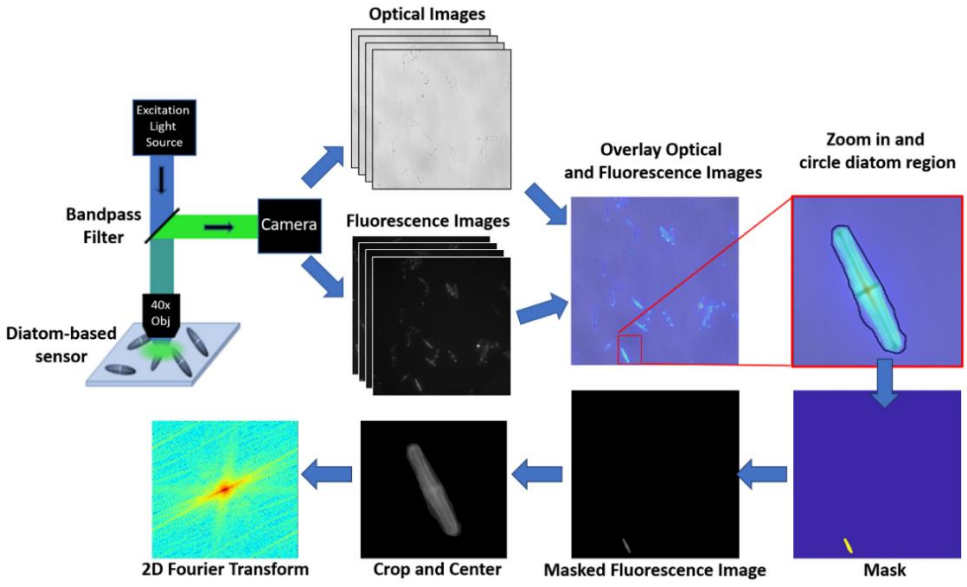

Fig. 3.3: Schematic view of preprocessing applied to the fluorescence images in preparation for analysis.

3.2.5 Statistical Regression Calibration Curve Creation

To create the calibration curve for solution-based NT-proBNP sensing, PCA was paired with PLSR. The model was created by first, using Matlab to find the average fluorescence intensity for each concentration by finding the average intensity of each PSD of the frequency domain image and taking the total average. Once the average intensity for each concentration was determined, 30 images with average intensities closest to the concentration's average fluorescence intensity were selected. This was done for each concentration to remove any outliers and resulted in a dataset of 30 images from each concentration. Using the built-in Matlab functions, the principle components (PCs) were determined and the first three were used in PLSR. A 5-fold cross-validation was performed using 80% of the data to train a regressionary model and which was tested on the remaining 20% to determine its quantification abilities

From the training and test regressions, the coefficient of determination (R^2) and the root mean square error (RMSE) were calculated from each cross-validation, and averaged. R^2 is defined as shown in Eq. 3.1 below.

$$R^2 = 1 - \frac{\sum_{i=1}^{n}(C_{Predicted,i} - C_{Actual,i})^2}{\sum_{i=1}^{n}(C_{Actual,i} - C_{avg})^2} \quad (3.1)$$

The variable $C_{Predicted}$ is the predicted concentration value from the model, C_{Actual} is the actual concentration of the measurement and C_{avg} is the average concentration of the measurements taken. The RMSE cross-validation (RMSECV) for the training data set and the RMSE predicted (RMSEP) for the test set were calculated as defined in Eq. 3.2 below where n is the number of measurements performed.

$$RMSE = \sqrt{\frac{\sum_{i=1}^{n}\left(C_{Predicted,i} - C_{Actual,i}\right)^2}{n}} \quad (3.2)$$

The RMSE is a measure of the average error predicted within the dataset and explains how spread out the data is and the R^2 is a measure of how good of a fit the regression gives. Generally, higher R^2 (but no more than 1) and lower RMSE values mean better regression performance. Discussion of our created model is given in section 3.3.2.

3.2.6 Qualitative Screening Procedure

To perform the qualitative screening of NT-proBNP in human plasma, the data preparation was similar to that of the regression analysis but 100 frequency domain images at high and low concentrations were chosen instead of 30, due to our larger plasma-based measurements dataset. PCA was performed on the images and classification algorithms, including kNN and SVM, were used in this analysis. kNN was achieved using Matlab's built-in function and SVM classification was performed using a common SVM library, libSVM[168]. The accuracy, sensitivity and specificity for each classification algorithm were calculated for various numbers of PCs using a 5-fold cross-validation and the average of each statistic were compared and discussed in section 3.3.3. Accuracy is a measure of how many measurements the model correctly classified and is defined by Eq. 3.3 below.

$$Accuracy = \frac{TP+TN}{TP+TN+FP+FN} \quad (3.3)$$

The model classifies the data sets into a positive and negative class which correspond to the high concentration and low concentration respectively. TP is the number of true positives, TN is the true negatives, FP is the false positives and FN is the number

of false negatives. Essentially, the accuracy is defined as the number of correctly classified measurements divided by the total number of measurements classified. Sensitivity is a measure of the number of correctly classified positive measurements with the definition below in Eq. 3.4.

$$Sensitivity = \frac{TP}{TP+FN} \tag{3.4}$$

The specificity is similar to the sensitivity but describes the number of correctly classified negative measurements. The definition is shown in Eq. 3.5. Each of these metrics range from 0 to 1 with 1 being perfect classification.

$$Specificity = \frac{TN}{TN+FP} \tag{3.5}$$

3.3 NT-proBNP Detection and Analysis

3.3.1 Average Intensity Analysis

To analyze the efficacy of our diatom-based fluorescence NT-proBNP biosensor, the immunoassay, image collection and preprocessing of the fluorescence images were performed as explained in sections 3.2.2-3.2.4 above, followed by an average intensity analysis. To begin, the average fluorescence intensity of each spatial domain image was calculated for a given concentration. The median average intensity was found, and images with an average fluorescence intensity greater than one standard deviation away from the median were excluded as outliers. The average and standard deviation of the remaining images' average fluorescence intensities were calculated for each concentration using the preprocessed spatial domain images of diatom frustules as well as the glass images. The

results were plotted versus the analyte concentration as shown in Fig. 3.4a. Figure 3.4b shows representative fluorescence images at those concentrations, which clearly highlights the enhanced fluorescence emission from the diatom biosilica due to the photonic crystal effect and surface effect. As can be seen in the figures, the fluorescence intensity on frustule is at least 2× higher than that on glass and validates the use of frustules for enhancing the fluorophore's signals.

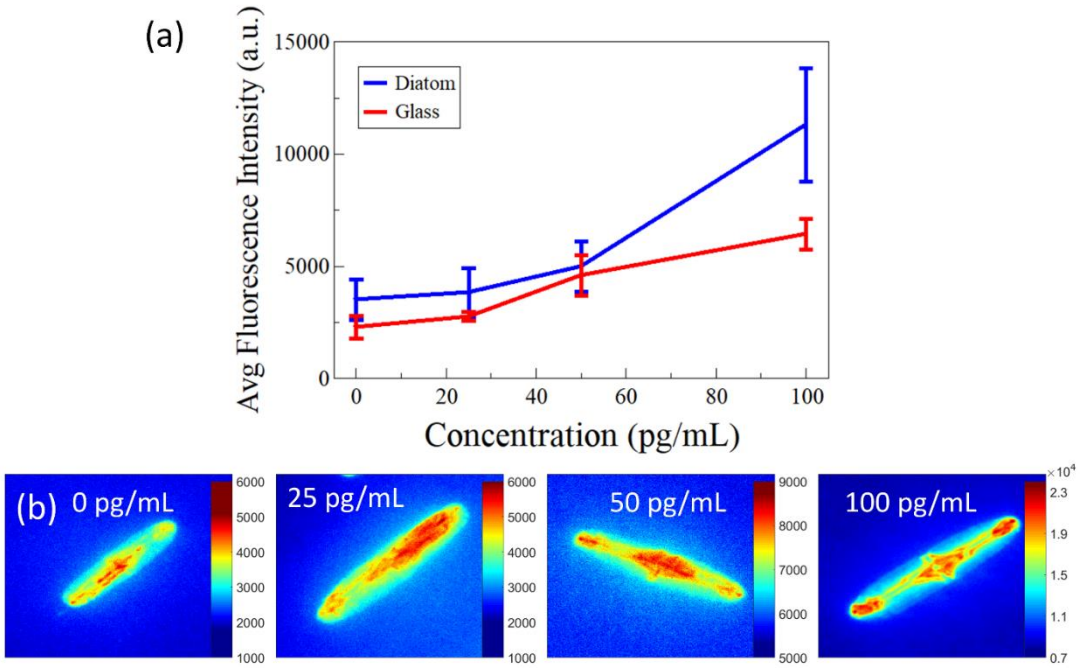

Fig. 3.4: A comparison plot of average fluorescence intensity on diatom biosilica and glass (a). Representative fluorescence images of the frustules (b).

Description of the fluorescence enhancing mechanism of frustules is explained in the previous chapter. Using this average fluorescence analysis, NT-proBNP at 100 pg/mL is distinct since the signal is clearly above the error bar of the control test (zero analyte concentration). However, for lower concentrations of analyte testing, the fluorescence signals are comparable to the error bar of the negative test, making it difficult to

differentiate. A more sophisticated method of analysis is required to achieve better sensitivity and quantization.

3.3.2 Quantitative Statistical Regression

While the average intensity analysis is simple and straightforward, the calibration curve is nonlinear with large variation, both with or without diatom frustules, resulting in a high limit of detection. Random errors during the immunoassay process and the statistical nature of fluorescence emission are the main causes of the error bars, which are intrinsic to the fluorescence imaging immunoassay. More advanced statistical analytical methods must be employed to improve the sensing performance.

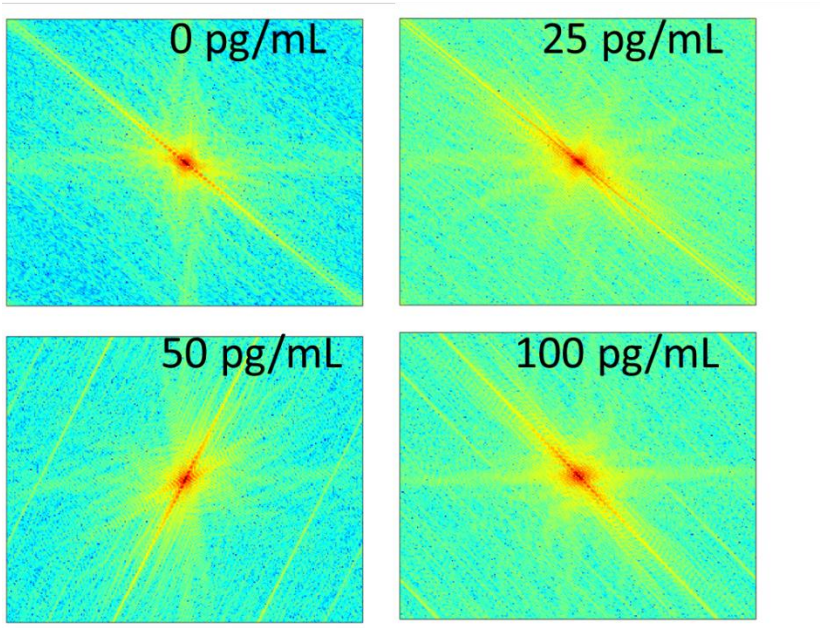

Fig. 3.5: Representative spatial frequency domain images of diatoms

Statistical regressions were performed using spatial domain images as well as the PSD of the spatial frequency domain images of preprocessed diatom images. Figure 3.5

shows representative spatial frequency domain images from the preprocessed diatom images. The central peak relates to the zero-frequency component of the background and the points in the image further from the center represent higher frequency components of the diatom fluorescence image. The spike lines radiating from the center represent fluorescence signals in the spatial domain corresponding to the geometric feature of diatom frustules. For example, the minor axis of the diatom in the spatial domain is represented by the prominent line radiating from the center of the spatial frequency domain image along the same axis.

The aim of the regression is to find the correlation of the fluorescence intensity and the analyte concentration. Optimal results were achieved by implementing PCA feature extraction with PLSR. Comparing the regression results applied to the spatial and spatial frequency domain images, spatial frequency domain images gave superior results. This may be due to the fact that the intensity variation among different concentrations in the spatial domain is slight, as seen in Fig. 3.4a. However, the spatial frequency domain is a more detailed image space and is heavily influenced by changes in the spatial domain. The slight change in fluorescence intensity in the spatial domain results in a much greater change in the spatial frequency domain. PCA and PLSR rely on variation to differentiate analyte concentrations and thus the greater change in the spatial frequency domain allows for greater sensitivity of PCA and PLSR.

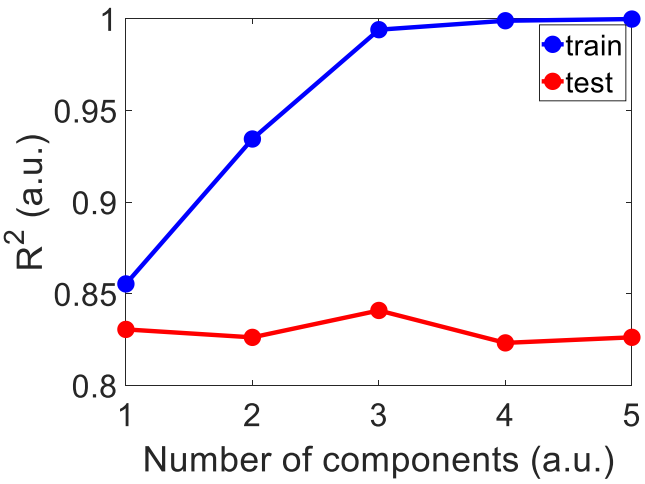

Fig. 3.6: Partial least squares regression R^2 values for training and test data plotted against the number of principle components used.

The number of PCs to include in the regression step affects the quality of the model achieved. The number of components to include was swept and R^2 values were compared and plotted in Fig. 3.6 above. From this plot, it is clear that after three PCs, the R^2 training value is saturated and close to 1. To reduce computation time without sacrificing accuracy, we elected to input three PCs to the PLSR algorithm.

Optimal results were achieved using the first three PCs and the training data PCs are plotted in Fig. 3.7a. The PLSR algorithm creates a model which can then be applied to a test set. As explained in section 3.2.5, a 5-fold cross-validation was performed by training a model using 80% of the images and testing that model on the remaining 20% images. This allows verification of the utility of our model for future quantification. The calculated calibration curve from the training set was applied to the test dataset. The calibration fit, as well as that obtained when validating the model, are shown in Fig. 3.7b below. Applying this model to the test dataset, we achieved good linearity with a R^2 testing value of 0.86

and a predicted RMSE (RMSEP) of 14.47. The high R^2 value and the low RMSEP indicate accurate quantifications of NT-proBNP detection.

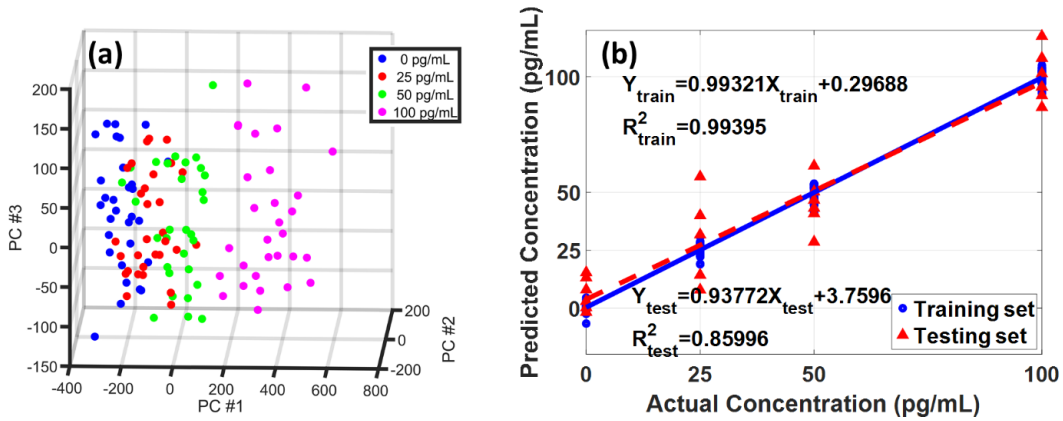

Fig. 3.7: The first three principle components of the images in the training dataset (a). Predictive model achieved using optimized statistical regression parameters on the training dataset, and the prediction results by applying the model to the testing dataset (b).

3.3.3 Qualitative Classification of NT-proBNP in Plasma

In real-world applications, the detection of NT-proBNP is performed in a real biological fluid with competing biomolecules like proteins that can obscure the signal. To prove the validity of our photonic crystal-enhanced fluorescence imaging immunoassay for future clinical usage, we performed the detection of NT-proBNP in human plasma. A qualitative classification screening was performed to screen for high or low concentrations of NT-proBNP. According to the literature[137, 138], if the NT-proBNP concentration is below 125 pg/mL, it can be used to “rule out” heart failure. If the concentration is above 450 pg/mL, it can be used to “rule in” heart failure. For this classification, we combined measurements made at 10 and 50 pg/mL to be considered a low concentration class and measurements made at 500 pg/mL was a high concentration class. To ensure the same

number of measurements were in each category, 50 images, with average intensities closest to the mean average intensity, were selected from each lower concentration. From the higher concentration, 100 measurements were taken, again, with average intensities closest to the total average intensity at this concentration. Representative spatial and spatial frequency domain images of frustules at high and low analyte concentration are shown in Fig. 3.8a-d below.

The classification analysis was performed using PCA feature extraction combined with two classification techniques which were compared to find the best solution. The kNN and SVM are classification techniques that have been applied to both fluorescence imaging and spectroscopy biosensing[162-164]. kNN is a non-parametric classification method. An unlabeled test sample is classified by a majority vote of its k-nearest neighbors and the most frequent label is assigned to the class of the output. SVM algorithm is a widely used supervised learning method which can efficiently perform a non-linear classification using the nonlinear kernel function and fitting the maximum-margin hyperplane in a transformed feature space.

The two classification algorithms were applied after PCA of the spatial frequency domain images and parameters were swept to find the optimal solution for each algorithm. A 5-fold cross-validation was again performed to enable training of the model and testing. The parameters for SVM were optimized and the results are shown in Fig. 3.8: (e) is the classification results from the training dataset and (f) is from the test dataset. Both are plotted with respect to the first three PCs. The color of each data point represents its actual

concentration class and each point with an “X” represents measurements that were incorrectly classified.

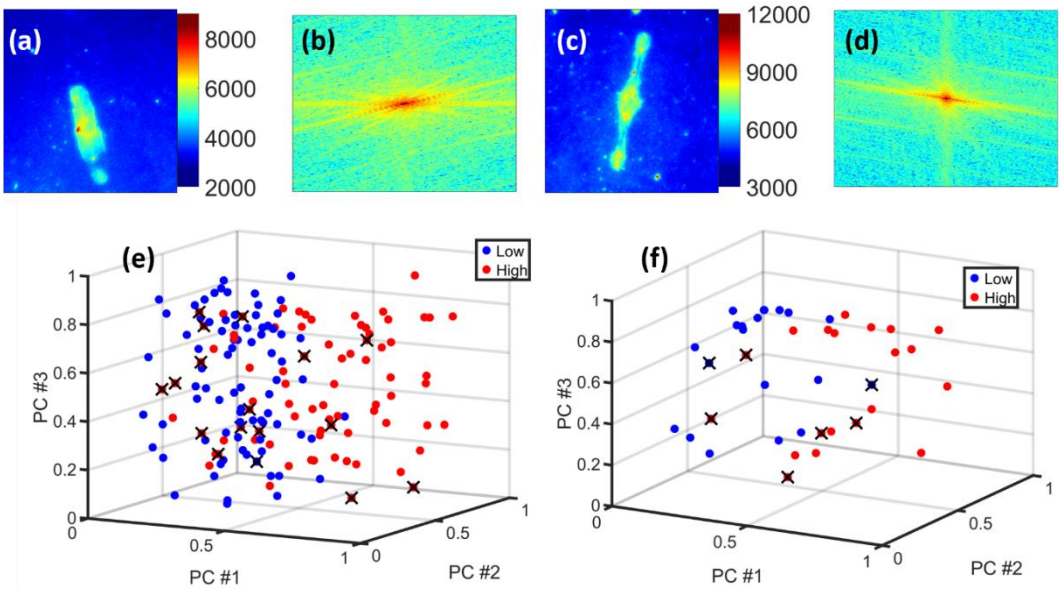

Fig. 3.8: Representative frustule images for low (a-b) and high (c-d) analyte concentrations in the spatial (a, c) and spatial frequency domains (b, d).Classification results of training (e) and test dataset (f) plotted with respect to the first three principle components extracted using PCA. The X’s represent measurements that were incorrectly classified.

From these classifications, the accuracy, sensitivity, and specificity were calculated as explained previously. These are common metrics that indicate the quality of the classification model where the closer to 1 (but less than 1), the better the classification model. The calculated metrics for the optimal solution for each classification technique were obtained from each of the 5-fold cross-validations and averaged. The two classification methods were compared, and the results are shown in Table 3.1 below. It was found that using SVM with enough PCs to account for 55% of the sample variation gave the best results.

Table 3.1: Binary classification results from NT-proBNP detection in plasma

	Training			Testing		
	Accuracy	Sensitivity	Specificity	Accuracy	Sensitivity	Specificity
SVM	0.929	0.860	0.998	0.775	0.640	0.910
kNN	0.668	0.368	0.968	0.540	0.290	0.800

As can be seen in the table above, the SVM model has a predictive accuracy and sensitivity that are slightly lower than desired. However, the specificity, of 91%, is excellent. The specificity is a measure of the model's ability to correctly classify negative measurements, in this case, the model can successfully determine low concentrations of NT-proBNP. As can be seen in Fig. 3.8 above, very few low concentration measurements were classified inaccurately. This allows us to confidently classify low concentration samples and rule out the heart failure diagnosis. The large discrepancy between the sensitivity and specificity can be attributed to the inclusion of two analyte concentrations in the lower concentration class compared to the single concentration included in the high class. The added variability provided by multiple concentrations allowed for a more robust model to be constructed thus allowing for better classification at low concentrations. In our future work, we will improve classification by including multiple analyte concentrations in both classes.

3.4 Summary

NT-proBNP is a clinically important cardiovascular disease biomarker. A photonic crystal-enhanced fluorescence imaging immunoassay biosensor has been created for this analyte, capable of detecting clinically relevant levels of NT-proBNP. Photonic diatom frustules achieve fluorescence signal intensity enhancement of fluorophores as high as 2× compared with those on the flat glass substrate. Furthermore, using PLSR, a predictive model has been extracted and validated on a test dataset showing excellent linearity with a R^2 of 0.86 and a RMSEP of 14.47. This model can be applied to an unknown measurement to quantify the analyte concentration far surpassing the clinical detection requirement, with an excellent measurement accuracy. To prove the potential for clinical testing, the biosensor was employed to screen NT-proBNP in human plasma and we were able to successfully implement SVM classification with an excellent test specificity of 91% to rule out heart failure with further optimization being done to improve its ability to rule in heart failure. In short, we have successfully shown that diatom frustules can be used as fluorescence imaging immunoassay platform to detect NT-proBNP. The statistical regressions and classifications we have developed can be used for the detection and classification of NT-proBNP levels. This easy-to-use and cost-effective immunoassay can achieve clinically relevant levels of detection while avoiding the complexity of current ECL method of detection.

Multi-scale Plasmonic-Photonic Crystal Nanomaterial for Rapid Vapor-Phase Detection of Explosives

Kenneth J. Squire, Sivashanmugan Kundan, Boxin Zhang, Joseph Kraai, Gregory Rorrer, and Alan X. Wang

Submission Pending

CHAPTER 4: MULTI-SCALE PLASMONIC-PHOTONIC CRYSTAL NANOMATERIAL FOR RAPID VAPOR-PHASE DETECTION OF EXPLOSIVES

In previous chapters, a diatom-based fluorescence immunoassay sensor was demonstrated and shown to be capable of enhancing detection. The practical screening of NT-proBNP was shown and cardiovascular disease can be successfully detected. To continue the exploration of further practical applications of the diatom-based sensor, a vapor-phase SERS sensor is fabricated to detect explosives and a representative figure is shown in Fig. 4.1 below. This is done to demonstrate the variability of diatom frustules to benefit the practical detection of multiple detection modalities in a variety of fields. Furthermore, the frustule enhancement for vapor sensing demonstrates the physical, as well as optical, enhancements diatoms contribute to a sensor.

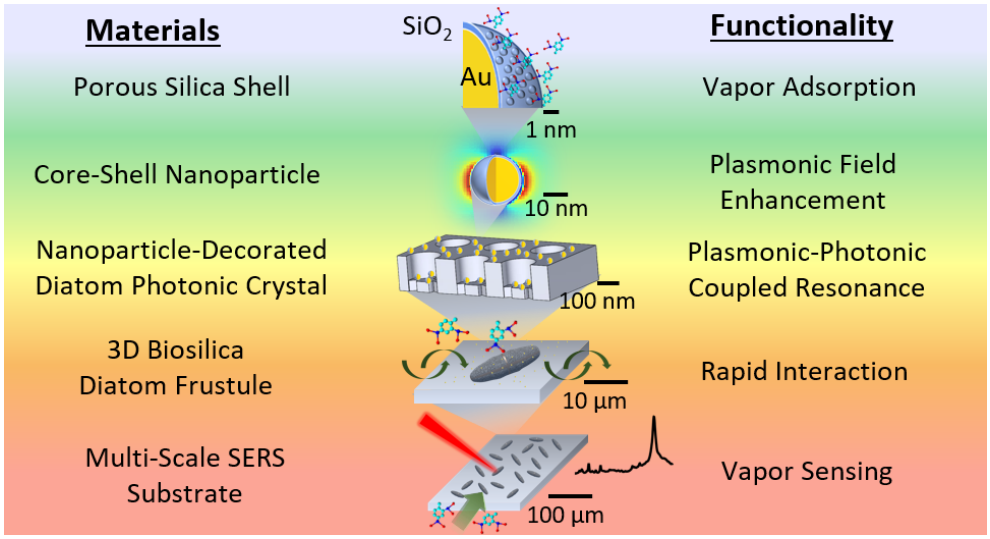

Fig. 4.1: Representative figure demonstrating the multi-scale enhancement of the hybrid SERS structure.

4.1 Background

Surface-enhanced Raman spectroscopy (SERS) is an appealing optical detection technique due to its capacity for rapid sensing, multiplex detection, and high sensitivity, capable of achieving single molecule detection[169]. Because of the many benefits of SERS sensing, its implementation to the detection of vapor analytes has been explored for several years[170-173], particularly for the detection of explosives[174]. However, improved response time and sensitivity are required for practical detections. The natural diffusion of the analyte vapor to a substrate is slow and hinders the response time of the sensor. For example, Chou et al. utilized a laser ablation fabricated gold nanostructured substrate to detect explosive 2,4-dinitrotoluene (DNT) vapor, but required 18 hours of analyte interaction[175]. To improve the response time, "flow-through"[176, 177] and "flow-over"[178] type sensors have been employed to reduce vapor diffusion time. Piorek and co-workers fabricated an open microfluidic channel, flowing plasmonic nanoparticles (NPs) to capture explosive DNT vapor across the open channel. However, this required a constant supply of flowing NPs and the complicated fluidic-vapor setup renders great difficulty in implementation[178]. Similarly, other applications requiring external circulation apparatuses also add complexity and difficulty to sensing setups.

Sensitive detection of trace levels of the explosive vapor enables remote and accurate sensing. High SERS sensitivity can be achieved through the rational design and fabrication of novel SERS substrates such as Demeritte's detection 100 fM 2,4,6-trinitrotoluene (TNT) in solution by using a single walled carbon nanotube functionalized with popcorn-shaped gold nanoparticles[179]. However, the plasmonic field enhancements accompanying the

SERS substrates are localized effects and, without analyte adsorption capabilities, are dependent upon vapor diffusion and condensation. Vapor adsorption allows for the capture and concentration of the target molecule within sensing regions and ensures the stability of the measurement. Improved vapor adsorption has been attained through substrate chemical functionalization[180, 181] and utilization of 3-dimensional (3D) materials[182, 183]. Wang et al. fabricated rationally designed nanocluster arrays, and Sylvia et al. prepared a roughened gold substrate for explosive vapor detection. Detection was achieved down to 10 parts-per-trillion (ppt) and 5 parts-per-billion (ppb), respectively. However, both required wetting the substrate with sodium hydroxide to increase the binding affinity and enable analyte adsorption, resulting in a sensing process that is more involved and tedious[180, 181]. Our group has previously achieved detection of attogram levels of TNT, but this was solution-based detection requiring inkjet printing for sample concentration[98]. A vapor sensor with strong analyte adsorption is needed to achieve rapid response and high sensitivity for practical engineering applications.

Multi-scale materials have extended the horizon of SERS sensing. Kreno et al. fabricated a porous metal-organic framework over a silver “film-on-nanoparticles” structure to increase surface area and analyte trapping while also enhancing SERS[171]. Chan fabricated biodegradable core-shell NPs for the delayed delivery of chemotherapy drugs, demonstrating molecular adsorption and desorption control[184]. Our group has previously fabricated a multi-scale mesoporous diatom capsules with plasmonic NPs to enable efficient substrate-environment interactions while simultaneously achieving plasmonic-enhanced optical fields[185]. The combination of multi-scale materials may

contribute multi-functionalities to enable rapid and sensitive vapor detection. Diatom frustules are one pragmatic component. As discussed in earlier chapters, diatoms are unicellular microalgae, found abundantly in nature, that possess a hierarchal nano-porous biosilica shell called a frustule. The periodic nano-pores within the structure of the frustule forms a naturally-occurring photonic crystal with properties similar to rationally-designed photonic crystals. Frustules have been integrated with optical biosensors and shown capable of enhancing optical signals[167, 186], particularly SERS[97, 99, 101, 187]. The photonic crystal structure of the frustule allows the induction of guided-mode resonance (GMR) within its structure, capable of pairing with the plasmonic resonance of metallic nanoparticles, resulting in stronger electromagnetic fields[91, 97]. Beyond optical enhancements, the implementation of mesoporous structures in flow-through applications have been shown to result in rapid equilibration due to the favorable transport of the analyte to the substrate[188, 189] and similarly, the hollow, mesoporous biosilica diatom frustule allows fast diffusion of gases[93]. The integration of frustules into a vapor sensor contributes enhanced optical field and increased analyte interaction for greater sensitivity and shorter response time.

Metallic nanoparticles are easily synthesized and common optical enhancers for SERS. However, the near-field plasmonic field enhancement decays exponentially with distance and analyte molecules not in the immediate vicinity of the NP are not detected[18]. The application of a shell, creating a core-shell NP structure, has been shown to contribute oxidative resistivity, thermal stability and stronger binding affinities for improved molecular trapping[190-193]. It has been verified by several works that silica shells on

NPs, fabricated by the Stöber method, result in a thin porous shell[194-197]. Furthermore, the silica shell can lead to facile immobilization of analytes that do not possess metal-binding functional groups[198]. This increased binding affinity and large surface area provides abundant binding sites and enables effective analyte trapping and concentration. The multi-scale plasmonic NP with a porous shell contributes optical signal enhancement and vapor adsorption capabilities.

The motivation for this work is to create a multi-scale SERS substrate capable of sensitive and rapid detection of analyte vapors, particularly explosives. An average of 19 injuries or deaths per day were reported in 2017 worldwide due to exploding landmines with 87% of those being civilians and 47% of the civilians being children[199]. TNT and its byproduct, DNT, are common components found in landmines. Though the percentage of DNT present is small compared to TNT, its vapor pressure is 20-100× greater, making it a preferred indicator for explosive device detection[200, 201]. Deteriorated casings of landmines release vaporized explosives into the soil and air, enabling detection. In this work, we present a multi-scale vapor SERS sensor, synergistically pairing gold-silica core-shell ($Au@SiO_2$) nanoparticles and photonic crystal-like frustules for the rapid and sensitive vapor SERS detection of DNT as shown in Fig. 4.2 below. The 36 nm plasmonic core and the porous, nanometer-thick shell enable enhanced electromagnetic fields, while trapping analyte molecules in these sensing regions. Meanwhile, the 30 μm frustule with 200 nm pores enables further field enhancement, as well as improved vapor-substrate interaction, enabling a rapid response. Using the polycyclic aromatic hydrocarbon, pyrene, as a model molecule, we characterize our multi-scale vapor SERS substrate. The

contributions from each component of the multi-scale sensor is explored and detection of pyrene vapor at 1 part-per-million (ppm) is achieved in only 3 minutes. DNT vapor is also detected at room temperature below 100 ppb in under 3 minutes, thus demonstrating the potential of our multi-scale sensor for target vapor sensing.

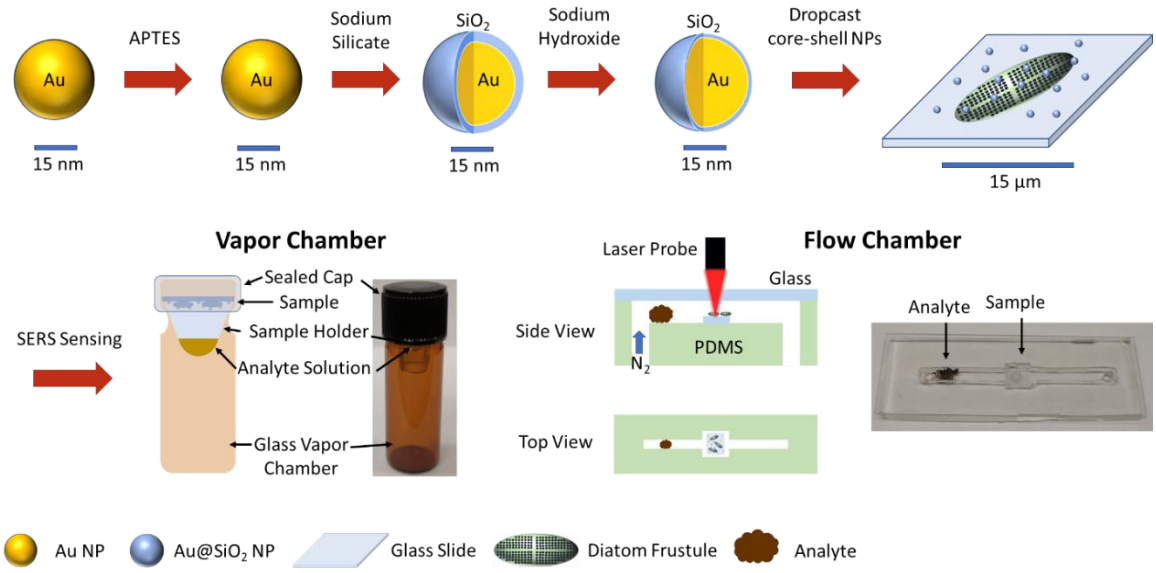

Fig. 4.2: Schematic showing synthesis process of Au@SiO2 core-shell NPs and subsequent integration on frustule-populated substrate to form multi-scale SERS vapor sensor and integration with stagnant vapor and vapor flow chambers.

4.2 Sensor Fabrication and Experimental Procedures

4.2.1 Synthesis of $Au@SiO_2$ Nanoparticles

The synthesis of the core-shell nanoparticles follows a procedure similar to the one found in the literature[190] with minor modifications and is shown in the schematic in Fig. 4.2 above. First, 70 mg of gold chloride was dissolved in 200 mL water and stirred at 130° C for 10 minutes. Next, 8.4 mL of 1% sodium citrate in H_2O (w/w) was slowly added and left stirring for 20 minutes at 230° C. During this process, the color changed from a pale

yellow to a deep purple, indicating the formation of gold NPs. The gold colloid was allowed to cool, and then NPs were separated into 50 mL aliquots and centrifuged at 7000 rotations per minute (RPM) for 15 minutes. The supernatant was removed, and the concentrated NPs were stored at 4° C for future use. One aliquot was resuspended in 50 mL of H_2O and the colloidal solution was used to coat with a silica shell. 100 µL of 1 mM APTES was added to the 20 mL colloidal Au NPs and stirred at room temperature for 20 minutes to silanate the surface. The pH of the solution was verified to be between 5-7 and adjusted if necessary. Sodium silicate solution was diluted in H_2O to 0.54% and 1 mL of this mixture was slowly pipetted into the mixing solution. This was left vigorously mixing for 20 hours to coat the NPs with a silica shell. 1 mL of 0.1 M NaOH in H_2O was slowly added and stirred gently for 4 hours to reduce the shell. The colloidal Au@SiO_2 NPs were centrifuged at 6000 RPM for 20 minutes and resuspended in 20 mL H_2O. The solution was centrifuged again using the same conditions after which it was decanted and left concentrated and stored at 4° C for future use. NP integration with diatom frustule-populated substrates was achieved by dicing the substrate into ~5×5 mm pieces. 1µL of Au@SiO_2 nanoparticle (NP) solution was dropcast onto the substrate and dried at 60°. This is represented in Fig. 4.2 and was repeated for a total of four drops.

4.2.2 Vapor Chamber Setup

A vapor chamber, shown in Fig. 4.2 above, was created using a glass vial, inset with a sample holder. 20 µL of an analyte-ethanol solution was pipetted into the sample holder and the multi-scale SERS substrate was placed facedown above the solution, high enough to ensure that no solution interacted with the substrate. The chamber was then sealed with

thermal tape and Parafilm Sealing Film. The chamber was heated on a hotplate to 70° C and left for various times. The SERS signal was immediately measured afterwards. For each substrate, 20 measurements were made and the 10 most similar were taken. The average and standard deviation of the characteristic peak intensity were calculated.

4.2.3 Flow Vapor Chamber

The flow chamber is shown in Fig. 4.2 above. A 3×60×2 mm (width x length x height) polydimethylsiloxane channel was constructed with a larger sample holding area (7 mm x 7 mm) in the middle. 10±5 mg of solid explosive DNT was placed near the inlet and about 2 cm away from the sensor. Once the sample and multi-scale sensor were placed in the channel, it was sealed with a glass slide. Nitrogen gas flowed through the channel with a regulator pressure of 1 pound per square inch (PSI). The Raman excitation source was focused through the glass slide and onto the sensor within the channel and measurements were taken immediately and continuously with 50 mW power and 60 second integration. Before each use, the channel was rinsed with EtOH and H_2O followed by drying with nitrogen gas to ensure its freedom from contaminants.

4.3 Vapor Sensing Results and Discussions

4.3.1 Au@SiO_2 NP Characterization

Utilizing FEI Quanta 600F scanning electron microscopy (SEM) and a FEI Titan transmission electron microscopy (TEM), the Au@SiO_2 NPs were characterized. Using ImageJ on 174 particles, it was found that the diameter of the NPs was 36±5 nm with a representative SEM and the size distribution being shown in the Fig. 4.3a and b. Strong optical absorption was measured, indicating the plasmonic effect of the NPs, which was plotted in Fig. 4.3c.

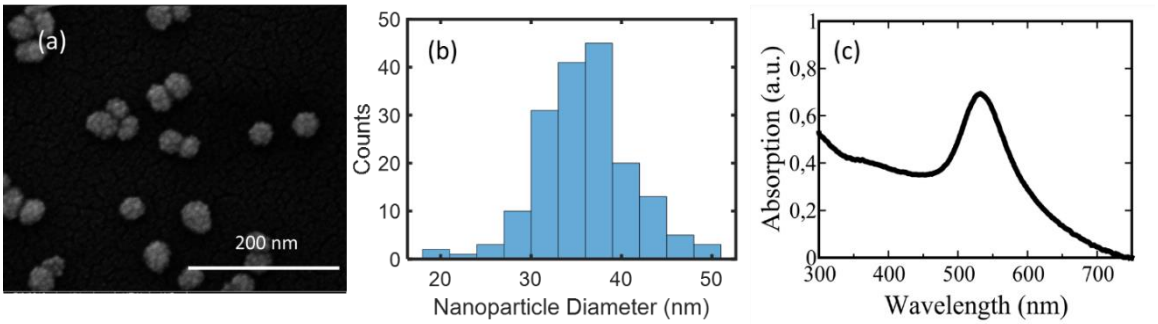

Fig. 4.3: Representative SEM image of core-shell NPs (a). Plots showing NP size distribution (b) and the absorption spectrum of core-shell NPs (c).

The diatom frustules were prepared as described in previous chapters. The diatom frustules are about 30 µm along the major axis and 10 µm along the minor axis with prime pores and sub-pores of 200 and 70 nm diameter, respectively. The large surface area-to-volume ratio of the biosilica frustule and the abundant silanol groups on its surface endow the frustule with abundant binding sites allowing for efficient NP decoration. The combination of the core-shell NPs with the micron-sized frustules was achieved using a

simple drop-casting method. The resulting macroscopic multi-scale hybrid structure is shown in Fig. 4.4a and the microscopic diatom frustule, showing core-shell NPs within the frustule pores, is shown in Fig. 4.4b and c. Frustules, as has been shown in our previous work, contribute optical field enhancements from GMR which combine with the plasmonic resonance of the nanoparticles. This enhancement is greatest when the plasmonic NPs are within the pores of the frustule[97, 101]. The TEM image in Fig. 4.4d verifies the existence of NPs within the pores, ensuring the effective combination of the biosilica diatom frustule and the plasmonic core-shell NPs. The core-shell NP structure is shown in Fig. 4.4e. The metallic core, responsible for the plasmonic enhancement can be seen, as well as the porous shell around it.

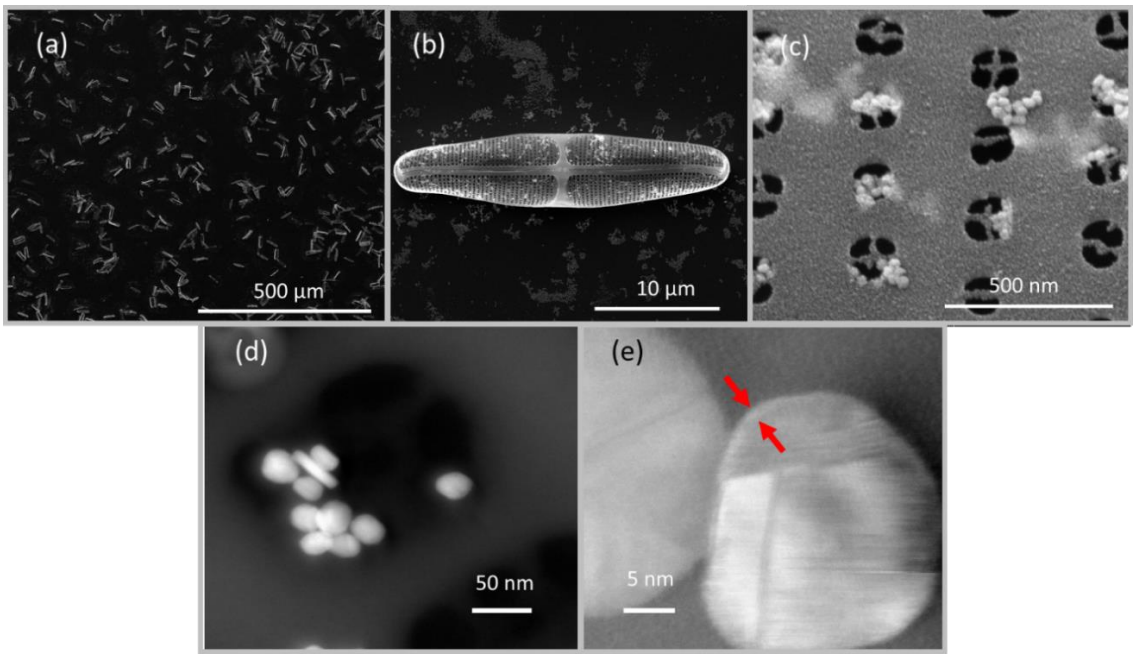

Fig. 4.4: SEM images of the combined multi-scale SERS substrate with core-shell and frustule structure shown at different magnifications (a-c). TEM images of NPs in a frustule pore (d) and core-shell structure with arrows highlighting the shell (e).

Using the TEM image, the shell is confirmed to have a thickness of ~1 nm, which follows the literature[190]. The nanoparticle composition was further investigated using energy-dispersive X-ray spectroscopy and is shown in Fig. 4.5. These images verify the formation of the core-shell NPs, their population upon the diatom frustules and in the frustule pores, and finally the total fabrication of our multi-scale hybrid SERS substrate.

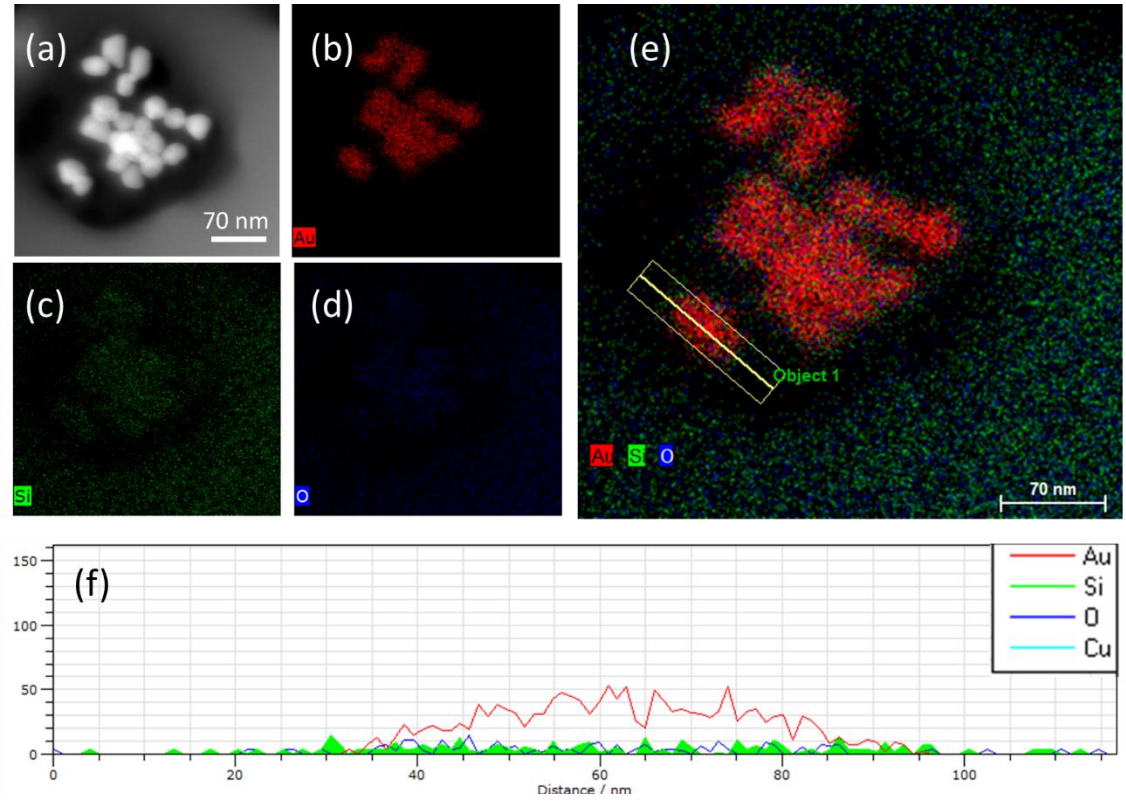

Fig. 4.5: TEM image of Au@SiO_2 NPs in frustule pore is shown (a). EDS was performed and the components are split into Au (b), Si (c) and O (d) as well as all three combined (e). A cross-sectional line map was created, and the composition is shown in (f) clearly showing the spatial separation of the Au core and the Si shell.

4.3.2 Core-Shell NPs for Vapor SERS

The SERS capabilities of our sensor were characterized by drop-casting various concentrations of pyrene-EtOH solution onto the core-shell-frustule substrate and

measuring the signal with the results shown in Fig. 4.6. Using the core-shell NPs, solution-based detection of pyrene down to 100 ppb was achieved, showing that the core-shell structure is capable of SERS.

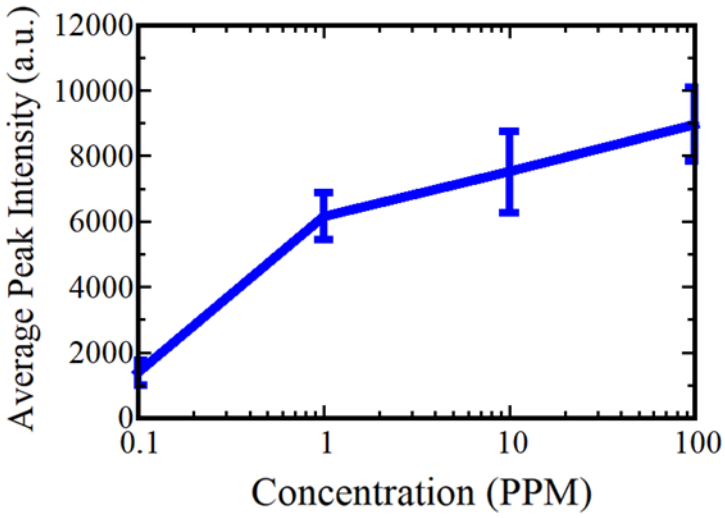

Fig. 4.6: SERS of pyrene dropcast on frustule-Au@SiO_2 substrates to show potential of core-shell NPs for SERS measurement.

Having verified the solution-based SERS capabilities of the core-shell NPs, vapor SERS is investigated. To thoroughly investigate and attribute the contribution from core-shell NPs, we prepared glass substrates with and without diatom frustules and drop-cast 1) Au@SiO_2 NPs 2) Au NPs or 3) no NPs onto their surfaces. The substrates were then placed face down in the stagnant vapor chamber shown in Fig. 4.2 above with 20 µL of 100 ppm pyrene-ethanol solution as described in the methods section. The substrates were heated for 5 minutes and SERS was measured. Representative spectra for each substrate are shown in Fig. 4.7 below. The characteristic peak at 587 cm^{-1} is attributed to the CCH out-of-plane deformation and is used in our analysis. The average and standard deviation of the

characteristic peak intensity is calculated from ten spectra and displayed for each substrate in Fig. 4.7b.

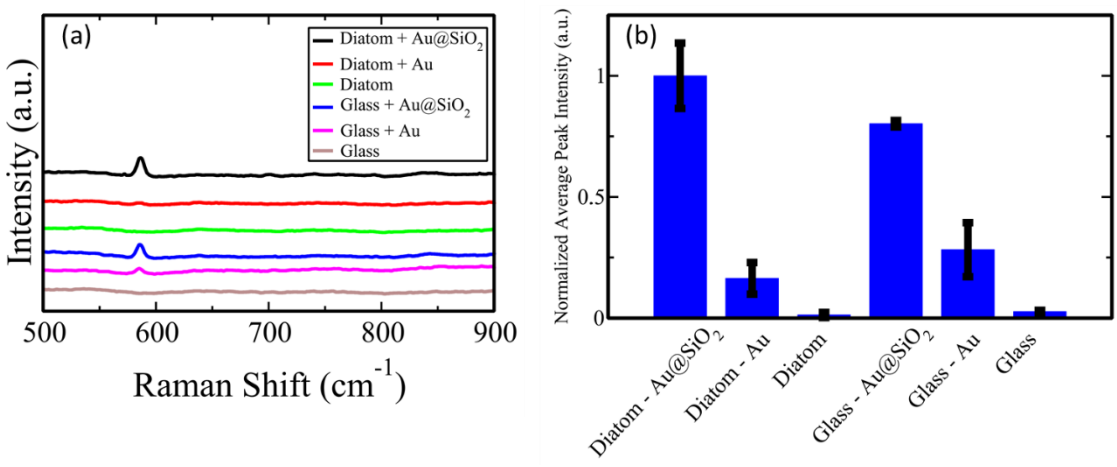

Fig. 4.7: Representative pyrene spectra (100 ppm) on frustule and glass substrates with $Au@SiO_2$ NPs, Au NPs, or no NPs (a) and bar graph showing normalized average characteristic peak intensities for each substrate (b).

When comparing substrates with no NPs, Au NPs, or $Au@SiO_2$ NPs, the peak intensity is significantly greater when the core-shell structure is employed. This observed SERS improvement can be attributed to the physical enhancement of vapor adsorption and concentration in the shell of the NP. Because the enhanced field effect from the plasmon resonance decays exponentially with distance from the particle, it is desirable to have the analytes as close to the metallic core as possible[18]. The addition of the silica shell and the subsequent hydroxylation of the surface siloxane sites results in the formation of silanol groups (Si-OH) which enables efficient hydrogen bonding between the core-shell NP and the analyte[202]. The improved binding affinity and resulting entrapment of the analyte within the porous shell serves to both concentrate and localize the analyte within close

proximity to the plasmon, thus enabling greater interaction with the enhanced field and resulting in the improved sensing.

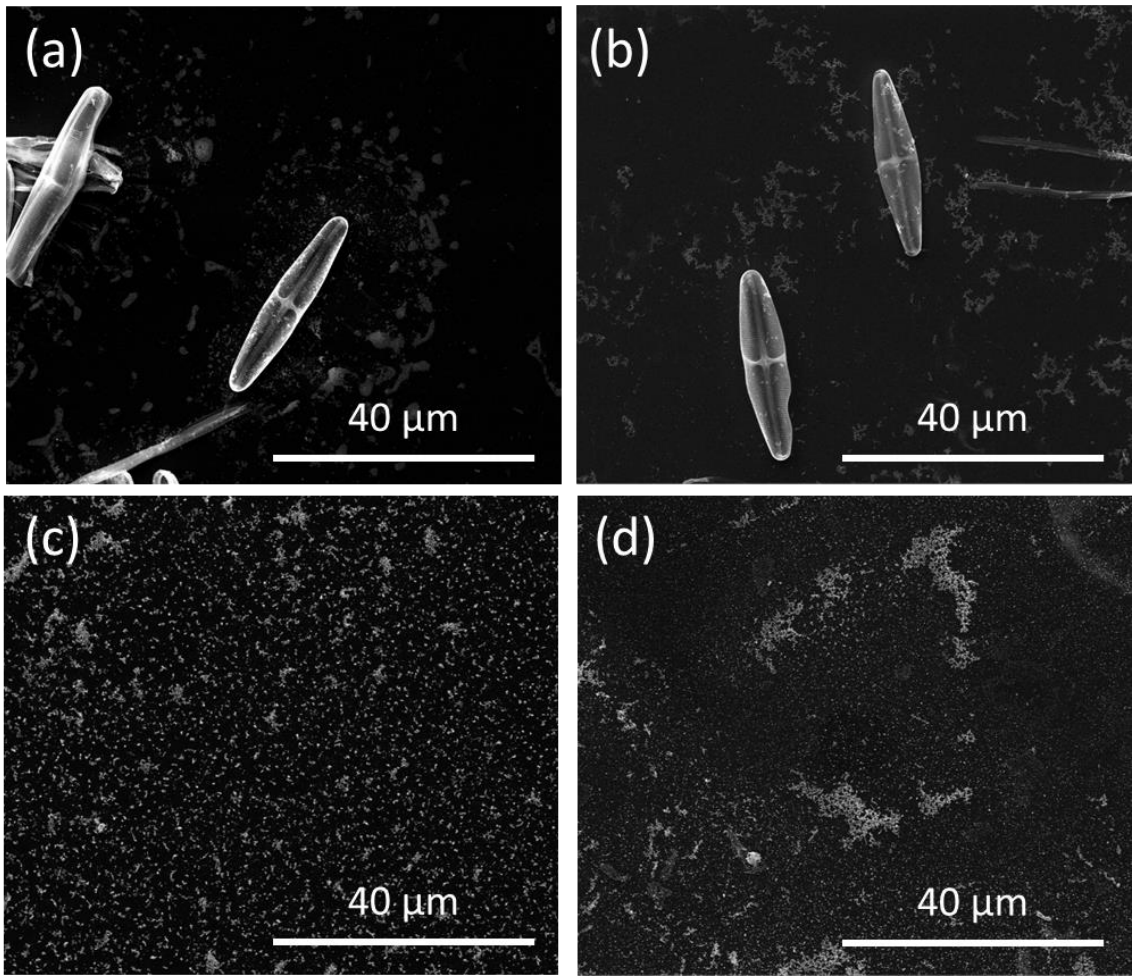

Fig. 4.8: SEM images of diatom frustule (a,b) and glass (c,d) substrates with core-shell NPs (a,c) and Au NPs (b,d) with a horizontal field width of 85 µm corresponding to the size of the laser spot. This clearly shows the higher density of NPs on glass despite which, the SERS intensity on diatom is superior.

Comparing the peak intensity on the frustule-populated substrate and that without frustules, we see a relatively small enhancement. This can be attributed to the NP density upon each the substrate. Due to the hydrophilic nature of the frustules, the drop-casted NPs spread further and cover a larger area on diatom substrates than on the glass substrate,

resulting in a lower density of NPs, as shown in Fig. 4.8 above. This will be remedied in future iterations by optimizing parameters such as NP concentration or number of drop-cast repetitions. However, despite the lower NP density, the intensity on the frustule-populated substrate is still greater than that on glass.

4.3.3 3-Dimensional Biosilica Diatom Frustule Analysis

After validating the utility of the core-shell NPs, the enhancements from diatom frustules were analyzed. To verify the accuracy of our measurement, the time-dependent analyte desorption was measured. Au@SiO_2-populated substrates with and without diatoms were placed in the vapor chamber for 12 hours at 70° C with 20 µL 100 ppm pyrene in EtOH. SERS measurements were taken immediately following the substrates' removal from the chamber and again at each of the intervals denoted on the plots below (Fig. 4.9a and b). 20 measurements were taken, and the peak intensities were calculated. The 10 spectra with peak intensities closest to the mean were averaged and the standard deviation was calculated and plotted with respect to time. At room temperature, even after two hours, the adsorbed molecules remain affixed within our sensor, resulting in little to no change in the SERS intensity. Thus, any desorption of analytes between the sensor's removal from the chamber, and its immediate measurement afterwards, is negligible, demonstrating a strong binding affinity between the analyte and the SERS substrate. When 70° C heat is applied, the desorption of the molecules occurs much more quickly and may be used for future sensor reuse.

To investigate the reduction of response time due to the presence of diatom frustules, the time-dependent adsorption of frustule and glass substrates was measured. Substrates

with $Au@SiO_2$ NPs were placed in the vapor chamber and heated for various times at 70° C with 20 µL pyrene in EtOH. The 20 SERS spectra were measured upon removal from the vapor chamber and 10 were selected to calculate the average and standard deviation of the characteristic peak at 587 cm^{-1}. The average peak intensity, normalized to the saturation intensity for each substrate, was plotted in Fig 4.9c below. As can be seen from the plots below, the diatom-based sensor has a much faster response time, reaching equilibrium within 3 minutes, whereas the substrate without diatoms has almost no signal at 3 minutes and took 20 minutes to equilibrate. This 6-fold reduction in response time can be attributed to the mesoporous structure of the diatom frustule. The porous 3D frustule allows the analyte vapor to rapidly permeate the structure and have greater interaction with the core-shell NPs compared to those decorating the planar glass surface. This results in rapid analyte adsorption into the porous shell of the NPs and thus, faster detection and saturation times. This effect has been utilized previously with the implementation of mesoporous structures in flow-through sensing applications resulting in rapid equilibration due to the favorable transport of the analyte to the substrate[188, 189]. Similarly, the hollow, mesoporous biosilica diatom frustule has demonstrated fast diffusion of gases[93]. The utilization of the 3D porous frustule in our application enables efficient vapor-substrate interaction and, consequentially, rapid adsorption and concentration within the porous NP shell.

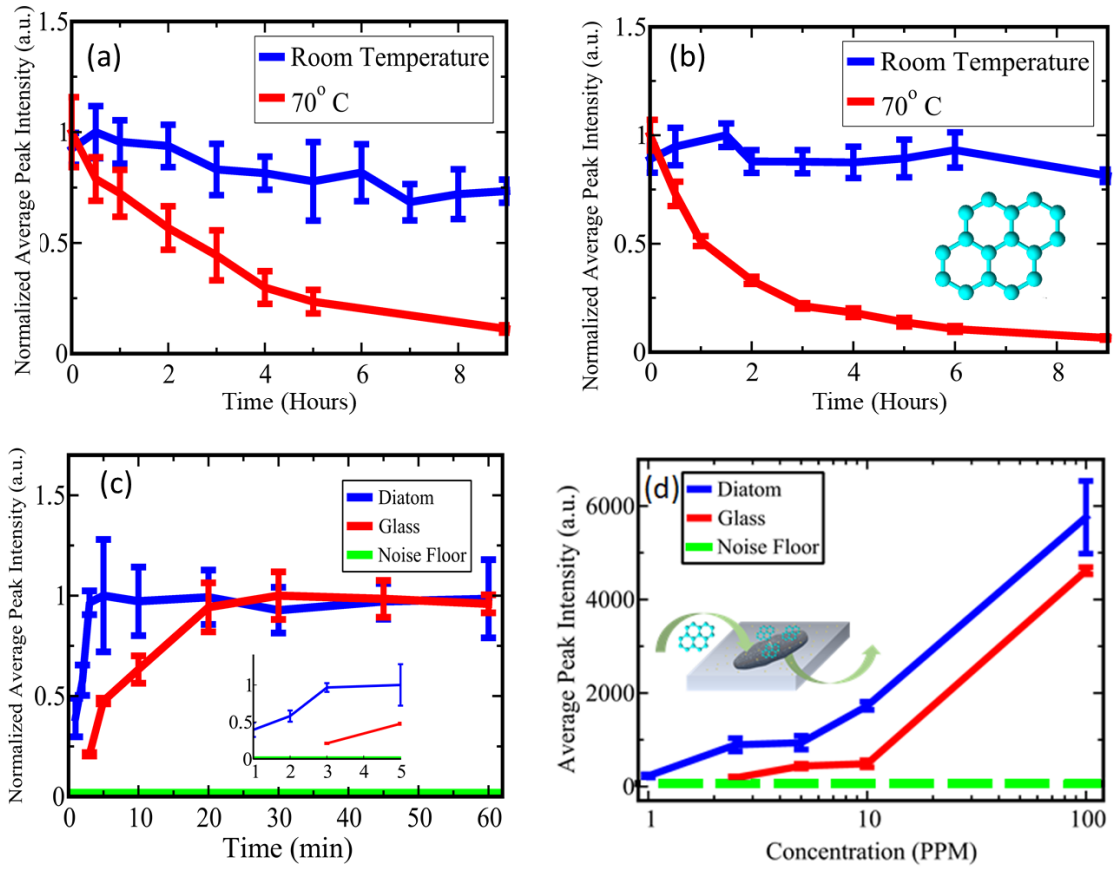

Fig. 4.9: Time-dependent desorption on substrates with (a) and without (b) diatom frustules at room temperature and at 70° C. A molecular pyrene inset is also shown in (b). The normalized average peak intensity is displayed with respect to time with a zoomed inset (c). Average peak intensity with respect to analyte concentration is plotted to show the concentration dependence with a diatom-vapor interaction schematic inset (d).

The dependence of the SERS peak intensity to the analyte concentration was compared between the frustule-populated substrate and the regular glass substrate. Using the same vapor chamber setup and various concentrations of pyrene in EtOH heated for 5 minutes, the results shown in Fig. 4.9d were obtained. The noise floor was defined to be the average characteristic peak intensity of the control substrate (no pyrene present) plus three times its standard deviation. As can be seen from the plot, detection without diatom was achieved

down to 2.5 ppm whereas concentrations down to 1 ppm were obtained with frustules. It has been shown that guided resonant modes can be excited within the photonic crystal-like structure of the diatom frustule and result in enhanced SERS sensitivity[97, 187]. The guided resonant mode interacts with the plasmonic resonance from the core-shell NPs to achieve a plasmonic-photonic enhancement capable of inducing fields over 20 times greater than those from metal nanoparticles on planar glass[91]. Additionally, as seen in Fig. 4.9d, the enhancement factor from diatom increases with a decrease in analyte concentration. This is evidence of the further enhancement from the 3D frustule structure. At high concentrations, with an abundance of analytes, natural diffusion is sufficient for effective analyte interaction with the core-shell NPs. However, at lower concentrations, the 3D structure is needed to allow efficient interaction of analyte molecules with the NPs. This accounts for the difference between the small enhancement from diatom seen in Fig. 4.7b at high analyte concentration, and the large diatom enhancement seen at lower concentrations in Fig. 4.9d. The reproducibility of the sensor was also verified by performing an experiment in triplicate. Three diatom-populated substrates with three drops of Au@SiO_2 NPs were placed in vapor chambers with 20 µL of 1000 ppm pyrene in EtOH. Each sample was left heating at 70° for 45 minutes and then immediately removed and measured. Similar to the other measurements, 20 spectra were measured, the characteristic peak intensity was calculated and the 10 spectra with intensities closest to the mean were used. The average characteristic peak intensity was then calculated, as well as the standard deviation. The three normalized peak intensities for the samples were plotted below in Fig.

4.10 with the standard deviation. The average characteristic peak intensities are within 10% between the three samples, demonstrating high reproducibility.

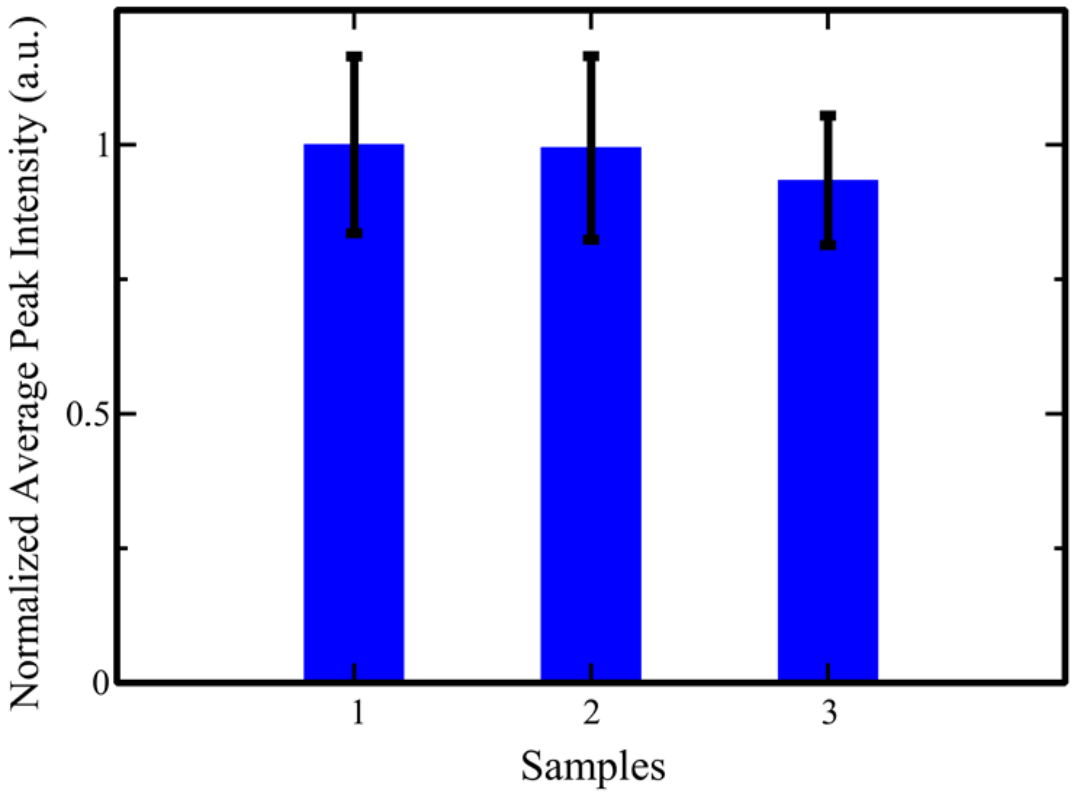

Fig. 4.10: Normalized average peak intensity of three samples performed under the same circumstances to demonstrate the reproducibility of the substrates.

4.3.4 Application of Multi-Scale SERS Substrate for DNT detection

Utilizing the multi-scale SERS substrate, DNT was detected in the vapor chamber shown in Fig. 4.2 above and described in the experimental section. The substrate was placed facedown above 20 mg of solid DNT and the chamber was heated for 30 minutes. Fig. 4.11a shows the 1000 ppm solution-based DNT SERS spectrum, as well as the background-subtracted, vapor SERS spectrum. The main characteristic peaks at 830 and

1332 cm^{-1} correspond to the out-of-plane NO_2 bending mode and the NO_2 stretching mode respectively. The background subtraction in the vapor SERS measurement resulted in a slight baseline decrease at higher wavenumbers but both characteristic peaks are clearly detectable, demonstrating the ability to sense DNT in the stationary vapor chamber.

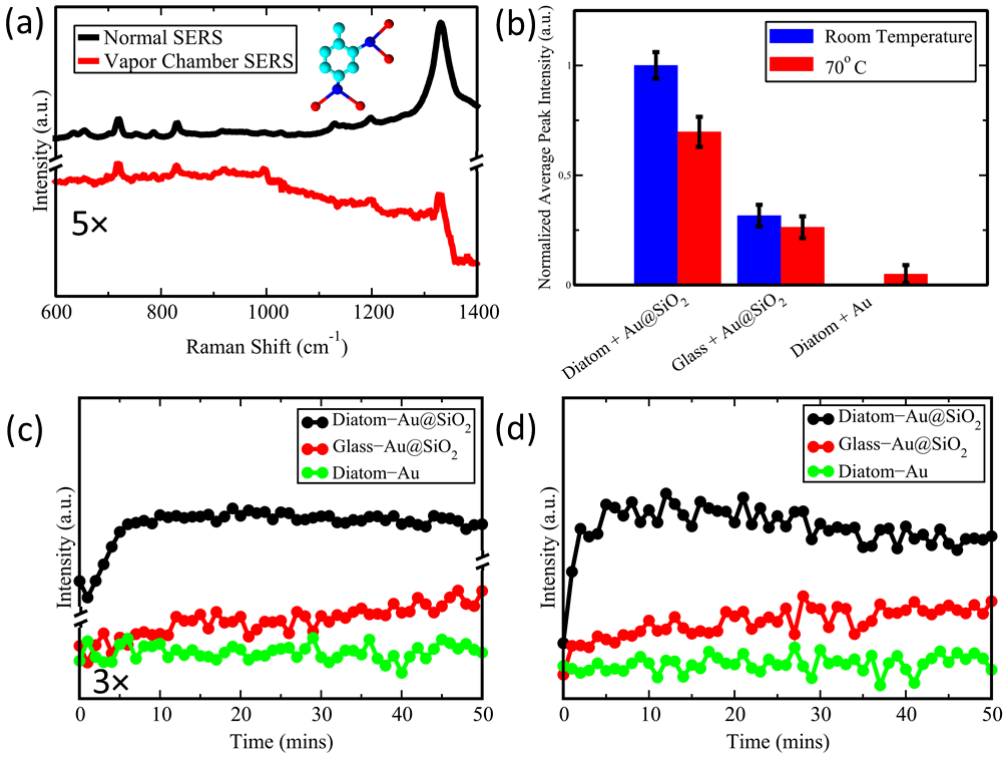

Fig. 4.11: Regular and vapor chamber SERS spectra are shown with the molecular structure of DNT inset (a). Average characteristic peak intensity on diatom-Au@SiO_2, glass-Au@SiO_2, and diatom-Au substrates in DNT flow chamber at room temperature and at 70° C are shown (b). The time dependence is also shown at room temperature (c) and at 70° C (d). Different scales are used to highlight trends and peaks (a,c).

The detection of DNT in a sealed container where a saturated headspace can form was performed to verify the detection capabilities however, it is desirable to create a sensor capable of detecting buried landmines in their environment, without the need for the formation of a concentrated headspace. The practical detection of DNT is achieved

utilizing a flow chamber as shown in Fig. 4.2 above and described in the experimental section. The concentration of DNT in this setup is less than the saturation vapor (100 ppb) and simulates real detection conditions where an equilibrated headspace may not have formed, due to ambient air flow. For this detection, 10±0.5 mg DNT was placed 2 cm away from the substrate and nitrogen flowed through the chamber, over the DNT and the multi-scale SERS substrate. SERS signals were measured continuously. Using this setup, we tested diatom-Au@SiO_2 NP, diatom-Au NP, and glass-Au@SiO_2 NP substrates. This was done at room temperature as well as under heating conditions at 70° C. The normalized average peak intensity of the 1332 cm^{-1} peak for each of these, along with their standard deviation, are shown in Fig 4.11b. As can be seen, the intensity on the substrate with diatom frustules and core-shell NPs at room temperature yields the best results, while the diatom-Au NP substrate shows almost no signal and the glass-Au@SiO_2 NP substrate shows a very slow response. This agrees with our previous pyrene characterization and highlights the importance of the core-shell and 3D frustule structures. Comparing temperature, one may expect the signal to be stronger under heated circumstances as that allows for more DNT to vaporize. While true, the heating condition also allows for trapped analytes within the core-shell structure to dissociate more quickly, as shown by our time-dependent desorption analysis in Fig. 4.9a and b. The stronger SERS intensity at room temperature is advantageous, as detection can be achieved without the need of external heating.

In addition to investigating the average peak intensity, the time-dependent intensity was measured at room temperature and 70° C (Fig. 4.11c and d). From these plots, it is clear that the diatom-core-shell hybrid substrate yields the best results with the highest

intensity and fastest response time. The diatom-Au NP substrate shows almost no signal. The glass-Au@SiO_2 NP substrate shows clear signal however, even after 50 minutes the substrate still hasn't reached equilibrium sensitivity. On the other hand, the multi-scale diatom-Au@SiO_2 NP substrate has a strong signal, capable of detecting the vapor within 3 minutes and reaching equilibrated response within only 5 minutes, allowing for fast and sensitive measurements. The performance of the diatom-Au NP, and glass-Au@SiO_2 NP substrates are similar under heated conditions as those at room temperature. However, the diatom-core-shell NP substrate shows a faster response time of 1 minute and saturates within 3 minutes, but with a slightly lower intensity due to the dissociation of the trapped analyte. The collaborative contributions from photonic crystal-like diatom frustules and core-shell Au@SiO_2 NPs coalesce in this detection of DNT. The multi-scale nature of our sensor enables rapid response while enhancing the analyte signal compared to other substrates. This clearly highlights both the ability of our sensor for vapor-based explosives sensing and its potential for further applications.

4.4 Summary

In this work we have demonstrated a multi-scale SERS substrate by synergistically combining naturally occurring photonic crystal-like diatom frustules and Au NPs with a mesoporous silica shell and used this substrate for the detection of explosive vapor. Utilizing a custom vapor chamber and the model analyte pyrene, the contributions from each component of the multi-scale substrate was verified. The nanometer-thick porous silica shell traps and concentrates the analyte vapor while the 36 nm plasmonic core enhances the Raman signal. The periodic array of 70 nm-wide sub-pores and 200 nm-wide

prime pores of the 30 μm-long diatom frustule enables GMR that couples with the plasmonic resonance of the NP for more sensitive SERS. The largely hollow and porous structure of the frustule allows for greater circulation and improved vapor-substrate interactions. These functionalities were employed using a flow chamber and detection of DNT vapor from the solid explosive below 100 ppb was demonstrated within 3 minutes at room temperature with the sensor reaching equilibrium in only 5 minutes. The sensitive and rapid detection results achieved by this multi-scale SERS substrate clearly illustrates its capabilities for vapor-phase explosives detection and its potential for future landmine and other vapor-phase SERS detections.

CHAPTER 5: CONCLUSION

Fluorescence and SERS are powerful detection techniques that are capable of achieving sensitive, selective, and responsive detection. However, current methods of substrate fabrication are generally expensive, time consuming, or irreproducible. Furthermore, with increased interest in point-of-care sensing, consumer grade electronics will need to be implemented. To achieve practical and comparable levels of detection with components inferior to their laboratory-based counterparts, signal enhancing substrates are necessary.

Diatom frustules, naturally occurring photonic crystal-like structures, are abundant in nature and easily obtained. Furthermore, the multi-scale nature of the three-dimensional biosilica shell enables optical, physical, and chemical enhancements for various sensing modalities. By harnessing the enhancements from these ubiquitous, natural structures, optical signals can be enhanced, and sensing substrates can be made while adding little to no expense.

In this work, diatom frustules for the enhancement of fluorescence and SERS sensing has been presented. In Chapter 2, diatom frustules are paired with a sandwich immunoassay to selectively capture an analyte followed by selective tagging of that bound analyte with a fluorescent label. It was shown theoretically that the frustule structure is capable of enhancing the fluorescence through the Purcell effect and through its large surface area-to-volume ratio. Experimentally it was proven that the fluorescence spectroscopy limit of detection measured upon the frustules was 100× higher than similar

measurements made without the frustule. Fluorescence imaging achieved 10× enhancement to the limit of detection utilizing the hot-spot counting approach.

Diatom frustule-based immunoassays were then shown to be practical methods of detection in Chapter 3. Using a sandwich immunoassay process similar to that described in Chapter 2, detection of the cardiovascular disease biomarker NT-proBNP was achieved. Fluorescence images were taken and analyzed, comparing the fluorescence on diatom and on glass. The images were analyzed in the spatial domain as well as the spatial frequency domain. Employing statistical chemometric analytics, the principle components of the images were extracted and used to create a regressionary calibration curve to be used for quantifying unknown amounts of NT-proBNP. A R^2 value of 0.86 and a predictive root mean square error of 14.47 was achieved. Lastly, a practical screening of high and low concentrations of NT-proBNP in plasma with 91% specificity was successfully demonstrated showing the diatom frustules' ability to be used for practical, real-world applications.

To demonstrate the versatility and potential of diatom-based optical sensors, the frustules were applied to SERS sensing of explosive vapors. The multi-scaled structure was fabricated by pairing hierarchal porous diatom frustules with core-shell nanoparticles. To characterize the vapor-phase detection capabilities of the sensor, pyrene gas was employed. It was found that the porous nature of the nanoparticle shell enabled adsorption and concentration of analyte molecules while its metallic core provided the plasmonic enhancement necessary for the SERS measurement. The diatom frustule enabled enhanced SERS signal and the porous nature of the structure enabled better analyte-substrate

interactions for rapid sensing. The substrate was applied to the vapor detection of the explosive 2,4-dinitrotoluene (DNT). Using a chamber with flowing gas to simulate practical detection conditions, detection of the DNT vapor was achieved in as little as 3 minutes with equilibrium sensitivity being reached within only 5 minutes. The rapid response and enhanced SERS signal of the frustule-based sensor demonstrates significant promise for further vapor-phase sensing.

In summary, the body of work represented in this dissertation represents an excellent method to enhance optical methods of detection. Their ubiquitous nature makes diatoms an easy and inexpensive method of boosting optical sensing capabilities. The addition of chemometric analytical methods allows for further enhancement and applications. Diatom frustule-enhanced optical sensing has vast potential, as shown by its implementation in fields as diverse as the fluorescence detection of biomarkers and the vapor-phase SERS detection of explosives. Further utilization and implementation of frustules in optical detection will result in an array of sensors in a variety of fields that are inexpensive and sensitive with rapid response.

REFERENCES

1. D. Llères, S. Swift and A.I. Lamond, Detecting Protein-Protein Interactions In Vivo with FRET using Multiphoton Fluorescence Lifetime Imaging Microscopy (FLIM), Current Protocols in Cytometry, 42 (2007) 12.10.11-12.10.19.
2. S. Shanmugaraju, S.A. Joshi and P.S. Mukherjee, Fluorescence and visual sensing of nitroaromatic explosives using electron rich discrete fluorophores, Journal of Materials Chemistry, 21 (2011) 9130-9138.
3. Y.H. Lee, H. Liu, J.Y. Lee, S.H. Kim, S.K. Kim, J.L. Sessler, Y. Kim and J.S. Kim, Dipyrenylcalix[4]arene—A Fluorescence-Based Chemosensor for Trinitroaromatic Explosives, Chemistry – A European Journal, 16 (2010) 5895-5901.
4. L.C. Shriver-Lake, C.H. Patterson and S.K. van Bergen, New horizons: Explosive detection in soil extracts with a fiber-optic biosensor, Field Analytical Chemistry & Technology, 4 (2000) 239-245.
5. A. Aït-Kaddour, T. Boubellouta and I. Chevallier, Development of a portable spectrofluorimeter for measuring the microbial spoilage of minced beef, Meat Science, 88 (2011) 675-681.
6. N. Oto, S. Oshita, Y. Makino, Y. Kawagoe, J. Sugiyama and M. Yoshimura, Non-destructive evaluation of ATP content and plate count on pork meat surface by fluorescence spectroscopy, Meat Science, 93 (2013) 579-585.
7. L. Brancaleon, A.J. Durkin, J.H. Tu, G. Menaker, J.D. Fallon and N. Kollias, In vivo Fluorescence Spectroscopy of Nonmelanoma Skin Cancer, Photochemistry and Photobiology, 73 (2001) 178-183.
8. Z.I. Volynskaya, A.S. Haka, K.L. Bechtel, M.F. M.D., R. Shenk, N. Wang, J. Nazemi, R.R. Dasari and M.S. Feld, Diagnosing breast cancer using diffuse reflectance spectroscopy and intrinsic fluorescence spectroscopy, Journal of Biomedical Optics, 13 (2008) 1-9, 9.
9. S.K. Chang, Y.N. Mirabal, E.N. Atkinson, D.D. Cox, A.M. M.D., M. Follen and R.R. Richards-Kortum, Combined reflectance and fluorescence spectroscopy for in vivo detection of cervical pre-cancer, Journal of Biomedical Optics, 10 (2005) 1-11, 11.
10. B.A. Flusberg, A. Nimmerjahn, E.D. Cocker, E.A. Mukamel, R.P.J. Barretto, T.H. Ko, L.D. Burns, J.C. Jung and M.J. Schnitzer, High-speed, miniaturized fluorescence microscopy in freely moving mice, Nature Methods, 5 (2008) 935.
11. K.K. Ghosh, L.D. Burns, E.D. Cocker, A. Nimmerjahn, Y. Ziv, A.E. Gamal and M.J. Schnitzer, Miniaturized integration of a fluorescence microscope, Nature Methods, 8 (2011) 871.
12. M.Y. Rennie, L. Lindvere-Teene, K. Tapang and R. Linden, Point-of-care fluorescence imaging predicts the presence of pathogenic bacteria in wounds: a clinical study, Journal of Wound Care, 26 (2017) 452-460.

13. D. Shin, M.C. Pierce, A.M. Gillenwater, M.D. Williams and R.R. Richards-Kortum, A Fiber-Optic Fluorescence Microscope Using a Consumer-Grade Digital Camera for In Vivo Cellular Imaging, PLOS ONE, 5 (2010) e11218.

14. H. Zhu, S. Mavandadi, A.F. Coskun, O. Yaglidere and A. Ozcan, Optofluidic Fluorescent Imaging Cytometry on a Cell Phone, Analytical Chemistry, 83 (2011) 6641-6647.

15. H. Zhu, O. Yaglidere, T.-W. Su, D. Tseng and A. Ozcan, Cost-effective and compact wide-field fluorescent imaging on a cell-phone, Lab on a Chip, 11 (2011) 315-322.

16. D.N. Breslauer, R.N. Maamari, N.A. Switz, W.A. Lam and D.A. Fletcher, Mobile Phone Based Clinical Microscopy for Global Health Applications, PLOS ONE, 4 (2009) e6320.

17. P. Anger, P. Bharadwaj and L. Novotny, Enhancement and Quenching of Single-Molecule Fluorescence, Physical Review Letters, 96 (2006) 113002.

18. P. Bharadwaj, P. Anger and L. Novotny, Nanoplasmonic enhancement of single-molecule fluorescence, Nanotechnology, 18 (2006) 044017.

19. G.P. Acuna, F.M. Möller, P. Holzmeister, S. Beater, B. Lalkens and P. Tinnefeld, Fluorescence Enhancement at Docking Sites of DNA-Directed Self-Assembled Nanoantennas, Science, 338 (2012) 506-510.

20. K. Aslan, M. Wu, J.R. Lakowicz and C.D. Geddes, Fluorescent Core−Shell Ag@SiO2 Nanocomposites for Metal-Enhanced Fluorescence and Single Nanoparticle Sensing Platforms, Journal of the American Chemical Society, 129 (2007) 1524-1525.

21. X.-Y. Xu and B. Yan, Eu(iii)-functionalized ZnO@MOF heterostructures: integration of pre-concentration and efficient charge transfer for the fabrication of a ppb-level sensing platform for volatile aldehyde gases in vehicles, Journal of Materials Chemistry A, 5 (2017) 2215-2223.

22. M.M. Wanderley, C. Wang, C.-D. Wu and W. Lin, A Chiral Porous Metal–Organic Framework for Highly Sensitive and Enantioselective Fluorescence Sensing of Amino Alcohols, Journal of the American Chemical Society, 134 (2012) 9050-9053.

23. A.N. Berlina, N.A. Taranova, A.V. Zherdev, Y.Y. Vengerov and B.B. Dzantiev, Quantum dot-based lateral flow immunoassay for detection of chloramphenicol in milk, Analytical and Bioanalytical Chemistry, 405 (2013) 4997-5000.

24. Y. Chen, et al., Near-infrared fluorescence-based multiplex lateral flow immunoassay for the simultaneous detection of four antibiotic residue families in milk, Biosensors and Bioelectronics, 79 (2016) 430-434.

25. J.M. Reyes-Goddard, H. Barr and N. Stone, Surface enhanced Raman scattering of herpes simplex virus in tear film, Photodiagnosis and Photodynamic Therapy, 5 (2008) 42-49.

26. Lesson 1. Basics of Raman scattering, https://www.nanophoton.net/raman-spectroscopy/lessons/lesson-1, (accessed 12/16/2019).

27. K. Squire, X. Kong, P. Leduff, G.L. Rorrer, S. Tang, B. Chen, C.P. McKay, R. Navarro-Gonzalez and A.X. Wang, Rochester, New York, 2016.

28. M. Muniz-Miranda, C. Gellini, P.R. Salvi and M. Pagliai, Surface-enhanced Raman micro-spectroscopy of DNA/RNA bases adsorbed on pyroxene rocks as a test of in situ search for life traces on Mars, Journal of Raman Spectroscopy, 41 (2010) 12-15.

29. S. Caporali, V. Moggi-Cecchi, M. Muniz-Miranda, M. Pagliai, G. Pratesi and V. Schettino, SERS investigation of possible extraterrestrial life traces: Experimental adsorption of adenine on a Martian meteorite, Meteoritics & Planetary Science, 47 (2012) 853-860.

30. F. Inscore, C. Shende, A. Sengupta, H. Huang and S. Farquharson, Detection of Drugs of Abuse in Saliva by Surface-Enhanced Raman Spectroscopy (SERS), Applied Spectroscopy, 65 (2011) 1004-1008.

31. K.R. Ackermann, T. Henkel and J. Popp, Quantitative Online Detection of Low-Concentrated Drugs via a SERS Microfluidic System, ChemPhysChem, 8 (2007) 2665-2670.

32. K. Faulds, W.E. Smith, D. Graham and R.J. Lacey, Assessment of silver and gold substrates for the detection of amphetamine sulfate by surface enhanced Raman scattering (SERS), Analyst, 127 (2002) 282-286.

33. T. Vo-Dinh, H.-N. Wang and J. Scaffidi, Plasmonic nanoprobes for SERS biosensing and bioimaging, Journal of Biophotonics, 3 (2010) 89-102.

34. K.C. Bantz, A.F. Meyer, N.J. Wittenberg, H. Im, Ö. Kurtuluş, S.H. Lee, N.C. Lindquist, S.-H. Oh and C.L. Haynes, Recent progress in SERS biosensing, Physical Chemistry Chemical Physics, 13 (2011) 11551-11567.

35. R.A. Tripp, R.A. Dluhy and Y. Zhao, Novel nanostructures for SERS biosensing, Nano Today, 3 (2008) 31-37.

36. R.S. Golightly, W.E. Doering and M.J. Natan, Surface-Enhanced Raman Spectroscopy and Homeland Security: A Perfect Match?, ACS Nano, 3 (2009) 2859-2869.

37. E.L. Izake, Forensic and homeland security applications of modern portable Raman spectroscopy, Forensic Science International, 202 (2010) 1-8.

38. Y. Cui, I.Y. Phang, Y.H. Lee, M.R. Lee, Q. Zhang and X.Y. Ling, Multiplex plasmonic anti-counterfeiting security labels based on surface-enhanced Raman scattering, Chemical Communications, 51 (2015) 5363-5366.

39. B. Sharma, R.R. Frontiera, A.-I. Henry, E. Ringe and R.P. Van Duyne, SERS: Materials, applications, and the future, Materials Today, 15 (2012) 16-25.

40. K. Chen, M. Leona, K.-C. Vo-Dinh, F. Yan, M.B. Wabuyele and T. Vo-Dinh, Application of surface-enhanced Raman scattering (SERS) for the identification of anthraquinone dyes used in works of art, Journal of Raman Spectroscopy, 37 (2006) 520-527.

41. S.A. Centeno and J. Shamir, Surface enhanced Raman scattering (SERS) and FTIR characterization of the sepia melanin pigment used in works of art, Journal of Molecular Structure, 873 (2008) 149-159.

42. A. Tittl, X. Yin, H. Giessen, X.-D. Tian, Z.-Q. Tian, C. Kremers, D.N. Chigrin and N. Liu, Plasmonic Smart Dust for Probing Local Chemical Reactions, Nano Letters, 13 (2013) 1816-1821.

43. J.F. Li, et al., Shell-isolated nanoparticle-enhanced Raman spectroscopy, Nature, 464 (2010) 392.

44. C. Pohling, J.L. Campbell, T.A. Larson, D. Van de Sompel, J. Levi, M.H. Bachmann, S.E. Bohndiek, J.V. Jokerst and S.S. Gambhir, Smart-Dust-Nanorice for Enhancement of Endogenous Raman Signal, Contrast in Photoacoustic Imaging, and T2-Shortening in Magnetic Resonance Imaging, Small, 14 (2018) 1703683.

45. E.M. van Schrojenstein Lantman, T. Deckert-Gaudig, A.J.G. Mank, V. Deckert and B.M. Weckhuysen, Catalytic processes monitored at the nanoscale with tip-enhanced Raman spectroscopy, Nature Nanotechnology, 7 (2012) 583.

46. B. Pettinger, B. Ren, G. Picardi, R. Schuster and G. Ertl, Nanoscale Probing of Adsorbed Species by Tip-Enhanced Raman Spectroscopy, Physical Review Letters, 92 (2004) 096101.

47. R.M. Stöckle, Y.D. Suh, V. Deckert and R. Zenobi, Nanoscale chemical analysis by tip-enhanced Raman spectroscopy, Chemical Physics Letters, 318 (2000) 131-136.

48. J. Xu, L. Zhang, H. Gong, J.í. Homola and Q. Yu, Tailoring Plasmonic Nanostructures for Optimal SERS Sensing of Small Molecules and Large Microorganisms, Small, 7 (2011) 371-376.

49. C. Cheng, B. Yan, S.M. Wong, X. Li, W. Zhou, T. Yu, Z. Shen, H. Yu and H.J. Fan, Fabrication and SERS Performance of Silver-Nanoparticle-Decorated Si/ZnO Nanotrees in Ordered Arrays, ACS Applied Materials & Interfaces, 2 (2010) 1824-1828.

50. Q. Zhang, Y.H. Lee, I.Y. Phang, C.K. Lee and X.Y. Ling, Hierarchical 3D SERS Substrates Fabricated by Integrating Photolithographic Microstructures and Self-Assembly of Silver Nanoparticles, Small, 10 (2014) 2703-2711.

51. M. Fan, G.F.S. Andrade and A.G. Brolo, A review on the fabrication of substrates for surface enhanced Raman spectroscopy and their applications in analytical chemistry, Analytica Chimica Acta, 693 (2011) 7-25.

52. Y. Fan, L. Liu, D. Sun, H. Lan, H. Fu, T. Yang, Y. She and C. Ni, “Turn-off” fluorescent data array sensor based on double quantum dots coupled with chemometrics for highly sensitive and selective detection of multicomponent pesticides, Analytica Chimica Acta, 916 (2016) 84-91.

53. D. Boehl, D. Solle, B. Hitzmann and T. Scheper, Chemometric modelling with two-dimensional fluorescence data for Claviceps purpurea bioprocess characterization, Journal of Biotechnology, 105 (2003) 179-188.

54. F. Clementschitsch, K. Jürgen, P. Florentina and B. Karl, Sensor combination and chemometric modelling for improved process monitoring in recombinant E. coli fed-batch cultivations, Journal of Biotechnology, 120 (2005) 183-196.

55. R. Botta, et al., Tuberculosis determination using SERS and chemometric methods, Tuberculosis, 108 (2018) 195-200.

56. J.E.L. Villa, M.A.S. Afonso, D.P. dos Santos, P.A. Mercadal, E.A. Coronado and R.J. Poppi, Colloidal gold clusters formation and chemometrics for direct SERS determination of bioanalytes in complex media, Spectrochimica Acta Part A: Molecular and Biomolecular Spectroscopy, 224 (2020) 117380.

57. N.E. Dina, A.M.R. Gherman, V. Chiş, C. Sârbu, A. Wieser, D. Bauer and C. Haisch, Characterization of Clinically Relevant Fungi via SERS Fingerprinting Assisted by Novel Chemometric Models, Analytical Chemistry, 90 (2018) 2484-2492.

58. J.D. Joannopoulos, P.R. Villeneuve and S. Fan, Photonic crystals, Solid State Communications, 102 (1997) 165-173.

59. J. Vučković, M. Lončar, H. Mabuchi and A. Scherer, Design of photonic crystal microcavities for cavity QED, Physical Review E, 65 (2001) 016608.

60. M. Lee and P.M. Fauchet, Two-dimensional silicon photonic crystal based biosensing platform for protein detection, Optics Express, 15 (2007) 4530-4535.

61. O. Painter, J. Vučković and A. Scherer, Defect modes of a two-dimensional photonic crystal in an optically thin dielectric slab, Journal of the Optical Society of America B, 16 (1999) 275-285.

62. A. Mekis, J.C. Chen, I. Kurland, S. Fan, P.R. Villeneuve and J.D. Joannopoulos, High Transmission through Sharp Bends in Photonic Crystal Waveguides, Physical review letters, 77 (1996) 3787-3790.

63. E. Kuramochi, M. Notomi, S. Mitsugi, A. Shinya, T. Tanabe and T. Watanabe, Ultrahigh-Q photonic crystal nanocavities realized by the local width modulation of a line defect, Applied Physics Letters, 88 (2006) 041112.

64. M. Notomi, K. Yamada, A. Shinya, J. Takahashi, C. Takahashi and I. Yokohama, Extremely Large Group-Velocity Dispersion of Line-Defect Waveguides in Photonic Crystal Slabs, Physical Review Letters, 87 (2001) 253902.

65. X. Zhang, Image resolution depending on slab thickness and object distance in a two-dimensional photonic-crystal-based superlens, Physical Review B, 70 (2004) 195110.

66. P.V. Parimi, W.T. Lu, P. Vodo and S. Sridhar, Imaging by flat lens using negative refraction, Nature, 426 (2003) 404-404.

67. T. Decoopman, G. Tayeb, S. Enoch, D. Maystre and B. Gralak, Photonic Crystal Lens: From Negative Refraction and Negative Index to Negative Permittivity and Permeability, Physical Review Letters, 97 (2006) 073905.

68. X. Zhang, Absolute negative refraction and imaging of unpolarized electromagnetic waves by two-dimensional photonic crystals, Physical Review B, 70 (2004) 205102.

69. E.M. Purcell, Spontaneous emission probabilities at radio frequencies, American Physical Society 69 (1946) 681.

70. N. Ganesh, W. Zhang, P.C. Mathias, E. Chow, J.A.N.T. Soares, V. Malyarchuk, A.D. Smith and B.T. Cunningham, Enhanced fluorescence emission from quantum dots on a photonic crystal surface, Nature Nanotechnology, 2 (2007) 515.

71. I.D. Block, P.C. Mathias, N. Ganesh, S.I. Jones, B.R. Dorvel, V. Chaudhery, L.O. Vodkin, R. Bashir and B.T. Cunningham, A detection instrument for enhanced-fluorescence and label-free imaging on photonic crystal surfaces, Optics Express, 17 (2009) 13222-13235.

72. C.-S. Huang, S. George, M. Lu, V. Chaudhery, R. Tan, R.C. Zangar and B.T. Cunningham, Application of Photonic Crystal Enhanced Fluorescence to Cancer Biomarker Microarrays, Analytical Chemistry, 83 (2011) 1425-1430.

73. H. Li, J. Wang, Z. Pan, L. Cui, L. Xu, R. Wang, Y. Song and L. Jiang, Amplifying fluorescence sensing based on inverse opal photonic crystal toward trace TNT detection, Journal of Materials Chemistry, 21 (2011) 1730-1735.

74. Y. Huang, F. Li, M. Qin, L. Jiang and Y. Song, A Multi-stopband Photonic-Crystal Microchip for High-Performance Metal-Ion Recognition Based on Fluorescent Detection, Angewandte Chemie International Edition, 52 (2013) 7296-7299.

75. S.-m. Kim, W. Zhang and B.T. Cunningham, Coupling discrete metal nanoparticles to photonic crystal surface resonant modes and application to Raman spectroscopy, Optics Express, 18 (2010) 4300-4309.

76. D. Christie, J. Lombardi and I. Kretzschmar, Two-Dimensional Array of Silica Particles as a SERS Substrate, The Journal of Physical Chemistry C, 118 (2014) 9114-9118.

77. J. Li, S. Dong, J. Tong, P. Zhu, G. Diao and Z. Yang, 3D ordered silver nanoshells silica photonic crystal beads for multiplex encoded SERS bioassay, Chemical Communications, 52 (2016) 284-287.

78. D. U. S, C.Y. Fu, K.S. Soh, B. Ramaswamy, A. Kumar and M. Olivo, Highly sensitive SERS detection of cancer proteins in low sample volume using hollow core photonic crystal fiber, Biosensors and Bioelectronics, 33 (2012) 293-298.

79. F. Eftekhari, A. Lee, E. Kumacheva and A.S. Helmy, Examining metal nanoparticle surface chemistry using hollow-core, photonic-crystal, fiber-assisted SERS, Optics Letters, 37 (2012) 680-682.

80. X. Zhao, J. Xue, Z. Mu, Y. Huang, M. Lu and Z. Gu, Gold nanoparticle incorporated inverse opal photonic crystal capillaries for optofluidic surface enhanced Raman spectroscopy, Biosensors and Bioelectronics, 72 (2015) 268-274.

81. L. De Stefano, P. Maddalena, L. Moretti, I. Rea, I. Rendina, E. De Tommasi, V. Mocella and M. De Stefano, Nano-biosilica from marine diatoms: A brand new material for photonic applications, Superlattices and Microstructures, 46 (2009) 84-89.

82. Diatoms, http://lifeofplant.blogspot.com/2011/04/diatoms.html, (accessed 8/24/2019, 2019).

83. J.D. Wehr and R.G. Sheath, in *Freshwater Algae of North America*, eds. J. D. Wehr and R. G. Sheath, Academic Press, Burlington, 2003, DOI: https://doi.org/10.1016/B978-012741550-5/50003-9, pp. 11-57.

84. S. Spaulding, How big are diatoms?, https://diatoms.org/news/how-big-are-diatoms, (accessed 8/23/19, 2019).

85. S. Maher, T. Kumeria, M.S. Aw and D. Losic, Diatom Silica for Biomedical Applications: Recent Progress and Advances, Advanced Healthcare Materials, 7 (2018) 1800552.

86. L.D. Stefano, I. Rea, I. Rendina, M.D. Stefano and L. Moretti, Lensless light focusing with the centric marine diatom Coscinodiscus walesii, Optics Express, 15 (2007) 18082-18088.

87. J. Noyes, M. Sumper and P. Vukusic, Light manipulation in a marine diatom, Journal of Materials Research, 23 (2008) 3229-3235.

88. K. Kieu, C. Li, Y. Fang, G. Cohoon, O.D. Herrera, M. Hildebrand, K.H. Sandhage and R.A. Norwood, Structure-based optical filtering by the silica microshell of the centric marine diatom Coscinodiscus wailesii, Optics Express, 22 (2014) 15992-15999.

89. T. Fuhrmann, S. Landwehr, M. El Rharbi-Kucki and M. Sumper, Diatoms as living photonic crystals, Applied Physics B, 78 (2004) 257-260.

90. S. Chandrasekaran, M.J. Sweetman, K. Kant, W. Skinner, D. Losic, T. Nann and N.H. Voelcker, Silicon diatom frustules as nanostructured photoelectrodes, Chemical Communications, 50 (2014) 10441-10444.

91. F. Ren, J. Campbell, X. Wang, G.L. Rorrer and A.X. Wang, Enhancing surface plasmon resonances of metallic nanoparticles by diatom biosilica, Optics Express, 21 (2013) 15308-15313.

92. K.S.A. Butcher, J.M. Ferris, M.R. Phillips, M. Wintrebert-Fouquet, J.W. Jong Wah, N. Jovanovic, W. Vyverman and V.A. Chepurnov, A luminescence study of porous diatoms, Materials Science and Engineering: C, 25 (2005) 658-663.

93. S. Lettieri, A. Setaro, L. De Stefano, M. De Stefano and P. Maddalena, The Gas-Detection Properties of Light-Emitting Diatoms, Advanced Functional Materials, 18 (2008) 1257-1264.

94. L.D. Stefano, I. Rendina, M.D. Stefano, A. Bismuto and P. Maddalena, Marine diatoms as optical chemical sensors, Applied Physics Letters, 87 (2005) 233902.

95. C. Jeffryes, R. Solanki, Y. Rangineni, W. Wang, C.-h. Chang and G.L. Rorrer, Electroluminescence and Photoluminescence from Nanostructured Diatom Frustules Containing Metabolically Inserted Germanium, Advanced Materials, 20 (2008) 2633-2637.

96. T. Qin, T. Gutu, J. Jiao, C.-h. Chang and G.L. Rorrer, Biological Fabrication of Photoluminescent Nanocomb Structures by Metabolic Incorporation of Germanium into the Biosilica of the Diatom Nitzschia frustulum, ACS Nano, 2 (2008) 1296-1304.

97. X. Kong, et al., Chemical and Biological Sensing Using Diatom Photonic Crystal Biosilica With In-Situ Growth Plasmonic Nanoparticles, IEEE Transactions on NanoBioscience, 15 (2016) 828-834.

98. X. Kong, Y. Xi, P. LeDuff, E. Li, Y. Liu, L.-J. Cheng, G.L. Rorrer, H. Tan and A.X. Wang, Optofluidic sensing from inkjet-printed droplets: the enormous enhancement by

evaporation-induced spontaneous flow on photonic crystal biosilica, Nanoscale, 8 (2016) 17285-17294.

99. J. Yang, L. Zhen, F. Ren, J. Campbell, G.L. Rorrer and A.X. Wang, Ultra-sensitive immunoassay biosensors using hybrid plasmonic-biosilica nanostructured materials, Journal of Biophotonics, 8 (2015) 659-667.

100. F. Ren, J. Campbell, G.L. Rorrer and A.X. Wang, Surface-Enhanced Raman Spectroscopy Sensors From Nanobiosilica With Self-Assembled Plasmonic Nanoparticles, IEEE Journal of Selected Topics in Quantum Electronics, 20 (2014) 127-132.

101. X. Kong, Y. Xi, P. Le Duff, X. Chong, E. Li, F. Ren, G.L. Rorrer and A.X. Wang, Detecting explosive molecules from nanoliter solution: A new paradigm of SERS sensing on hydrophilic photonic crystal biosilica, Biosensors and Bioelectronics, 88 (2017) 63-70.

102. S.C. Pinzaru, C. Müller, S. Tomšić, M.M. Venter, I. Brezestean, S. Ljubimir and B. Glamuzina, Live diatoms facing Ag nanoparticles: surface enhanced Raman scattering of bulk cylindrotheca closterium pennate diatoms and of the single cells, RSC Advances, 6 (2016) 42899-42910.

103. A. Kamińska, M. Sprynskyy, K. Winkler and T. Szymborski, Ultrasensitive SERS immunoassay based on diatom biosilica for detection of interleukins in blood plasma, Analytical and bioanalytical chemistry, 409 (2017) 6337-6347.

104. K.E. Marshall, E.W. Robinson, S.M. Hengel, L. Paša-Tolić and G. Roesijadi, FRET Imaging of Diatoms Expressing a Biosilica-Localized Ribose Sensor, PLOS ONE, 7 (2012) e33771.

105. J. Pan, J. Cai, D. Zhang, Y. Jiang, Y. Wang, M. Chen and A. Li, Diatom based biosensor for high sensitive fluorescence detection based on a spin-on glass bonding technique, IEEE Sensors, (2012) 1-5.

106. S. Weiss, Fluorescence Spectroscopy of Single Biomolecules, Science, 283 (1999) 1676-1683.

107. J.R. Lakowicz, *Topics in Fluorescence Spectroscopy*, Plenum Press, New, York, 1994.

108. J.C. Pickup, F. Hussain, N.D. Evans, O.J. Rolinski and D.J.S. Birch, Fluorescence-based glucose sensors, Biosensors and Bioelectronics, 20 (2005) 2555-2565.

109. F. Luo, L. Zheng, S. Chen, Q. Cai, Z. Lin, B. Qiu and G. Chen, An aptamer-based fluorescence biosensor for multiplex detection using unmodified gold nanoparticles, Chemical Communications, 48 (2012) 6387-6389.

110. E. Sikorska, A. Gliszczyńska-Świgło, I. Khmelinskii and M. Sikorski, Synchronous Fluorescence Spectroscopy of Edible Vegetable Oils. Quantification of Tocopherols, Journal of Agricultural and Food Chemistry, 53 (2005) 6988-6994.

111. L. Yi, H. Li, L. Sun, L. Liu, C. Zhang and Z. Xi, A Highly Sensitive Fluorescence Probe for Fast Thiol-Quantification Assay of Glutathione Reductase, Angewandte Chemie International Edition, 48 (2009) 4034-4037.

112. H. Jo, J. Her and C. Ban, Dual aptamer-functionalized silica nanoparticles for the highly sensitive detection of breast cancer, Biosensors and Bioelectronics, 71 (2015) 129-136.

113. J. Zhang, L. Wang, H. Zhang, F. Boey, S. Song and C. Fan, Aptamer-Based Multicolor Fluorescent Gold Nanoprobes for Multiplex Detection in Homogeneous Solution, Small, 6 (2010) 201-204.

114. A.V. Sheahan, T.V. Sekar, K. Chen, R. Paulmurugan and T.F. Massoud, A molecular imaging biosensor detects in vivo protein folding and misfolding, Journal of Molecular Medicine, 94 (2016) 799-808.

115. X. Lu, P.R. Nicovich, K. Gaus and J.J. Gooding, Towards single molecule biosensors using super-resolution fluorescence microscopy, Biosensors and Bioelectronics, 93 (2017) 1-8.

116. E.H.K. Stelzer, Light-sheet fluorescence microscopy for quantitative biology, Nature Methods, 12 (2014) 23.

117. H. Deschout, F.C. Zanacchi, M. Mlodzianoski, A. Diaspro, J. Bewersdorf, S.T. Hess and K. Braeckmans, Precisely and accurately localizing single emitters in fluorescence microscopy, Nature Methods, 11 (2014) 253.

118. A. Kuroda, M. Alexandrov, T. Nishimura and T. Ishida, Rapid on-site detection of airborne asbestos fibers and potentially hazardous nanomaterials using fluorescence microscopy-based biosensing, Biotechnology Journal, 11 (2016) 757-767.

119. X. Gao, C. Ding, A. Zhu and Y. Tian, Carbon-Dot-Based Ratiometric Fluorescent Probe for Imaging and Biosensing of Superoxide Anion in Live Cells, Analytical Chemistry, 86 (2014) 7071-7078.

120. A.F. Coskun, R. Nagi, K. Sadeghi, S. Phillips and A. Ozcan, Albumin testing in urine using a smart-phone, Lab on a Chip, 13 (2013) 4231-4238.

121. N. Ganesh, I.D. Block, P.C. Mathias, W. Zhang, E. Chow, V. Malyarchuk and B.T. Cunningham, Leaky-mode assisted fluorescence extraction: application to fluorescence enhancement biosensors, Optics Express, 16 (2008) 21626-21640.

122. M. Bauch, K. Toma, M. Toma, Q. Zhang and J. Dostalek, Plasmon-Enhanced Fluorescence Biosensors: a Review, Plasmonics, 9 (2014) 781-799.

123. D. Gallegos, K.D. Long, H. Yu, P.P. Clark, Y. Lin, S. George, P. Nath and B.T. Cunningham, Label-free biodetection using a smartphone, Lab on a Chip, 13 (2013) 2124-2132.

124. S. Dutta, K. Saikia and P. Nath, Smartphone based LSPR sensing platform for bio-conjugation detection and quantification, RSC Advances, 6 (2016) 21871-21880.

125. C.C. Cheng and A. Scherer, Fabrication of photonic band-gap crystals, Journal of Vacuum Science & Technology B: Microelectronics and Nanometer Structures Processing, Measurement, and Phenomena, 13 (1995) 2696-2700.

126. M. Campbell, D.N. Sharp, M.T. Harrison, R.G. Denning and A.J. Turberfield, Fabrication of photonic crystals for the visible spectrum by holographic lithography, Nature, 404 (2000) 53.

127. A. Pokhriyal, M. Lu, V. Chaudhery, C.-S. Huang, S. Schulz and B.T. Cunningham, Photonic crystal enhanced fluorescence using a quartz substrate to reduce limits of detection, Optics Express, 18 (2010) 24793-24808.

128. H. Li, et al., Near-Infrared Selective and Angle-Independent Backscattering from Magnetite Nanoparticle-Decorated Diatom Frustules, ACS Photonics, 1 (2014) 477-482.

129. X. Kong, Q. Yu, E. Li, R. Wang, Q. Liu and A.X. Wang, Diatomite photonic crystals for facile on-chip chromatography of harmful ingredients from food, Materials 11 (2018).

130. Y.-J. Hung, I.I. Smolyaninov, C.C. Davis and H.-C. Wu, Fluorescence enhancement by surface gratings, Optics Express, 14 (2006) 10825-10830.

131. S.V. Gaponenko, et al., Spontaneous emission of dye molecules, semiconductor nanocrystals, and rare-earth ions in opal-based photonic crystals, Journal of Lightwave Technology, 17 (1999) 2128-2137.

132. A.R. Guerrero and R.F. Aroca, Surface-Enhanced Fluorescence with Shell-Isolated Nanoparticles (SHINEF), Angewandte Chemie International Edition, 50 (2011) 665-668.

133. H. Yu, Y. Tan and B.T. Cunningham, Smartphone Fluorescence Spectroscopy, Analytical Chemistry, 86 (2014) 8805-8813.

134. W. Chen, et al., Mobile Platform for Multiplexed Detection and Differentiation of Disease-Specific Nucleic Acid Sequences, Using Microfluidic Loop-Mediated Isothermal Amplification and Smartphone Detection, Analytical Chemistry, 89 (2017) 11219-11226.

135. D. Mozaffarian, et al., Heart Disease and Stroke Statistics-2016 Update, Circulation, 133 (2016) e38-e360.

136. P.A. Heidenreich, et al., Forecasting the Future of Cardiovascular Disease in the United States, Circulation, 123 (2011) 933-944.

137. P. Ponikowski, et al., 2016 ESC Guidelines for the diagnosis and treatment of acute and chronic heart failureThe Task Force for the diagnosis and treatment of acute and chronic heart failure of the European Society of Cardiology (ESC)Developed with the special contribution of the Heart Failure Association (HFA) of the ESC, European Heart Journal, 37 (2016) 2129-2200.

138. J.L. Januzzi, et al., The N-terminal Pro-BNP Investigation of Dyspnea in the Emergency department (PRIDE) study, The American Journal of Cardiology, 95 (2005) 948-954.

139. M.C. Laboratories, NT-Pro B-Type Natriuretic Peptide (BNP), Serum, https://www.mayocliniclabs.com/test-catalog/Performance/84291, (accessed 20 December 2017, 2017).

140. E. Song, M. Yu, Y. Wang, W. Hu, D. Cheng, M.T. Swihart and Y. Song, Multi-color quantum dot-based fluorescence immunoassay array for simultaneous visual detection of multiple antibiotic residues in milk, Biosensors and Bioelectronics, 72 (2015) 320-325.

141. H.-F. Wang and S.-P. Wu, A pyrene-based highly selective turn-on fluorescent sensor for copper(II) ions and its application in living cell imaging, Sensors and Actuators B: Chemical, 181 (2013) 743-748.

142. D. Zhang, M. Li, M. Wang, J. Wang, X. Yang, Y. Ye and Y. Zhao, A rhodamine-phosphonate off–on fluorescent sensor for Hg2+ in natural water and its application in live cell imaging, Sensors and Actuators B: Chemical, 177 (2013) 997-1002.

143. B. Zhang, et al., Fluorescence quenching-based signal amplification on immunochromatography test strips for dual-mode sensing of two biomarkers of breast cancer, Nanoscale, 9 (2017) 18711-18722.

144. Y. Chen, Y. Wu, B. Weng, B. Wang and C. Li, Facile synthesis of nitrogen and sulfur co-doped carbon dots and application for Fe(III) ions detection and cell imaging, Sensors and Actuators B: Chemical, 223 (2016) 689-696.

145. P. Hartmann, W. Ziegler, G. Holst and D.W. Lübbers, Oxygen flux fluorescence lifetime imaging, Sensors and Actuators B: Chemical, 38 (1997) 110-115.

146. A. Agrawal, C. Zhang, T. Byassee, R.A. Tripp and S. Nie, Counting Single Native Biomolecules and Intact Viruses with Color-Coded Nanoparticles, Analytical Chemistry, 78 (2006) 1061-1070.

147. L. Cai, N. Friedman and X.S. Xie, Stochastic protein expression in individual cells at the single molecule level, Nature, 440 (2006) 358.

148. J.H. Lee, H.K. Choi and J.H. Chang, Optimization of biotin labeling of antibodies using mouse IgG and goat anti-mouse IgG-conjugated fluorescent beads and their application as capture probes on protein chip, Journal of Immunological Methods, 362 (2010) 38-42.

149. M.D. Wilkins, B.L. Turner, K.R. Rivera, S. Menegatti and M. Daniele, Quantum dot enabled lateral flow immunoassay for detection of cardiac biomarker NT-proBNP, Sensing and Bio-Sensing Research, 21 (2018) 46-53.

150. M.B. Mohamed, V. Volkov, S. Link and M.A. El-Sayed, The `lightning' gold nanorods: fluorescence enhancement of over a million compared to the gold metal, Chemical Physics Letters, 317 (2000) 517-523.

151. N. Sui, L. Wang, T. Yan, F. Liu, J. Sui, Y. Jiang, J. Wan, M. Liu and W.W. Yu, Selective and sensitive biosensors based on metal-enhanced fluorescence, Sensors and Actuators B: Chemical, 202 (2014) 1148-1153.

152. H. Tan and Y. Chen, Silver nanoparticle enhanced fluorescence of europium (III) for detection of tetracycline in milk, Sensors and Actuators B: Chemical, 173 (2012) 262-267.

153. S. Chakravarty, Y. Zou, W.-C. Lai and R.T. Chen, Slow light engineering for high Q high sensitivity photonic crystal microcavity biosensors in silicon, Biosensors & bioelectronics, 38 (2012) 170-176.

154. J. Hou, H. Zhang, Q. Yang, M. Li, Y. Song and L. Jiang, Bio-Inspired Photonic-Crystal Microchip for Fluorescent Ultratrace Detection, Angewandte Chemie International Edition, 53 (2014) 5791-5795.

155. P.-E. Buffet, et al., Biochemical and behavioural responses of the marine polychaete Hediste diversicolor to cadmium sulfide quantum dots (CdS QDs): Waterborne and dietary exposure, Chemosphere, 100 (2014) 63-70.

156. D.R. Larson, W.R. Zipfel, R.M. Williams, S.W. Clark, M.P. Bruchez, F.W. Wise and W.W. Webb, Water-Soluble Quantum Dots for Multiphoton Fluorescence Imaging in Vivo, Science, 300 (2003) 1434.

157. S.R. Cordero, P.J. Carson, R.A. Estabrook, G.F. Strouse and S.K. Buratto, Photo-Activated Luminescence of CdSe Quantum Dot Monolayers, The Journal of Physical Chemistry B, 104 (2000) 12137-12142.

158. W.G.J.H.M. van Sark, P.L.T.M. Frederix, A.A. Bol, H.C. Gerritsen and A. Meijerink, Blueing, Bleaching, and Blinking of Single CdSe/ZnS Quantum Dots, ChemPhysChem, 3 (2002) 871-879.

159. R. Diez, M.C. Ortiz, L. Sarabia and I. Birlouez-Aragon, Potential of front face fluorescence associated to PLS regression to predict nutritional parameters in heat treated infant formula models, Analytica Chimica Acta, 606 (2008) 151-158.

160. O. Divya and A.K. Mishra, Combining synchronous fluorescence spectroscopy with multivariate methods for the analysis of petrol-kerosene mixtures, Talanta, 72 (2007) 43-48.

161. X. Yan, H. Li, X. Han and X. Su, A ratiometric fluorescent quantum dots based biosensor for organophosphorus pesticides detection by inner-filter effect, Biosensors and Bioelectronics, 74 (2015) 277-283.

162. C. Kurachi, C.R. Fontana, L.E.B. Rosa and V.S. Bagnato, Fluorescence spectroscopy for the detection of tongue carcinoma—validation in an animal model, Journal of Biomedical Optics, 13 (2008) 6.

163. D. Moshou, X.-E. Pantazi, D. Kateris and I. Gravalos, Water stress detection based on optical multisensor fusion with a least squares support vector machine classifier, Biosystems Engineering, 117 (2014) 15-22.

164. Y. Zhang, X. Zhou, R.M. Witt, B.L. Sabatini, D. Adjeroh and S.T.C. Wong, Dendritic spine detection using curvilinear structure detector and LDA classifier, NeuroImage, 36 (2007) 346-360.

165. C. Jeffryes, T. Gutu, J. Jiao and G.L. Rorrer, Two-stage photobioreactor process for the metabolic insertion of nanostructured germanium into the silica microstructure of the diatom Pinnularia sp, Materials Science and Engineering: C, 28 (2008) 107-118.

166. J.A. Berges, D.J. Franklin and P.J. Harrison, Evolution of an artificial seawater medium: improvements in enriched seawater, artificial water over the last two decades, Journal of Phycology, 37 (2001) 1138-1145.

167. K. Squire, X. Kong, P. LeDuff, G.L. Rorrer and A.X. Wang, Photonic crystal enhanced fluorescence immunoassay on diatom biosilica, Journal of Biophotonics, 11 (2018) e201800009.

168. C.-C. Chang and C.-J. Lin, LIBSVM: A library for support vector machines, ACM Trans. Intell. Syst. Technol., 2 (2011) 1-27.

169. K. Kneipp, Y. Wang, H. Kneipp, L.T. Perelman, I. Itzkan, R.R. Dasari and M.S. Feld, Single Molecule Detection Using Surface-Enhanced Raman Scattering (SERS), Physical Review Letters, 78 (1997) 1667-1670.

170. R. Kodiyath, S.T. Malak, Z.A. Combs, T. Koenig, M.A. Mahmoud, M.A. El-Sayed and V.V. Tsukruk, Assemblies of silver nanocubes for highly sensitive SERS chemical vapor detection, Journal of Materials Chemistry A, 1 (2013) 2777-2788.

171. L.E. Kreno, N.G. Greeneltch, O.K. Farha, J.T. Hupp and R.P. Van Duyne, SERS of molecules that do not adsorb on Ag surfaces: a metal–organic framework-based functionalization strategy, Analyst, 139 (2014) 4073-4080.

172. N. Taranenko, J.-P. Alarie, D.L. Stokes and T. Vo-Dinh, Surface-Enhanced Raman Detection of Nerve Agent Simulant (DMMP and DIMP) Vapor on Electrochemically Prepared Silver Oxide Substrates, Journal of Raman Spectroscopy, 27 (1996) 379-384.

173. G.C. Phan-Quang, et al., Tracking Airborne Molecules from Afar: Three-Dimensional Metal-Organic-Framework - Surface-Enhanced Raman Scattering (MOF-SERS) Platform for Stand-Off and Real-Time Atmospheric Monitoring, ACS Nano, DOI: 10.1021/acsnano.9b06486 (2019).

174. C. Muehlethaler, M. Leona and J.R. Lombardi, Review of Surface Enhanced Raman Scattering Applications in Forensic Science, Analytical Chemistry, 88 (2016) 152-169.

175. A. Chou, E. Jaatinen, R. Buividas, G. Seniutinas, S. Juodkazis, E.L. Izake and P.M. Fredericks, SERS substrate for detection of explosives, Nanoscale, 4 (2012) 7419-7424.

176. M.K. Khaing Oo, C.-F. Chang, Y. Sun and X. Fan, Rapid, sensitive DNT vapor detection with UV-assisted photo-chemically synthesized gold nanoparticle SERS substrates, Analyst, 136 (2011) 2811-2817.

177. M.K. Khaing Oo, Y. Guo, K. Reddy, J. Liu and X. Fan, Ultrasensitive Vapor Detection with Surface-Enhanced Raman Scattering-Active Gold Nanoparticle Immobilized Flow-Through Multihole Capillaries, Analytical Chemistry, 84 (2012) 3376-3381.

178. B.D. Piorek, S.J. Lee, M. Moskovits and C.D. Meinhart, Free-Surface Microfluidics/Surface-Enhanced Raman Spectroscopy for Real-Time Trace Vapor Detection of Explosives, Analytical Chemistry, 84 (2012) 9700-9705.

179. T. Demeritte, R. Kanchanapally, Z. Fan, A.K. Singh, D. Senapati, M. Dubey, E. Zakar and P.C. Ray, Highly efficient SERS substrate for direct detection of explosive TNT using popcorn-shaped gold nanoparticle-functionalized SWCNT hybrid, Analyst, 137 (2012) 5041-5045.

180. J. Wang, L. Yang, S. Boriskina, B. Yan and B.M. Reinhard, Spectroscopic Ultra-Trace Detection of Nitroaromatic Gas Vapor on Rationally Designed Two-Dimensional Nanoparticle Cluster Arrays, Analytical Chemistry, 83 (2011) 2243-2249.

181. J.M. Sylvia, J.A. Janni, J.D. Klein and K.M. Spencer, Surface-Enhanced Raman Detection of 2,4-Dinitrotoluene Impurity Vapor as a Marker To Locate Landmines, Analytical Chemistry, 72 (2000) 5834-5840.

182. H. Ko, S. Chang and V.V. Tsukruk, Porous Substrates for Label-Free Molecular Level Detection of Nonresonant Organic Molecules, ACS Nano, 3 (2009) 181-188.

183. S.-Y. Cho, S.J. Kim, Y. Lee, J.-S. Kim, W.-B. Jung, H.-W. Yoo, J. Kim and H.-T. Jung, Highly Enhanced Gas Adsorption Properties in Vertically Aligned MoS2 Layers, ACS Nano, 9 (2015) 9314-9321.

184. J.M. Chan, L. Zhang, K.P. Yuet, G. Liao, J.-W. Rhee, R. Langer and O.C. Farokhzad, PLGA–lecithin–PEG core–shell nanoparticles for controlled drug delivery, Biomaterials, 30 (2009) 1627-1634.

185. K. Sivashanmugan, K. Squire, J.A. Kraai, A. Tan, Y. Zhao, G.L. Rorrer and A.X. Wang, Biological Photonic Crystal-Enhanced Plasmonic Mesocapsules: Approaching Single-Molecule Optofluidic-SERS Sensing, Advanced Optical Materials, 7 (2019) 1900415.

186. K.J. Squire, Y. Zhao, A. Tan, K. Sivashanmugan, J.A. Kraai, G.L. Rorrer and A.X. Wang, Photonic crystal-enhanced fluorescence imaging immunoassay for cardiovascular disease biomarker screening with machine learning analysis, Sensors and Actuators B: Chemical, 290 (2019) 118-124.

187. N. Chamuah, L. Chetia, N. Zahan, S. Dutta, G.A. Ahmed and P. Nath, A naturally occurring diatom frustule as a SERS substrate for the detection and quantification of chemicals, Journal of Physics D: Applied Physics, 50 (2017) 175103.

188. S.C. Davis, V.C. Sheppard, G. Begum, Y. Cai, Y. Fang, J.D. Berrigan, N. Kröger and K.H. Sandhage, Rapid Flow-Through Biocatalysis with High Surface Area, Enzyme-Loaded Carbon and Gold-Bearing Diatom Frustule Replicas, Advanced Functional Materials, 23 (2013) 4611-4620.

189. M. Tortajada, D. Ramón, D. Beltrán and P. Amorós, Hierarchical bimodal porous silicas and organosilicas for enzyme immobilization, Journal of Materials Chemistry, 15 (2005) 3859-3868.

190. T.T.B. Quyen, W.-N. Su, K.-J. Chen, C.-J. Pan, J. Rick, C.-C. Chang and B.-J. Hwang, Au@SiO2 core/shell nanoparticle assemblage used for highly sensitive SERS-based determination of glucose and uric acid, Journal of Raman Spectroscopy, 44 (2013) 1671-1677.

191. Y. Liu and Z. Tang, Multifunctional Nanoparticle@MOF Core–Shell Nanostructures, Advanced Materials, 25 (2013) 5819-5825.

192. M. Mueller, M. Tebbe, D.V. Andreeva, M. Karg, R.A. Alvarez Puebla, N. Pazos Perez and A. Fery, Large-Area Organization of pNIPAM-Coated Nanostars as SERS Platforms for Polycyclic Aromatic Hydrocarbons Sensing in Gas Phase, Langmuir, 28 (2012) 9168-9173.

193. L. Ma, H. Wu, Y. Huang, S. Zou, J. Li and Z. Zhang, High-Performance Real-Time SERS Detection with Recyclable Ag Nanorods@HfO2 Substrates, ACS Applied Materials & Interfaces, 8 (2016) 27162-27168.

194. Y. Lu, J. McLellan and Y. Xia, Synthesis and Crystallization of Hybrid Spherical Colloids Composed of Polystyrene Cores and Silica Shells, Langmuir, 20 (2004) 3464-3470.

195. M.P. Nikolić, K.P. Giannakopoulos and V.V. Srdić, Synthesis and characterization of mesoporous and superparamagnetic bilayered-shell around silica core particles, Ceramics International, 41 (2015) 13480-13485.

196. C. Song, J. Chen, J.L. Abell, Y. Cui and Y. Zhao, Ag–SiO2 Core–Shell Nanorod Arrays: Morphological, Optical, SERS, and Wetting Properties, Langmuir, 28 (2012) 1488-1495.

197. A. Walcarius, C. Despas and J. Bessière, Molecular sieving with amorphous monodisperse silica beads, Microporous and Mesoporous Materials, 23 (1998) 309-313.

198. C. Wang, Y. Chen, T. Wang, Z. Ma and Z. Su, Monodispersed Gold Nanorod-Embedded Silica Particles as Novel Raman Labels for Biosensing, Advanced Functional Materials, 18 (2008) 355-361.

199. Landmine Monitor 2018, http://www.the-monitor.org/en-gb/reports/2018/landmine-monitor-2018/preface.aspx, (accessed 9/5/2019, 2019).

200. A. Rose, Z. Zhu, C.F. Madigan, T.M. Swager and V. Bulović, Sensitivity gains in chemosensing by lasing action in organic polymers, Nature, 434 (2005) 876-879.

201. V. George, T.F. Jenkins, D.C. Leggett, J.H. Cragin, J.M. Phelan, J.C. Oxley and J. Pennington, *Progress on determining the vapor signature of a buried land mine*, SPIE, 1999.

202. O. Tsendra, A.M. Scott, L. Gorb, A.D. Boese, F.C. Hill, M.M. Ilchenko, D. Leszczynska and J. Leszczynski, Adsorption of Nitrogen-Containing Compounds on the (100) α-Quartz Surface: Ab Initio Cluster Approach, The Journal of Physical Chemistry C, 118 (2014) 3023-3034.